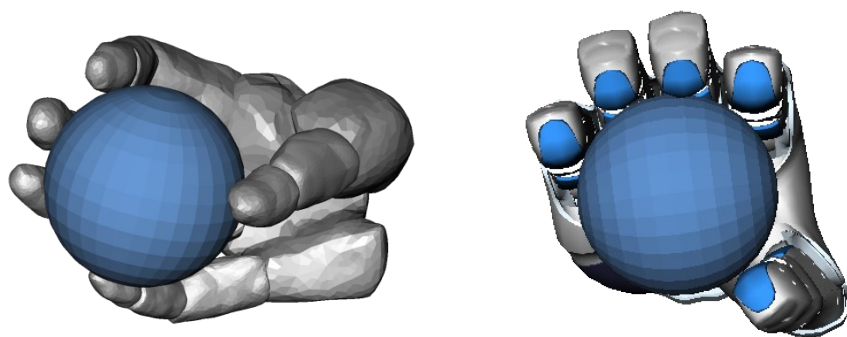


Georg Stillfried

Kinematic modelling of the human hand for robotics



PhD Thesis

TECHNISCHE UNIVERSITÄT MÜNCHEN
Fakultät für Informatik
Lehrstuhl für Echtzeitsysteme und Robotik
Biomimetic Robotics and Machine Learning

**Kinematic modelling of the human hand for
robotics**

Dipl.-Ing. Univ. Georg Norbert Christoph Dominik Graf von
Stillfried-Rattonitz

Vollständiger Abdruck der von der Fakultät für Informatik der Technischen Universität München zur Erlangung des akademischen Grades eines

Doktors der Naturwissenschaften (Dr. rer. nat.)

genehmigten Dissertation.

Vorsitzender: Univ.-Prof. Dr.-Ing. Alin Albu-Schäffer

Prüfer der Dissertation: 1. Univ-Prof. Dr. Patrick van der Smagt
2. Univ-Prof. Dr.-Ing. Tamim Asfour,
Karlsruher Institut für Technologie

Die Dissertation wurde am 30.03.2015 bei der Technischen Universität München eingereicht und durch die Fakultät für Informatik am 27.07.2015 angenommen.

Abstract

Human hand movement models are needed for the design of humanoid robotic hands. Humanoid hands are robotic hands that resemble human hands, especially regarding their appearance and their ability to move. Possible application areas of humanoid hands are expected in human-inhabited environments, in teleoperation and in prosthetics.

The goal for this thesis is to find out which kinematic properties of the human hand are important and should be implemented in a humanoid hand. For this, a model is desired that matches the mobility of the human hand as closely as possible. It should be able to replicate the movements that the human hand is able to do and avoid movements that the human hand is unable to do. Such a kinematic model of the human hand that can be used for simulations has been lacking.

This thesis aims to find answers to the following questions:

1. How can human hand movements be measured?
2. How can the kinematic structure be modelled?
3. How does the kinematic structure of the hand affect its functionality?

As answers to the first and second questions, for the first time, a complete human hand movement model is created on the basis of magnetic resonance imaging (MRI).

The whole tool chain from recording to the complete simulation is presented. It contains the following steps: recording of hand postures in MRI, segmentation of bones from the MRI images, determination of the bone poses, definition of a set of joint types, identification of joint parameters and calculation of the discrepancy between the measurement and the model, choice of a suitable joint type from the set of joint types and the creation of surface geometries.

The discrepancy between measurement and model can be adjusted within certain limits by choosing suitable joint types. For example, a desired limit of 6° and 3 mm on the mean discrepancy of each joint leads to a selection of joint

types that result in a hand model with 24 degrees of freedom. This amount of discrepancy is considered tolerable for grasping medium-sized objects. Depending on the desired application, other points on the trade-off curve between complexity and accuracy need to be selected.

As an answer to the third question, above hand model is extended with surface geometries and applied in a simulation of grasps. It is compared with two additional hand models that contain alternative thumb joint types, since these are particularly controversial. However, the six grasps that are investigated do not show any clear difference between the thumb models. Additionally, the human hand models are compared to a robotic hand model (DLR/HIT Hand II). The robotic hand is able to reach five of the prescribed grasps, but not the grasp of a pen or similar cylindrical object between the phalanges of the fingers. It is able to fulfill the task only with an alternative grasp type.

It is hypothesised that hand movement models based on MRI are more accurate than those based on position measurements of markers attached to the skin, because the skin moves with respect to the bone and thereby violates the premise of a rigid body mechanism, which is commonly used in kinematic modelling. In this thesis, this hypothesis is tested by comparing MRI measurements and skin marker measurements of a hand. The results do not show any substantial accuracy difference between both methods, expanding the answer to the first question by the fact that skin marker measurements can be used as well.

Hence, the skin movement does not seem to influence the measurement accuracy more than other sources of error that occur in MRI measurements. Still, it may be possible to further improve the measurement accuracy of the skin markers by modelling and compensating the skin movement. In this thesis, the movement of the skin with respect to the bone is measured using MRI. Furthermore, a model for skin movement near joints is validated. It is shown that using this model, the measurement accuracy can be substantially improved (by about 50%). This expands the answer to the second question on how to model the kinematic structure, by including elastic skin kinematics in addition to rigid bone kinematics.

This thesis provides the following core results:

1. The number of degrees of freedom of a data-driven hand model depends on how closely the measured movements shall be replicated. This trade-off between complexity and error is shown using three examples of hand models based on MRI data.
2. Skin marker measurements provide similar accuracy as MRI for measuring

hand postures.

3. Skin movement is larger near joints but a large part of it can be explained by a rotational model.
4. In a simulation of six defined grasps with three human hand models and one robotic hand model, it is shown that a higher number of degrees of freedom tends to increase grasp stability.
5. An influence of the kinematic structure on the ability to form force closure grasps can not be shown with these combinations of grippers and object grasps.
6. However, an influence of the link surface geometry on grasp functionality can be shown: the so-called light tool grasp works better with thin fingers than thick fingers.
7. Simpler grasps also tend to increase grasp stability.

In summary, the methods developed in this thesis allow the creation of kinematic hand models for investigating the most important kinematic properties for humanoid robotic hands.

Zusammenfassung

Modelle der menschlichen Handbeweglichkeit werden für die Konstruktion von humanoiden Händen benötigt. Humanoide Hände sind Roboterhände, welche menschlichen Händen ähneln, besonders hinsichtlich ihres Aussehens und ihrer Bewegungsmöglichkeiten. Anwendungsmöglichkeiten von humanoiden Roboterhänden werden in von Menschen bewohnter Umgebung, in der Telemanipulation und in der Prothetik erwartet.

Das Ziel dieser Dissertation ist herauszufinden, welche kinematischen Eigenheiten der menschlichen Hand wichtig sind und in humanoiden Robotern umgesetzt werden sollten. Dafür ist ein Modell wünschenswert, welches die Beweglichkeit der Hand so eng wie möglich abdeckt. Es sollte alle möglichen Bewegungen der menschlichen Hand möglichst genau nachbilden und unmögliche Bewegungen der menschlichen Hand vermeiden. Ein solches kinematisches Modell der menschlichen Hand, welches für Simulationen verwendet werden kann, fehlte bisher.

Diese Dissertation zielt darauf ab, Antworten für die folgenden Fragen zu finden:

1. Wie können menschliche Handbewegungen gemessen werden?
2. Wie kann die kinematische Struktur modelliert werden?
3. Wie beeinflusst die kinematische Struktur der Hand ihre Funktionalität?

Als Antwort auf die erste Frage wird erstmals mit Hilfe von Magnetresonanztomographie (MRT)-Aufnahmen ein vollständiges Bewegungsmodell der menschlichen Hand erstellt.

Der gesamte Ablauf von der Aufnahme bis hin zur fertigen Simulation wird präsentiert. Folgende Schritte sind darin enthalten: Aufnehmen von Handstellungen im MRT, Segmentieren der Knochen aus den MRT-Aufnahmen, Bestimmung der Knochenlagen, Erstellung einer Liste von Gelenktypen, Identifizierung der Gelenkparameter und Bestimmung der Abweichung zwischen Messung und Modell, Auswahl eines geeigneten Gelenktyps aus der Liste der Gelenktypen und Erstellung von Oberflächengeometrien.

Die Abweichung zwischen Messung und Modell kann in gewissen Grenzen eingestellt werden, indem geeignete Gelenktypen ausgewählt werden. Beispielsweise führt eine gewünschte mittlere Abweichung pro Gelenk von weniger als 6° und 3 mm zu einer Auswahl von Gelenktypen, die ein Handmodell mit 24 Freiheitsgraden ergeben. Dies wird als Abweichung angesehen, die beim Greifen von mittelgroßen Objekten toleriert werden kann. Je nachdem, wie fein manipuliert werden soll, kann die Genauigkeit des Modells eingestellt werden.

Als Antwort auf die dritte Frage wird das erwähnte Handmodell in einer Greifsimulation eingesetzt. Dieses wird mit zwei weiteren Handmodellen mit alternativen Daumengelenken verglichen, weil die Ausformung der Daumengelenke besonders umstritten ist. Allerdings zeigen sich bei den sechs untersuchten Griffen keine klaren Unterschiede zwischen den Daumenmodellen. Des Weiteren werden die menschlichen Handmodelle mit einem Roboterhandmodell (DLR/HIT Hand II) verglichen. Fünf vorgegebene Griffe werden auch von der Roboterhand erreicht, nicht aber das Greifen eines Stifts oder ähnlichen zylindrischen Objekts zwischen den Fingergliedern. Diese Aufgabe kann die Roboterhand nur mit einem alternativen Grifftyp erfüllen.

Es wird vermutet, dass Handbewegungsmodelle, die auf MRT basieren, genauer sind als solche, die auf Messung von Markerpositionen basieren, welche auf der Haut aufgebracht sind, weil sich die Haut gegenüber den Knochen bewegt und damit die übliche Annahme eines Starrkörpermechanismus verletzt. In dieser Arbeit wird diese Vermutung durch einen Vergleich von MRT und Hautmarker-Messung einer Hand überprüft. Im Ergebnis ist zwischen beiden Messmethoden kein nennenswerter Genauigkeitsunterschied zu erkennen, womit die Antwort auf die erste Frage dahingehend erweitert wird, dass Messungen von Hautmarkerpositionen ebenfalls verwendet werden können.

Die Hautbewegung scheint also die Messgenauigkeit nicht stärker zu beeinflussen als andere Fehlerquellen, die bei MRT-Messungen auftreten. Dennoch kann die Messgenauigkeit möglicherweise noch weiter erhöht werden, indem die Hautbewegung modelliert und kompensiert wird. Ein Modell zur Hautbewegungskompensation wird in dieser Arbeit validiert wobei sich zeigt, dass dadurch die Messgenauigkeit deutlich (um ca. 50%) erhöht werden kann.

Diese Dissertation stellt folgende Kernergebnisse zur Verfügung:

1. Die Anzahl von Freiheitsgraden eines datenbasierten Handmodells hängt davon ab, wie genau die gemessenen Bewegungen nachgebildet werden sollen. Dieser Zielkonflikt zwischen niedriger Komplexität und niedriger Abweichung wird anhand dreier Beispiele von Handmodellen gezeigt, welche auf MRT-Daten basieren.

2. Hautmarkermessungen bieten ähnliche Genauigkeit wie MRT für die Messung von Handstellungen.
3. Hautbewegungen sind in der Nähe von Gelenken größer, können aber zu einem großen Teil durch ein rotatorisches Modell erklärt werden.
4. In einer Simulation von sechs bestimmten Griffen mit drei menschlichen Handmodellen und einer Roboterhand wird gezeigt, dass eine höhere Anzahl von Freiheitsgraden tendenziell zu höherer Greifstabilität führt.
5. Ein Einfluss der kinematischen Struktur auf die Fähigkeit zur Erzeugung von kraftschlüssigen Griffen kann bei diesen Kombinationen von Greifern und Objektgriffen nicht gezeigt werden.
6. Jedoch kann ein Einfluss der Oberflächengeometrie der Fingerglieder auf die Greiffähigkeit gezeigt werden: Der Griff eines dünnen Zylinders zwischen den Fingergliedern funktioniert mit dünnen Fingern besser als mit dicken.
7. Auch einfachere Griffe erhöhen tendenziell die Greifstabilität.

Zusammengefasst unterstützen die erarbeiteten Methoden bei der Erstellung eines kinematischen Handmodells zur Erforschung von wichtigen kinematischen Eigenschaften für humanoide Roboterhände. Zusammengefasst ermöglichen die erarbeiteten Methoden die Erstellung kinematischer Handmodelle zur Erforschung von wichtigen kinematischen Eigenschaften für humanoide Roboterhände.

Acknowledgment

This PhD thesis was written during my employment at the Institute of Robotics and Mechatronics at the German Aerospace Center (DLR) in Oberpfaffenhofen, Germany. The work was in part funded by the European Commission through the projects SENSOPAC (FP6-IST-028056) and The Hand Embodied (FP7-ICT-248587).

I gratefully acknowledge many contributions from my colleagues in the Bionics Group, in the Institute of Robotics and Mechatronics of DLR, in the BRML group at Technische Universität München (TUM), at the Rechts der Isar hospital of TUM and at the Centro Piaggio of University of Pisa. Without their technical and personal advice and scientific exchange this thesis would not have become what it is. I would like to specifically mention some of them:

My supervisor Patrick van der Smagt provided the idea of doing a PhD thesis on modelling of hand kinematics using MRI, established the contact to the hospital for the MRI images, encouraged me to plan the work and took the time to regularly discuss it with me. Tamim Asfour of Karlsruhe Institute of Technology kindly agreed to be the second reviewer of this thesis. The head of the Department of Autonomy and Teleoperation Christoph Borst gave me the freedom and opportunity to work on this thesis during the office hours. Marcus Settles of the TUM Rechts der Isar hospital worked the MRI machine and tried many different settings in order to obtain high-quality images and provided the text about it in our joint book chapter. Karolina Stonawska of TUM segmented the MRI images. Ulrich Hillenbrand provided the algorithm for the bone pose estimation and wrote about it in our book chapter. Hannes Höppner provided valuable discussion and advice on how to progress with this thesis, and proof-read the thesis. It was also his idea to let the skeletal hand model show the chapter numbers in Chinese manner. Theodoros Stouraitis programmed the graphical user interface for the grasp simulations and proof-read the Chapter on grasp simulations. Katharina Hertkorn processed the skin surface meshes for the grasp simulations. Simon Kriegel shared experiences and advice on submitting this thesis and proof-read it. Tim Bodenmüller shared his L^AT_EX

template. Marco Gabiccini, Hamal Marino and Matteo Bianchi discussed with me their ideas for the skin movement modelling.

Many thanks to the subjects who took part in the experiments.

I would also like to thank the members of the system administration, financial administration and secretarial administration, as well as the Department and Institute heads for providing the infrastructure that made this work possible.

Also in times of receding motivation, I received much encouragement from colleagues, the prayer group, friends and family.

Finally, special thanks to my partner Achim for his love and continuous support.

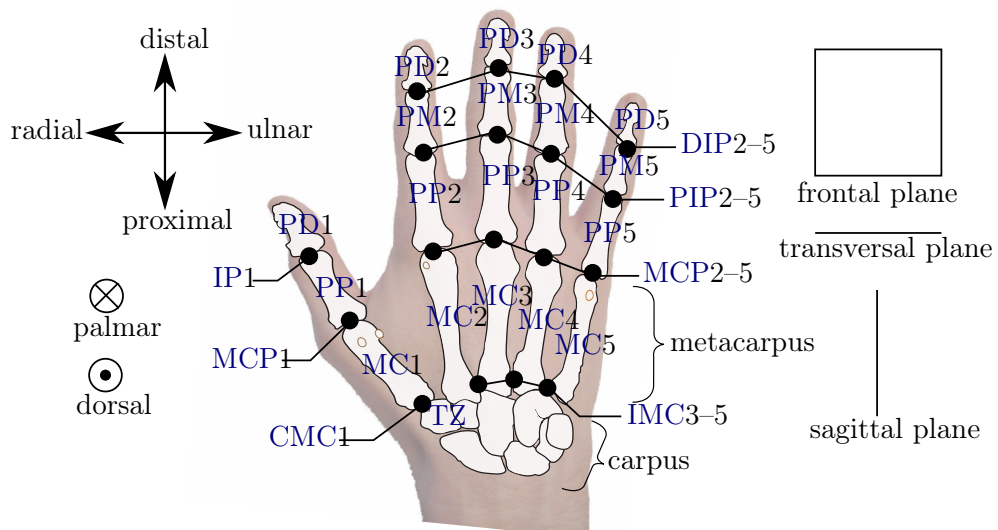
Contents

Anatomical terms	xv
Glossary	xv
Abbreviations	xvi
Mathematical notation	xvii
1 Introduction	1
2 Related work	5
2.1 Robotic hands	5
2.2 Modelling of human hand and finger joints	9
2.3 Measurement of human hand and finger postures	14
2.4 Measurement, modelling and compensation of skin movement . .	15
2.5 The role of the kinematic structure for the practical abilities . .	19
3 Determination of joint types	23
3.1 Methods	23
3.2 Results	44
3.3 Discussion	50
4 Hand models for grasp simulation	57
4.1 Methods	57
4.2 Results	60
4.3 Discussion	63
5 Comparison of magnetic resonance imaging (MRI) and optical motion capture (MoCap) for hand modelling	67
5.1 Methods	68
5.2 Results	72
5.3 Discussion	75
6 Validation of the skin movement model by Zhang et al.	77
6.1 Methods	77

6.2	Results	81
6.3	Discussion	82
7	Conclusion	85
7.1	Limitations	86
7.2	Outlook	88
	Bibliography	89

Anatomical Terms, Glossary, Abbreviations and Mathematical Notation

Anatomical terms



The abbreviated bone and joint names are explained in the Section [Abbreviations](#) below.

Glossary

DH parameters A minimal description of a serial chain of rotation or translation axes as described by Denavit and Hartenberg [1955] or a modification thereof [Khalil and Dombre, 2002, Craig, 2005, Waldron and Schmiedeler, 2008].

ex vivo On the dead body, that is, experiments on cadaveric specimens.

generativeness The ability of a humanoid robot to avoid generating unnatural poses.

in vivo On the living body, that is, experiments with live subjects.

kinematics The study of movement without regarding the forces that might cause it. In this thesis especially the movement *abilities* of a mechanism.

pose The position and orientation of a rigid object. The three-dimensional pose can be fully described by six independent parameters.

posture The set of poses of multiple rigid bodies that constitute an articulated object. “Hand posture” refers to the set of poses of the bones that constitute the hand, where the bones are idealised as rigid objects.

Abbreviations

1a	a joint with one rotation axis (see Figure 3.6)
2cia	a joint with two coupled rotation axes (see Figure 3.6)
2ia	a joint with two intersecting, possibly non-orthogonal, axes (see Figure 3.6)
2oia	a joint with two orthogonal intersecting axes (see Figure 3.6)
2ona	a joint with two orthogonal, possibly non-intersecting, axes (see Figure 3.6)
2na	a joint with two general axes that are possibly non-orthogonal and non-intersecting (see Figure 3.6)
3oia	a joint with three orthogonal and intersecting axes (see Figure 3.6)
3ona	a joint with three orthogonal, possibly non-intersecting, axes (see Figure 3.6)
2D	two dimensions, two-dimensional
3D	three dimensions, three-dimensional
ANOVA	analysis of variance 60
BCS	bone coordinate system 78
CoR	centre of rotation 10
CMC	carpometacarpal (joint, see Section Anatomical terms above) 52
CT	computed tomography 14
DLR	Deutsches Zentrum für Luft- und Raumfahrt e.V. (German Aerospace Center)

DIP	distal interphalangeal (joint, see Section Anatomical terms above)
DoF	degrees of freedom 6
EC	European Commission 21
EVA	extra-vehicular activity (in space) 60
GUI	graphical user interface..... 58
IP	inter-phalangeal (joint of the thumb, see Section Anatomical terms above)
IMC	inter-metacarpal (joint, see Section Anatomical terms above)
LOOCV	leave-one-out cross-validation 42
MC	metacarpal (bone, see Section Anatomical terms above)
MCP	metacarpophalangeal (joint, see Section Anatomical terms above)52
MoCap	optical motion capture xiii
MPS	markers per segment 69
MRI	magnetic resonance imaging xiii
PIP	proximal interphalangeal (joint, see Section Anatomical terms above)
PD	<i>phalanx distalis</i> (bone, see Section Anatomical terms above)
PM	<i>phalanx media</i> (bone, see Section Anatomical terms above)
PP	<i>phalanx proximalis</i> (bone, see Section Anatomical terms above)
RMSE	square root of mean squared error 12
RoM	range of motion 15
SD	standard deviation 63
SNR	signal-to-noise ratio 24
STA	soft tissue artefact 2
STAMAS	Smart technology for artificial muscle applications in space (project, STAMAS [2013])
TZ	trapezium (bone, see Section Anatomical terms above)

Mathematical notation

a	scalar value
$f(\cdot)$	function

\mathbf{a}	vector
$\mathbf{a} \cdot \mathbf{b}$	dot product
$\mathbf{a} \times \mathbf{b}$	cross product
A	matrix
A^T	transpose of matrix
A^{-1}	inverse of matrix
$A_{(i:j,k:l)}$	sub-matrix of matrix A, obtained by deleting the rows $\{1, \dots, i-1\}$ and $\{j+1, \dots, n_{\text{rows}}\}$ and deleting the columns $\{1, \dots, k-1\}$ and $\{l+1, \dots, n_{\text{columns}}\}$ (if $i=j$ or $k=l$, one of them and the colon can be omitted)
AB	matrix product
$\prod_{i=1}^n A_i$	multiple matrix product, with $\prod_{i=1}^n A_i = A_1 A_2 \cdots A_n$
$\{a, \dots, b\}$	integer interval
${}^A \mathbf{a}$	coordinates of vector \mathbf{a} expressed in coordinate system A
${}^A T_B$	transformation from coordinate system B to coordinate system A, such that ${}^A \mathbf{a} = {}^A T_B {}^B \mathbf{a}$
$\text{Rot}(\mathbf{a}, q)$	3×3 rotation matrix of a rotation around an axis \mathbf{a} by an angle q :

$$\text{Rot}(\mathbf{a}, q) := \begin{pmatrix} c + c' a_x^2 & c' a_x a_y - a_z s & c' a_x a_z + a_y s \\ c' a_x a_y + a_z s & c + c' a_y^2 & c' a_y a_z - a_x s \\ c' a_x a_z - a_y s & c' a_y a_z + a_x s & c + c' a_z^2 \end{pmatrix}, \quad (1)$$

with

$$c = \cos q, \quad c' = 1 - \cos q \quad \text{and} \quad s = \sin q,$$

where a_x , a_y and a_z are the Cartesian elements of the unit orientation vector \mathbf{a} [Meyberg and Vachenauer, 1999, p. 319].



1

Introduction

The subject of this thesis is the modelling of the movement abilities (kinematic modelling) of the human hand, which is needed for the design of humanoid robotic hands.

Humanoid robotic hands are robotic hands that resemble human hands, especially with respect to their shape and their kinematic abilities. In some situations, humanoid robotic hands offer some advantages over other types of robotic grippers.

One such situation occurs when a robot is supposed to work with objects that are normally used by humans, for example as an assistant for a paralysed person. If its hand has the same shape, size and kinematic abilities as a human hand, it can take advantage of object properties (for example, handles) that are adapted to the human hand.

As another example, if a robot is tele-operated by a human operator, for example, in a hazardous situation like defusing a bomb, the operation will become simpler if the robot moves in the same way as the operator.

A third example is prosthetics, where it is often desired that the appearance of the prosthetic device is human-like. Human-like kinematics will help to create a human-like appearance.

In order to recreate the kinematic abilities of the human hand in a robotic hand, one needs to know what they are. In other words, the designer of a humanoid

hand needs to have a qualitative or quantitative model of the human hand kinematics.

Kinematic hand models are greatly simplified when regarding the hand as a set of rigid segments which are able to move with respect to each other. A hand posture is then described by the positions and orientations (poses) of each segment. This approximation is supported by the high elastic modulus of the bones and the relatively small thickness of the soft tissues compared to the overall hand dimensions. It is often used in the literature and also throughout most of this thesis.

The relative poses between neighbouring segments are constrained by joints. An important aspect of kinematic models is the description of the joint types, that is, of the kinds of movement between neighbouring segments that they allow. The joint types for some of the joints of the hand are a matter of dispute. In Chapter 3, a method is developed to select the appropriate joint types from a list of joint types based on measurements of hand postures and thresholds on the desired accuracy.

In the same Chapter, the method is applied to a set of magnetic resonance imaging ([MRI](#)) images of a human hand in order to determine the joint types at different accuracy constraints. A compromise between accuracy, simplicity and naturalness is found at the user's discretion.

In Chapter 4, the joint types are combined with joint parameters and surface shapes of the finger and palm segments in order to create a more complete hand model. This is the first generative hand model created from [MRI](#) images. A possible application of the hand model is shown by using it in grasp simulations. The grasp simulations are used to investigate the effect of different joint types in the thumb on the ability to grasp predefined objects. The human hand models are furthermore compared with a robotic hand model in order to discover possibilities for the improvement of the robotic hand.

For determining the joint parameters of a hand model it is necessary to measure hand postures. One of the most widely used methods is optical motion capture ([MoCap](#)), a system that tracks the positions of markers. The markers are attached to the surfaces of fingers and palm. Since the skin surface is able to move somewhat with respect to the underlying bone, the rigid-body assumption becomes less appropriate. The error that is induced by measuring skeletal postures using skin markers is called soft tissue artefact ([STA](#)). A reason for using [MRI](#) as measurement methods in Chapters 3 and 4 is to avoid [STA](#) by measuring bone poses more directly.

Chapter 5 is dedicated to the comparison between [MRI](#) and [MoCap](#) as mea-

surement methods for kinematic hand modelling. It is hypothesised that **MRI** measurements are more suitable for identifying the joint parameters of a rigid-body model than **MoCap** measurements due to lack of **STA**. Since ground truth about segment poses is not available, the inverse question is investigated as proxy, that is, whether a rigid-body hand model is able to reproduce the **MRI**-measured postures better than the **MoCap**-measured postures. It is assumed that if the model can better explain one of the measurements, then, conversely, the measurements can better be used to identify the model parameters.

The comparison between **MRI** and **MoCap** is carried out without any skin movement model, that is, the markers are assumed to be rigidly attached to the bone. However, using a model of the movement of the skin with respect to the bone, the accuracy of **MoCap**-based model could possibly be improved. One such model for skin movement near joints as a function of the skeletal movement was proposed by researchers Zhang et al. [2003]. However, so far it lacked a quantitative validation. In Chapter 6, this skin model is validated by using simultaneous **MRI** measurements of bones and skin markers as ground truth. In summary, this thesis proposes several methods for improving kinematic hand models and shows how they can be applied for improving the design of humanoid robotic hands.



2

Related work

In this Chapter, the state of the art of research related to hand kinematics is presented. It starts with an overview on robotic hands, continues with the description of work on the modelling of hand and finger joints and on the measurement of hand and finger segment poses and concludes with review of literature on how the kinematics of a hand affects its functionality.

2.1 Robotic hands

A fairly large number of humanoid robotic hand designs exists. On a website about robotic hands [Mindtrans.narod.ru, 2010–2013], 31 advanced robotic hand models and seven prosthetic hand models are listed. Most of them are humanoid robotics hands.

One of the first articulated artificial hands was the prosthetic hand of Götz von Berlichingen from the sixteenth century [Bertram, 2011]. In the eighteenth century intricate automata like piano-playing or handwriting automata were built [ABlogtoWatch.com, 2012]. The first five-fingered, electrically driven artificial hand was probably the Belgrade Hand by Tomović and Boni [1962]. It was conceived, but never used, as a prosthetic device [Bekey and Fermoso, 2008]. In 1986, the Utah/MIT Dextrous Hand [Jacobsen et al., 1986] was presented, which featured strong actuators connected to the finger joints by a complex and

large tendon routing mechanism. In the early nineties, the DLR Hand was built. It is a detachable four-fingered tendon driven hand containing all motors in the palm of the hand [Butterfass et al., 1998]. The DLR Hand II, which followed a few years later, was built without tendons, and featured modular fingers driven via gears [Butterfaß et al., 2001]. In Japan, the Gifu Hand was developed in several versions. It also contains the motors within the hand, making it detachable [Kawasaki et al., 2002]. One of the first commercially available dexterous hands is the Shadow Hand (Figure 2.1a), actuated via tendons by pneumatic muscles in the forearm [Kochan, 2005].

The Anatomically Correct Testbed (ACT) hand [Vande Weghe et al., 2004] (Figure 2.1b) aims at reproducing the biological structure of a human hand in a robotic hand as closely as possible. This remarkable testbed includes, for example, a complex crocheted replica of the extensor tendon apparatus. A goal is the replication of the kinematic and dynamic behaviour of the human hand. Regarding the kinematics, earlier versions used technical joints, whereas recently, a more true-to-nature approach with surface contacts is tested. However, the surface shapes are still approximated as spheres instead of the more irregular human joint surfaces [Xu et al., 2011].

Hydraulic actuation has been implemented in the Karlsruhe Anthropomorphic Fluidic Hands [Schulz et al., 2004]. It is used in the research humanoid platform ARMAR-III [Asfour et al., 2006] for assistant robotics in human-centered environments.

One of the first commercial modular hands is the four-fingered DLR/HIT/Schunk Anthropomorphic Hand [Liu et al., 2006]. A improved version, DLR/HIT Hand II, was presented in 2008 [Liu et al., 2008] (Figure 2.1c).

In the early 2010s, the DLR Hand Arm System was presented [Gebensteiner et al., 2011] (Figure 2.1d). It features variable passive stiffness in all joints. The hand of the DLR Hand Arm System (Awiwi hand) moves in 19 independent kinematic degrees of freedom (DoF), each of which are driven by two antagonistic motors in the forearm. This is more than the number of independent kinematic DoF of the human hand, some of whose joints are somewhat coupled. Therefore it is sometimes called “hyper-actuated”. The size of the fingers is within the 25th and 75th percentile of human size (Gebensteiner [2012], Figure 2.1). The DoFs are distributed as follows: thumb, index and middle finger: four each; ring and little finger: three each; palm arching: one. It differs from most other robotic hands in that the joint axes of the PIP¹ and DIP joints are neither fully parallel

¹For the meaning of the joint names see [Anatomical terms](#) and [Abbreviations](#) at the beginning of this thesis.

to each other nor exactly orthogonal to the bones. This so-called inclination leads to a radial or ulnar deviation of the phalanges during flexion, which is “e.g. important grasping a palm sized or small ball”. Furthermore, “it enables opposition of the little finger and thumb”. In addition,

the inclination rotates the phalanges toward the inside of the palm.

This rotation prevents (painful) contact of the sides of the fingers and enables contact of the pulp with the object. Performing small object power grasp, it also prevents lateral forces within the joints due to laterally oriented contact forces. [Grebenstein, 2012]

Like most robotic hands, the Awipi hand has four **DoF** in the thumb instead of the five **DoF** that most bio-mechanists find in human thumbs. However, Grebenstein claims:

The thumb TMC [=CMC1] placement and the twist and inclination of the thumb IP has been optimized to meet the requirements of the Kapandji test, used by surgeons to check grasping ability of human hands. Furthermore, grasping tests such as key grasp and large cylinder power grasp have been used to further fine tune these parameters. The combination of proper TMC joint placement and IP joint twist and inclination has shown to be able to adequately compensate the missing fifth thumb DoF of the Awipi Hand. [Grebenstein, 2012]

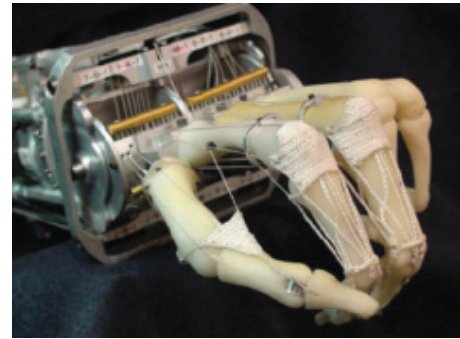
The inclination of the human fingers and the axes of the **MCP** joints are such that when the fingers are all flexed, their sides are pressed against each other and can only be separated with considerable effort. This can be a problem in robotic hands, since they generally lack the passive elasticity that the human hand possesses, and therefore, the fingers can block each other during flexion. This is especially the case if the robot fingers are wider at the tip than the human fingers.

Robonaut 2, the first humanoid robot in space, is also equipped with two dexterous robotics hands [TIME, 2012]. Their 12 **DoF** each are distributed such that the thumb has four **DoF**, index and middle finger three each and ring and little finger one each. Its size is “within 60th to 85th percentile human male” [Bridgwater et al., 2012] and it is able to emulate 90% of Cutkosky’s [1989] grasp taxonomy [Diftler et al., 2011] (Figure 2.1e).

There are many more robotic hand designs, and with **3D** printing technology becoming affordable, many new designs have been presented within a short time span, for example Gibbard [2013] (Figure 2.1f).



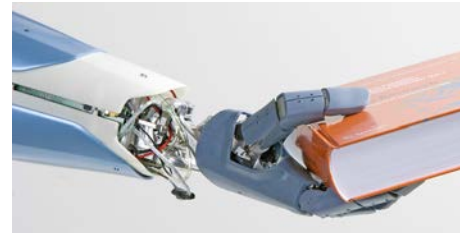
Shadow Hand. Picture by Richard Greenhill and Hugo Elias of Shadow Robotics, licensed under GNU-FDL.



Anatomically correct testbed hand.
Reprinted from [Deshpande et al. \[2013\]](#)
©2013 IEEE



DLR/HIT Hand II. Picture by Holger Urbanek of DLR.



The hand of the DLR Hand Arm System. Picture by DLR.



The hands of Robonaut 2. Picture by NASA.



Dextrus hand. Picture by Joel Gibbard, used with permission.

Figure 2.1: Examples of humanoid hands.

In summary, already many humanoid hand designs exist. Some of them are already quite advanced, also from the kinematics view point. But maybe some improvements can still be made.

2.2 Modelling of human hand and finger joints

Some aspects of the kinematic structure of human hands are apparent to the common senses, for example, that the hand has five digits.² The easily apparent aspects further include the number of bony segments per fingers, namely three. Some **DoF** are also easily apparent: the flexion/extension **DoF** of the interphalangeal joints, the flexion/extension **DoF** of the **MCP** joints and the abduction/adduction **DoF** of the **MCP** joints of index, middle, ring and little finger.

However, there are less apparent properties of the kinematic structure of the human hand that provoke scientific discussion and justify deeper probing. These include: the precise orientations of the joint axes; the exact positions of the joint axes and the link length ratios; especially, the positions and orientations of the joint axes of the carpometacarpal and intermetacarpal joints of the thumb and palm; the number of **DoF** of some joints; especially, which small movements should be considered and whether they occur due to active movement of the uninhibited hand or due to passive movement induced by external forces; and the type of movement that the bones perform around the joint, that is, nearly concentric or rather eccentric.

For example, it is disputed whether the **CMC1** joint possesses two or three **DoF**. The question was elaborately investigated by [Koebke \[1983\]](#). The **CMC1** joint connects the **TZ** bone of the carpus with the **MC1** bone. It is saddle shaped, that is, both joint surfaces are curved convexly in one direction and concavely in another direction. The joint surfaces are oriented such that the convex part of the **TZ** fits into the concave part of the **MC1** and vice versa. Two main movements take place: flexion/extension around the centre of the convex curvature of the **TZ** and abduction/adduction around the centre of curvature of the **MC1**. However, these main movements do not explain the rotation that the thumb tip undergoes during the movement from a flat-hand posture to opposition between the thumb and a finger. In a flat-hand posture, the thumb points towards the ulnar and slightly palmar direction of the hand, whereas in opposition, it points towards the ulnar and dorsal direction. Two competing

²For a number of reasons, individual hands may differ; for example, about 2 in 1000 humans are born with a (more or less developed) sixth digit [[Greene, 2008](#)].

explanations for this opposition movement have been proposed:

1. that the concave part of the **TZ** is curved in a way that the **MC1** bone rotates while maintaining close contact with the **TZ**, or
2. that the **MC1** bone rotates around its longitudinal axis while moving away from the **TZ** and thereby reducing the contact are to two small spots.

The first argument is supported by anatomical findings that there is indeed a suitable curvature in the joint surfaces [Kuczynski, 1975]. The second argument is supported by the fact that in cadaver dissection of arthritic hands, abrasions at the two expected spots were found [Koebke, 1983].

The goal of kinematic modelling is to find a mathematical description of the bone movements that reconstructs the actual movements that the human is able to perform. This is closely related to the field of *kinematic synthesis*, as for example described by Hartenberg and Denavit [1964]. Kinematic synthesis deals with “mechanisms created to meet certain motions specifications” [Hartenberg and Denavit, 1964]:

In the design of a mechanism for a given application, a decision must first be reached regarding the *type* of mechanism to be employed, as, for example, deciding between a cam or a linkage. The *number* of links and connections required to give the desired **DoF** must then be determined. Finally the required *dimensions* needed to bring about a particular motion must be deduced. In the broadest sense, kinematic synthesis thus consists of the three interrelated areas of type, number and dimensional synthesis. [Hartenberg and Denavit, 1964, Preface]

A special case of the dimensional synthesis is the calibration of robots, as, for example, described by Khalil and Dombre [2002]. Here the type of mechanism and the number of links is fixed in advance, and even the dimensions are known from the construction plans. The goal of robot calibration is to find out the differences in dimensions between the construction plan and the actual robot, which are due, for example, to the precision of the manufacturing process. So robot calibration is dimensional synthesis with good initial values.

In human joints, the number of links and connections is known as the number of bones and joints between them. The types of connections are sometimes a matter of dispute.

For example, Youm et al. [1978] investigated whether the **MCP** joint behaves like a simple rotational joint with a fixed centre of rotation (**CoR**) or like a

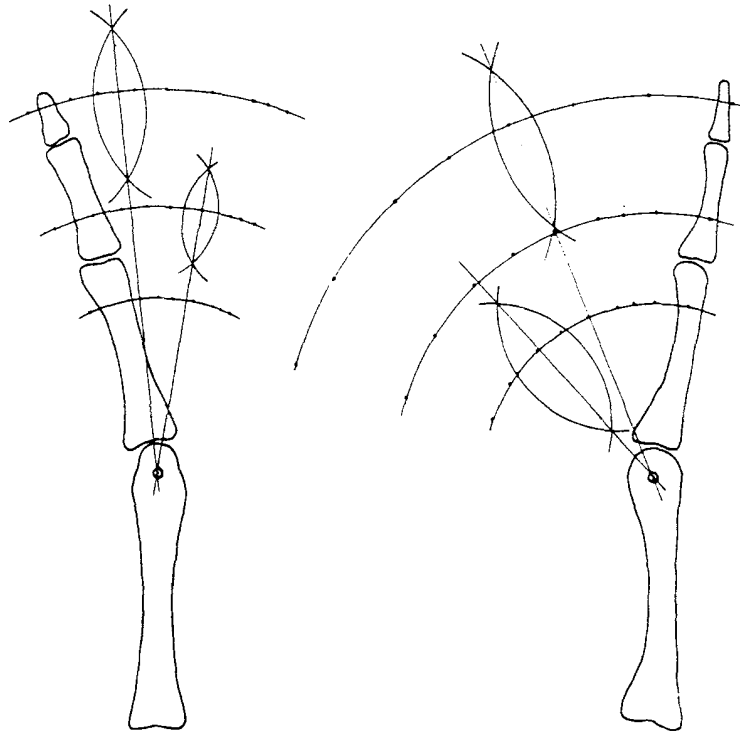


Figure 2.2: Construction of the CoR of the MCP joint. Left: radial and ulnar abduction. Right: flexion–extension movement. The measured positions of the landmarks on the phalanges are shown as faint dots. They all lie very close to circles around the CoR, so the CoR can be assumed to be fixed. Reprinted from Youm et al. [1978], Copyright (1978), with permission from Elsevier.

more complex cam-like joint with a moving CoR. For this, they constructed the CoR graphically from a set of positions of bony landmarks during planar movements measured using X-ray. In order to do so, they locked the PIP and DIP joints of a cadaver finger and recorded series of X-ray images during planar movements of the finger. The position of the CoR was constructed graphically from a number measured positions of landmarks on the phalanges. It turned out that different positions of a landmark during a movement are very close to a circle drawn around the CoR (Figure 2.2). Therefore, it can be assumed that the MCP joint behaves like a simple rotational joint with a fixed CoR.

Assuming fixed axes, the problem of the exact positions of the joint axes and the ratio of link lengths was tackled in 2D by Buchholz et al. [1992]. From measured trajectories of bony landmarks, they calculated centres of rotation using Rouleaux' method.

Sommer and Miller [1980] described “a technique for kinematic modeling of anatomical joints”. They presented a method based on numerical optimisation, with which they were able to determine the positions and orientations of multiple

axes of rotation that connect two rigid bodies. They used the technique to determine the locations of two wrist axes between the forearm (radius bone) and the palm ([MC2](#) bone).

An important issue in numerical optimisation is the choice of the cost function ϵ , as well as the calculation of its gradient. The cost function by Sommer and Miller was the sum of the squared differences between the measured and modelled palm coordinate system origins added to the squared differences between three Euler angles that describe the orientation of the palm coordinate system:

$$\epsilon = \sum_{t \in \mathcal{P}} \left[\sum_{i=1}^3 (r'_{it} - r_{it})^2 + \sum_{i=1}^3 (\psi'_{it} - \psi_{it})^2 \right],$$

where t is a time sample, \mathcal{P} is a set of measured postures, r'_{it} is the i -th coordinate of the measured position of the palm coordinate system with respect to the forearm coordinate system at time sample t , r_{it} is the corresponding coordinate of the modelled position, ψ'_{it} is the i -th Euler angle of the measured palm orientation with respect to the forearm orientation and ψ_{it} is the corresponding Euler angle of the modelled orientation.

In this thesis, a cost function different from the one of Sommer and Miller is developed, with the goal of providing a more intuitive interpretation of its value. Khalil and Dombre [2002] provide approaches on how to calculate the gradient of the cost function with respect to both the dynamic and the static variables. Cerveri et al. [2008] used the square root of mean squared error ([RMSE](#)) between measured and modelled marker positions as the cost function and minimised it in a nested optimisation, in which the joint angles were optimised in the inner loop using the Jacobian as a gradient and a Newton-Raphson optimiser, and the static parameters (axis position and orientation) were optimised in the outer loop using an evolutionary algorithm.

For spherical joints, the [CoR](#) can also be found with a closed-form solution [[Chang and Pollard, 2007a](#)]. A closed-form solution is desirable because of execution speed and repeatability. However, to the author's knowledge, for determining the axis orientations and positions of joints other than spherical joints, no closed-form solution is known.

A different approach to the determination of axis positions and orientations was taken by Cerveri et al. [2007]. They defined a 22-DoF kinematic model and used the positions of markers placed on anatomical landmarks such as joint knuckles in one static posture and measurements of joint thickness for determining the positions and orientations of the fixed rotation axes according to a defined algorithm.

Such chains of rotation axes that are fixed with respect to the parent axes have shown to be a suitable approximation for most finger joints. An exception to this is the CMC1 joint, where modelling with fixed rotation axes leads to larger residual errors than in the other joints [Stillfried and van der Smagt, 2010]. Therefore, Synek [2011, 2012] took a more complex approach to modelling the CMC1 joint. He simulated the movement of the CMC1 joint by balancing the forces of the joint surface contact, the tendons and the ligaments with the acceleration of the finger segment mass. Goß [2012] extended the simulation method to multiple joints in order to simulate the chain of middle finger phalanges. While he employed the simulation software Simpack with a special polygonal contact model in order to speed up the simulation, the computation times were still too large for many practical applications.

Van Nierop et al. [2008] presented an interesting biologically-inspired joint model in which two different curvatures are assumed for the joint surfaces of finger joints. This means that the positions of the rotation axes jump at certain points during movement. While may capture the human movement better, it is not straightforward to implement in a robotic joint.

Some researchers (for example, Moritomo et al. [2003], Miyata et al. [2005]), have used helical axes to describe measured skeletal movement. These represent exactly the movement between discrete measured poses and can be seen as an average of the instantaneous helical axes of the movement between the poses³. They are a useful tool for the qualitative description of the movement. However, since the helical axes are generally different for different poses, they do not constitute a *model* of the movement.

Sancho-Bru et al. [2011] proposed a “self-contained biomechanical model” including kinematics, tendons, muscles, ligaments, a contact model, a model for neural control and ergonomic evaluation criteria in order to evaluate grasps entirely in simulation, without the need for any measurement data.

In summary, models for single joints and limbs other than the hand have been created, as well as a whole-hand model based on MoCap. The contribution of this thesis to the topic of hand and finger joint modelling is described in Chapter 3. In contrast to most other works in literature (e.g., Rohling and Hollerbach [1994], Hollister et al. [1995], Cerveri et al. [2005, 2007]), it includes different joint type hypotheses and a method to choose from these, and it is the first complete hand model based on MRI.

³Woltring et al. [1987] have described a method for estimating the instantaneous helical axes using splines.

2.3 Measurement of human hand and finger postures

In order to measure the kinematic properties of human joints in detail, different methods have been applied. Due to their rigid nature, it is much easier to mathematically describe the movement of the bones than that of the soft tissues surrounding them. This poses the problem of how to measure the movement of the bones.

One approach is to cut open the skin and insert screws or needles into the bone in order to attach a measurement device rigidly to the bone. Due to its invasive nature, this method has mostly been applied *ex vivo*.⁴

For example, Manter [1941] investigated the movement of the subtalar joint with the calcaneus fixed and the talus mobile. He bolted rods to the talus to determine the plane of rotation as well as the position of the rotation axis.

As an example of an invasive method on the hand, Hollister et al. [1992, 1995] attached a mechanical axis-finder to bone pairs in the thumbs of cadaver hands. The axis finder consisted of one or two mechanical axes whose positions and orientations relative to the bone attachment locations could be varied. The axes were adjusted manually while moving the joint until the axes remained stationary during the joint movement. The result was recorded using photographs, in which the axis locations relative to the bone or finger shapes are visible.

Another method is to leave the skin intact and record the bone poses with medical imaging. Imaging methods with ionising radiation (X-ray and computed tomography (CT)) produce a good contrast between bone and surrounding tissues. However, since they can cause cancer, they are usually only used *in vivo* if medically necessary or *ex vivo* for research purposes.

For example, Pearcy and Whittle [1982] tracked poses of the vertebrae of the lumbar spine by calculating 3D positions of anatomical landmarks from biplanar radiographs. In a combination of invasive and imaging methods, Lundberg et al. [1989] inserted “three or more beads of tantalum” into each of seven bones and recorded their positions using X-ray stereophotogrammetry, in order to measure postures of the ankle.

Buchholz et al. [1992] took planar X-ray images of finger joints *ex vivo* during flexion/extension movements and used bony landmarks for tracking planar bone movement. In MRI, the contrast is not as good, the grey values do not only depend on the tissue type but also on the surrounding tissue and the location in the MRI scanner, but it is considered safe for human usage [Dempsey et al., 2002].

⁴For STA measurements in joints other than finger joints, invasive experiments have also been carried out *in vivo*. References to those experiments are found in [Leardini et al., 2005].

Kamojima et al. [2004] recorded **MRI** images of a hand *in vivo*. They segmented the bones manually from one of the volume images. To determine the relative poses of the bones in the other images, they did a manual pre-registration and a subsequent automatic registration by maximising the intensity values inside the registered volume. Also in this thesis, **MRI** is used for measuring bone poses. The registration of the bone point clouds is accomplished by an algorithm from **3D** robotic vision (Section 3.1.1).

A third method is measuring positions of points on the skin or fingernail and inferring the bone pose by ignoring or modelling the relative movement between skin and bone. Usually, for these measurements, markers are attached to the skin and their positions are measured by stereophotogrammetry. Even though there are also methods for markerless, video-based measurements of hand posture, to the author's knowledge they always require an existing model of the kinematic structure and cannot be used to make measurements for creating a model of the kinematic structure.

As Lundberg [1996] wrote, the mathematical methods for stereophotogrammetry (calculating **3D** positions from **2D** images) have been known in the field of geological survey for a long time. With computers taking over the calculating effort, stereophotogrammetry has become frequently used also in biomechanical analysis. The earliest examples mentioned by Lundberg are from 1992 and deal with the movement of the knee (Koh et al. [1992] in Lundberg [1996]).

Rohling and Hollerbach [1993] used a single light-emitting diode marker on a fingernail in combination with an exoskeleton that measured the joint angles to create a kinematic model of the finger joints. Cerveri et al. [2005] placed multiple markers on all segments of the hand and measured their positions during movements that involved “the action of all the functional **DoF** with wide range of motion (**RoM**)s of the fingers and dorsum”.

In summary, *in vitro* and *in vivo* measurement methods of the bones and of the skin have been developed. In this thesis, both optical and **MRI** measurements are taken and the residual errors of models based on these two modalities are compared. The measurements are described in Chapter 5.

2.4 Measurement, modelling and compensation of skin movement

Frequently, surface-based measurements are used in biomechanics to infer skeletal kinematics. However, these measurements suffer from **STA**, i.e., from errors due to relative movement between the skin and the bone.

The causes for STA are described by Leardini et al. [2005]:

Inertial effects, skin deformation and sliding, which occur mainly in areas closer to the joints, and deformation caused by muscle contractions, contribute independently to STA. Because of its nature, the artifact has a frequency content similar to the actual bone movement and it is therefore very difficult to distinguish between the two by means of any filtering technique.

In the literature, different researchers dealt with the problem of STA. They used different methods to measure STA and proposed different methods for compensating it. For measuring bone motion, some researchers used percutaneous invasive methods (bone pins, external fixtures), medical imaging (X-ray, CT, fluoroscopy, MRI) and palpation of anatomical landmarks on the bones (see reviews by Leardini et al. [2005] and Peters et al. [2010]). Additional markers were fixed to the skin, and the movement of both the skin and bones was measured. Most of the these works dealt with the lower limb.

The percutaneous methods provide the possibility of tracking bone poses very accurately, because the percutaneous structures are in direct contact with the bones. Whereas intracortical bone pins and external fixtures are fixed to the bone by screws that enter the bony material, the bone tracking device only penetrates the periosteum surrounding the bones and ensures a stable connection by clamping the bone from different sides. On the downside, the invasive methods leave the subjects with the risk of scars, pain and infection; furthermore, the percutaneous structures interfere with the skin movement, thereby introducing an error into the STA measurements.

Medical imaging can be used to measure bone poses without interfering with the skin movement.

In order to measure STA, different methods have been applied, and many of them are described in a paper by Leardini et al. [2005].

Unconstrained skin movement was measured with medical imaging methods, such as X-ray, CT and MRI. The movement of the bones was calculated by image registration or by tracking previously implanted markers. The first work using MRI to measure STA and also the first work measuring STA on the hand was, according to the author's knowledge, by Ryu et al. [2003, 2006]. They measured the relative movement between skin and bone by analysing MRI images of bones and skin markers of six subjects in three postures. They published the results for the skin over the MC2 bone, which moved up to 11 mm relative to the bone. Researchers of the Dexmart project [Corato et al., 2009] took similar

measurements, with one subject and two hand postures, and obtained similar results. They published results for marker movements over two metacarpal bones, one phalangeal bone and over the carpus. In order to obtain a more comprehensive view, with STA values for all bones and joints of the hand, further MRI measurements are conducted as part of this thesis in Section 6.1.1.

Sometimes apparatuses are used to constrain the relative movement, for example, by Marin et al. [1999]. Also identifying the postures of kinematic chains instead of poses of single segments can be used to mitigate the effect of STA [Leardini et al., 2005]. Another interesting approach for reducing STA is locking one joint and measuring the pose of the newly formed rigid body at a place where the skin is less mobile (Lucchetti et al. [1998] in Leardini et al. [2005]).

The most simple model is a rigid connection. It is frequently used, for example, by Cerveri et al. [2005], but the resulting STA is arguably the largest of all possible models. Models of skin-vs.-bone movement include translational movement, either as a linear function of the joint angles [Dumas and Cheze, 2009] or as a non-linear function [Corato et al., 2009], and a rotational movement as linear or non-linear function of the joint angles [Zhang et al., 2003].

In the literature, there are two different models of skin movement on the hand and fingers: Zhang et al. [2003] model the movement of skin markers near joints as a rotation around the skeletal joint axis; Corato et al. [2009] modelled the movement of skin markers as translations along the axes of the bone coordinate system. In the following, both skin models are explained. Soft tissue movement models in other body parts include a lookup table [Cappozzo, 1984] and a multilinear regression model [Gao, 2009].

The rotational skin movement model by Zhang et al. aimed to explain the movement of skin markers near the MCP, PIP and DIP joints of the fingers during flexion/extension movements of these joints. The markers attached to the fingertips were considered to be fixed to the PD bones. Skin movement was treated as a 2D problem in the sagittal plane⁵. The main components of the model are shown in Figure 2.3. The finger number was indicated by the index $i \in \{2, \dots, 5\}$ and the joint number was indicated by the index $k \in \{1, \dots, 3\}$. The distances L_k^i between centres of rotation C_{k-1}^i and C_k^i and the distances d_k^i between CoR C_k^i and the marker M_k^i were assumed to maintain constant length. This also applied to the distance L_1^i between the fingertip marker M_0^i and the DIP CoR C_1^i . The angle α_k^i between the line connecting C_k^i and M_k^i and the line connecting C_{k-1}^i and C_k^i was modelled as a function of the angle θ_k^i between the line connecting M_{k-1}^i and M_k^i and the line connecting M_k^i and

⁵flexion/extension plane, see Anatomical terms at the beginning of this thesis.

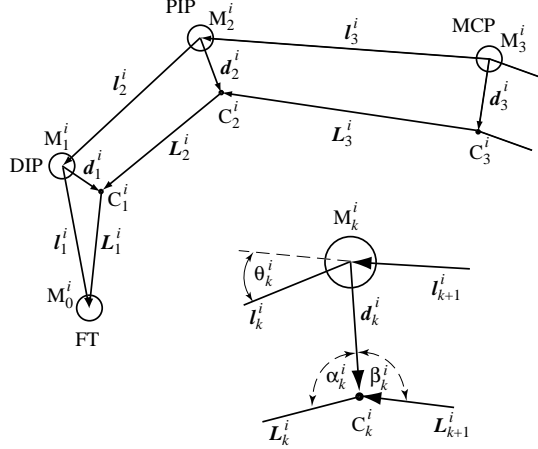


Figure 2.3: The rotational skin movement model by Zhang et al. [2003]. Reprinted from [Zhang et al. \[2003\]](#), Copyright (2003), with permission from Elsevier.

M_{k+1}^i :

$$\alpha_k^i(t) = g(\theta_k^i(t)).$$

Specifically, a linear function was chosen:

$$\alpha_k^i(t) = c_k^i \theta_k^i + \delta_k^i.$$

The parameters c_k^i , δ_k^i and d_k^i were optimised to minimise the variation in internal link length L_k^i . The resulting values for c_k^i ranged from 0.27 to 0.47 and those for d_k^i from 0.48 to 0.67 of measured corresponding joint thickness. Zhang et al. [2003] considered the values for d_k^i plausible. Values close to 0.5 for d_k^i mean that the joint centres were close to the middle of the bone. A plot of the measured marker positions with respect to their proximal modelled bones showed an approximately circular trajectory, which further supports this model. However, the model has been lacking a complete quantitative validation. To fill this gap, a validation of the skin movement model is done in Chapter 6 of this thesis.

In their translational skin model, the Dexmart project [2009] postulated that a skin marker i moves along the Cartesian directions of the corresponding bone coordinate system with distances depending on the joint angles:

$$\mathbf{m}_i = \begin{bmatrix} \phi_x(\theta) & 0 & 0 \\ 0 & \phi_y(\theta) & 0 \\ 0 & 0 & \phi_z(\theta) \end{bmatrix} \mathbf{w}_i,$$

where \mathbf{m}_i is the marker position in the parent bone coordinate system in homo-

geneous coordinates, \mathbf{w}_i are model parameters and $\phi(\theta)$ are polynomial regression functions of the distances with respect to the joint angles. The order of the polynomial is chosen separately for each component. A greedy algorithm was used for choosing the order and the coefficients of the polynomials. The model was quantitatively validated.

The Dexmart model was applied in four trials to an index finger and thumb (32 markers on a latex glove). Joint axes and marker movement parameters of the translational model were optimised. The RMSE between the measured and modelled marker positions was 0.91–1.02 mm with a rigid model and 0.66–0.80 mm with a moving-marker model. The percentage improvement was 18.2–27.8%.

In summary, STA has been measured invasively and non-invasively. In this thesis, such measurements are presented for the first time for all segments of the hand. Rotational and translational models for skin movement have been presented in literature. The rotational model was not yet quantitatively validated, which is done in Chapter 6 of this thesis.

2.5 The role of the kinematic structure for the practical abilities

A goal of the kinematic measurements is trying to understand how the functionality of the hand depends on its kinematic properties.

Jones and Lederman [2006] started their book *Human Hand Function* with a description of the abilities of the hand:

The human hand is a miraculous instrument that serves us extremely well in a multitude of ways. We successfully use our hands to identify objects and to extract a wealth of information about them, such as their surface texture, compliance, weight, shape, size, orientation, and thermal properties. We demonstrate impressive manual dexterity when reaching for, grasping, and subsequently manipulating objects within arm's reach. Manual gesture, such as those used in sign language and finger spelling, collectively offer valuable forms of communication to those who are deaf or hearing impaired. [...]

The book “analyzes and synthesizes the results of fundamental research drawn from a broad range of disciplines that contribute in important ways to our understanding of human hand function.”

The hand surgeon Kapandji [1992] described in his book *Physiology of the Joints* the anatomy of the hand and its kinematic capabilities. He listed a taxonomy of different grasp types and provided functional examples in which these grasp types are used. He further summarized other functions of the hands, such as percussion, contact and signaling. As a means of understanding the functional role of the kinematic structure of the hand, he devised alternative structures in thought experiments and pointed out the things that those hands could not do anymore. A further taxonomy of grasp types was provided by Cutkosky [1989] and extended by Feix et al. [2009].

Gebensteiner [2010, 2012] described how different grasp types (pinch, key, power, sphere) depend on kinematic properties such as thumb CMC joint position and orientation and fingertip rotation, intersection of thumb and index finger tip workspace, finger MCP first axis orientation, finger medial and distal phalanx reorientation with flexion, palmar arching and rotation of the little finger workspace towards the thumb.

Lewis [1977] compared the shapes of human and other primates' joint surfaces, especially of the CMC and MCP joints, and demonstrated "that the human joints have been quite strikingly modified in a number of ways, and that these evolutionary changes may be logically correlated with the refined functional attributes of the human hand."

Iberall [1997] presented "an analysis of human prehensile capability [...], comparing a symbolic description of prehension to an opposition-space, parameterized framework. By pointing out features of the human hand in prehensile tasks," she hoped "to offer insights that designers can use for building more versatile robot and prosthetic hands."

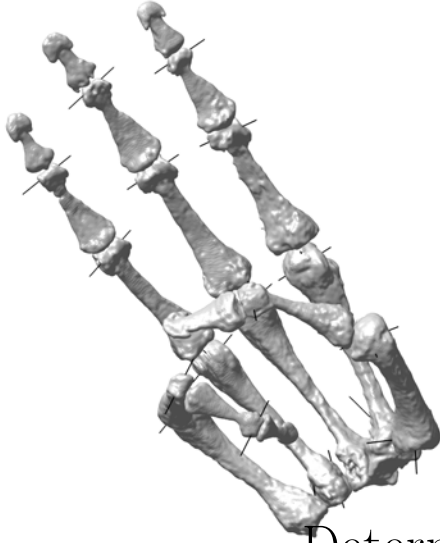
Chalon et al. [2010] published guidelines for robotic thumb design, some of which concerned kinematic aspects and were related to hand functionality.

Further understanding of the role of kinematic properties for the functionality of the hand are provided by simulations of grasps with different hand models. Fairly extensive work in the field of grasp simulation has been done by Miller, Ciocarlie and Allen around their grasp simulator GraspIt! [Miller, 2001], which contains a human hand model. The axes of its thumb joints are placed such that they optimally fit a model to measured electromyographic (EMG) signals and fingertip forces. The finger joint axes are simply three parallel axes and one orthogonal axis. The surface is taken from animation software. GraspIt! allows automatic planning and evaluation of grasps, by using so-called eigengrasps, a low-dimensional representation of the joint angle space in which most of the common hand movements are covered [Allen et al., 2009]. Different hand models

and objects can be loaded.

Diankov [2008, 2010] developed the open-source software OpenRAVE, an environment for planning, simulation and automatic execution of robotic manipulation. It strongly focuses on modularity in order to allow users to test specific parts of software, for example, planning algorithms, without having to deal with all other aspects of the simulation such as kinematics, collision detection and visualisation. The software OpenGRASP is an extension of OpenRAVE that was developed within the GRASP European Commission ([EC](#)) project [[León et al., 2010](#)]. It includes “plugins for specific sensors used to improve the grasping capabilities of the robot”, “more physics engines and collision checkers that helps to compare and improve the simulation performance”, “a standard plugin interface of a basic actuator”, an abstraction layer for physics engines, utilities for creating robot and object models, as well as set of robotic hand models [[GRASP, 2011](#)].

In summary, some insight on how kinematic properties affect the functionality of the hand exists, but the picture is far from complete. Grasp simulations may be a useful tool for further exploring the role of the kinematic properties for hand functionality.



3

Determination of joint types

In this Chapter, which is based on [Stillfried, 2009] and [Stillfried et al., 2014], the selection of joint types of the human palm and finger joints is presented.

3.1 Methods

For the selection of joint types, a list of joint types is defined, finger segment poses are measured, the joint parameters are adapted to the measurements and the residual error between modelled and measured segment poses is calculated. A threshold on the mean residual error is defined and the simplest joint type whose residual error is lower than the threshold is selected.

3.1.1 Measurements of finger segment poses using MRI

In the following Section, the processing steps from image acquisition to segment pose are described. They involve the segmentation of the 3D images, the reduction of the segmented volumes to point clouds and the alignment (registration) of the point clouds of the same bones in different images.

MRI images and segmentation

The MRI images are taken on a Philips Achieva 1.5 T unit, with a Philips SENSE eight-channel head coil to receive a more homogeneous signal and to improve

the signal-to-noise ratio (**SNR**). For a given object of interest and a given **MRI** sequence, **SNR** is proportional to the voxel¹ volume and to the square root of the net scan duration:

$$r \propto v\sqrt{t}, \quad (3.1)$$

where r is the **SNR**, v is the voxel volume and t is the net scan duration, that is, the time actually spent for signal acquisition. Thus for every application an individual compromise has to be found optimally balancing the needs for a small v (high spatial resolution), small t (short scan times to minimise potential motion artefacts) and large r (image quality sufficient for either diagnosis or—as in this case—the segmentation of certain anatomic structures).

An optimal compromise is found with a total scan duration (which is always longer than the net scan duration) of between two and two and a half minutes and a spatial resolution of $(0.76 \text{ mm})^3$. Note that, from Equation (3.1), a voxel volume of $(0.38 \text{ mm})^3$ would require 64 times the scan duration in order to achieve the same **SNR**. To further minimise motion artefacts the hand is stabilised using modelling clay. For post-processing, the spatial resolution is interpolated to $(0.38 \text{ mm})^3$ in order to achieve sub-voxel resolution in the segmentation process. In the processing step after the segmentation, the grey value information is discarded. The interpolation helps retain some of the information that is contained in the grey values.

For scanning, a sequence type called balancedFFE is used (also known as true-FISP or balancedSSFP) with $T_R/T_E/\text{flip angle} = 4.8 \text{ ms}/2.4 \text{ ms}/45^\circ$. The repetition time T_R is the time between two successive excitation pulses. The transverse component of the magnetization is read out at echo time T_E after each pulse.

The advantage of balancedFFE is that it yields a strong signal at short T_R . (In fact, the signal of the balancedFFE sequence becomes independent of T_R , which can be as low as 2.5 ms with the limiting factors being the readout time and the avoidance of peripheral and heart muscle stimulation.)

As a drawback, balancedFFE is prone to the so-called banding artefacts appearing as black stripes across the bone. This artefact can in principle be overcome by applying the balancedFFE offset averaging technique (also known as CISS or FIESTA-C), but requires twice the scan time.

Another artefact occurring in these sequences is opposed phase fat/water cancelling, where voxels containing both fat and water appear dark, because the magnetisation vectors of fat and water point in opposite directions.

¹voxel “volume pixel” = basic volume element of a **3D** image; analogous to *pixel* in **2D** images

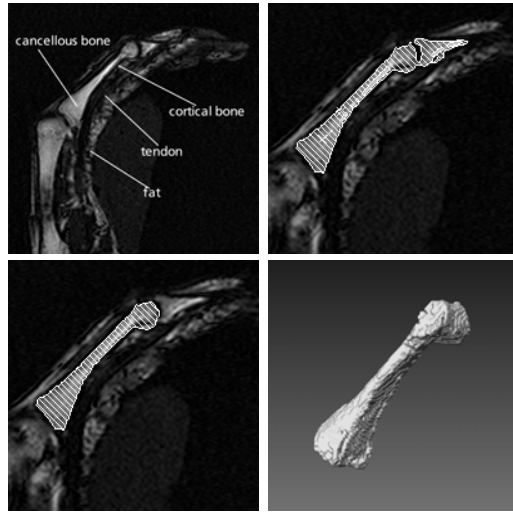


Figure 3.1: Segmentation process. *Top left:* Slice of an [MRI](#) image, showing the middle finger metacarpal (MC3). Tissue types can be discriminated by the intensity of the signal that is emitted. Segmentation is done at the boundary between cancellous and cortical bone. *Top right:* Threshold-based preselection. *Bottom left:* Manually refined selection. *Bottom right:* Segmented volume consisting of the selected areas from all slices. Reproduced from [Stillfried et al. \[2014\]](#).

Also a so-called cine-sequence, a continuous-motion sequence with two to five images per second, is recorded. However, only one image layer for the whole hand can be recorded, which renders this method unusable for the purpose of exact bone localisation.

The images are taken of a 29-year-old female subject with no history of hand problems who gave informed consent to the procedure. 51 images are taken in different hand postures with the aim of reflecting each joint's range of motion. From the [MRI](#) volume images, the bones are segmented. In fact, not the whole bone volume is segmented but the signal-intense volume inside the bone that corresponds to the cancellous bone. The tissue between the trabeculae of the cancellous bone is bone marrow consisting mainly of fat, which yields high signal intensity in the balancedFFE sequence.

The cortical bone, which forms the outer calcified layer of the bone, hardly contains any free fat or water protons and therefore stays dark in the [MRI](#) image. Near the bones there are other low-signal structures like tendons, which makes it difficult to determine the outer bone surface. Therefore, the boundary between cancellous and cortical bone is used for segmentation (Figure 3.1).

The bones are segmented from the image by highlighting the cancellous bone area in each slice of the [MRI](#) image. In the medical imaging software Amira (Visage Imaging GmbH, Berlin, Germany), the area is preselected by adjusting a threshold and refined manually (Figure 3.1).

Motion estimation

For the purpose of estimating the rigid motion of bones between different hand postures, some geometric structure rigidly related to each bone has to be extracted from the [MRI](#) images that can be reliably recovered with little shape variation between images. Automatic reconstruction of the bone geometry is a challenge, as the image density of cancellous bone, cortical bone and surrounding tissue can vary greatly between and across images. Also manual segmentation, besides being tedious work, is prone to introducing shape variation.

Hence a double strategy is pursued. The border between cancellous and cortical bone often produces a marked contrast edge at reproducible locations. These border points can hence be detected by selection of high-contrast points. In the absence of such a marked density contrast, on the other hand, guidance by manual bone segmentation is needed. This double strategy is implemented as follows. First, the bone segments are padded with zero-density voxels to fit in a cuboid volume. Then a dipolarity score of the padded density within each $3 \times 3 \times 3$ -voxel sub-volume is computed, as

$$\text{Dipolarity}(c_1, c_2, c_3) = \left\| \sum_{\substack{(i,j,k) \in \{c_1-1, c_1+1\} \\ \times \{c_2-1, c_2+1\} \\ \times \{c_3-1, c_3+1\}}} I(i, j, k) \begin{pmatrix} i - c_1 \\ j - c_2 \\ k - c_3 \end{pmatrix} \right\|.$$

Here $I(i, j, k)$ is the [MRI](#) image density as function of the voxel indices (i, j, k) , and (c_1, c_2, c_3) are the indices of the centre voxel within the $3 \times 3 \times 3$ -voxel sub-volume. The sum computes the density-weighted centroid of voxels around the voxel at (c_1, c_2, c_3) ; its Euclidean norm quantifies the degree of dipolarity of the density at the centre voxel. It attains high values for centre voxels close to a strong density edge. Finally, the centre voxels with the top q percent of dipolarity are selected as representing bone-related points. The grey value information is discarded in the selected points, but the interpolation mentioned in Section 3.1.1 is used to refine the point set. The quantile q is chosen to produce a data set of between 2,000 and 20,000 points, depending on the size of the bone. This way, points on the manually determined bone border are selected in the absence of high-contrast edges in the image; while high-contrast image edges dominate the selected points where available.

The above procedure produces sets of points that are close to the surface of the bones. However, missing parts and shape variation cannot be avoided. Moreover, there is no correspondence of points across different data sets of the same

bone. A robust estimator of motion between such data sets hence has to be employed. A correspondence-free alignment that is also robust to geometric deviations [Hillenbrand, 2010] is provided within the framework of parameter-density estimation and maximization, or parameter clustering. This is a robust estimation technique based on location statistics in a parameter space where parameter samples are computed from data samples [Hillenbrand, 2007, Hillenbrand and Fuchs, 2011]. The estimator may be viewed as a continuous version of a generalised, randomised Hough transform. In the present variant, samples are drawn from the 3D points selected through the high-dipolarity criterion above. Let $X, Y \subset \mathbb{R}^3$ be the point sets extracted from two MRI images of the same bone. A motion hypothesis can be computed from a minimum subset of three points from X matched against a minimum subset of three points from Y . The sampling proceeds thus as follows:

1. Randomly draw a point triple $\mathbf{x}_1, \mathbf{x}_2, \mathbf{x}_3 \in X$;
2. Randomly draw a point triple $\mathbf{y}_1, \mathbf{y}_2, \mathbf{y}_3 \in Y$ that is approximately congruent to the triple $\mathbf{x}_1, \mathbf{x}_2, \mathbf{x}_3 \in X$;
3. Compute the rigid motion that aligns $(\mathbf{x}_1, \mathbf{x}_2, \mathbf{x}_3)$ with $(\mathbf{y}_1, \mathbf{y}_2, \mathbf{y}_3)$ in the least-squares sense;
4. Compute and store the six parameters of the hypothetical motion.

Random drawing of approximately congruent point triples in step 2 of the sampling procedure is efficiently implemented using a hash table of Y -point triples indexed with the three X -point distances ($\|\mathbf{x}_1 - \mathbf{x}_2\|, \|\mathbf{x}_2 - \mathbf{x}_3\|, \|\mathbf{x}_3 - \mathbf{x}_1\|$) as the key. Least-squares estimation of rigid motion in step 3 computes the rotation $R \in \text{SO}(3)$ and translation $\mathbf{t} \in \mathbb{R}^3$ as

$$\begin{aligned} \{R, \mathbf{t}\} = \arg \min_{\{R', \mathbf{t}'\} \in \text{SE}(3)} & [\|R' \mathbf{x}_1 + \mathbf{t}' - \mathbf{y}_1\|^2 \\ & + \|R' \mathbf{x}_2 + \mathbf{t}' - \mathbf{y}_2\|^2 + \|R' \mathbf{x}_3 + \mathbf{t}' - \mathbf{y}_3\|^2]. \end{aligned}$$

The special three-point method of Horn [1987] is used to obtain a closed-form solution. The parametrisation of rigid motions chosen for sampling step 4 may have an influence on the result. In fact, the parameter density from which the samples are taken depends upon this choice. A parametrisation that is consistent for clustering is used here, in the sense of Hillenbrand [2007].

By repeatedly executing the sampling procedure 1–4 above (in the order of 10^6 times), samples are obtained from the parameter density for the rigid alignment

problem. This parameter density is similar in spirit to a posterior density, but without assuming a probabilistic observation model.

The parameter samples can be stored in an array or a tree of bins. The sampling stops when a significant cluster of samples has formed, as judged from the bin counts. Then the location of maximum parameter density is searched by repeatedly starting a mean-shift procedure [Fukunaga and Hostetler, 1975, Comaniciu and Meer, 2002] from the centre of the bins with high parameter counts. From all the local density maxima found through mean shift, the location in the six-dimensional parameter space of the largest maximum is returned as the motion estimate of a bone, in the following denoted as R_e and t_e . Details of the implementation are presented elsewhere [Hillenbrand and Fuchs, 2011].

The main sources of error in the procedure for estimating bone motion are

- the variation in bone geometry erroneously represented in the point sets extracted from different images of the same bone, resulting from variation in manual segmentation or dipolarity values computed from the images;
- the approximate rotational symmetry about the longitudinal axis of a bone, especially in case of poor geometric representation lacking shape details.

To get rid of grossly wrong motion estimates, an interactive cluster analysis is performed on the estimated rotations. Making use of the stochastic nature of the estimation algorithm, each motion estimate is repeated 100 times with different subsets of the data being sampled, resulting in motion estimates $\{R_{e1}, t_{e1}\} \dots \{R_{e100}, t_{e100}\}$. If the rotational distance between any two of the 100 motion estimates exceeds a threshold, clusters of rotation parameters are identified and the correct cluster $\mathcal{C} \subset \{1, \dots, 100\}$ is selected through visual inspection (Figure 3.2).

The rotational distance between two rotations is defined as the angle of a third rotation that would have to be appended to the first rotation in order to make it identical to the second rotation. It is calculated as follows:

$$\text{RotationalDistance}(R_1, R_2) = \arccos \left(\frac{1}{2} (\text{trace} (R_2 R_1^{-1}) - 1) \right), \quad (3.2)$$

where R_1 and R_2 are the rotation matrices of the first and second rotation.

The final rotation estimate \bar{R} is determined as the rotation that minimises the sum of squared rotational distances to all rotations in the cluster, that is, the

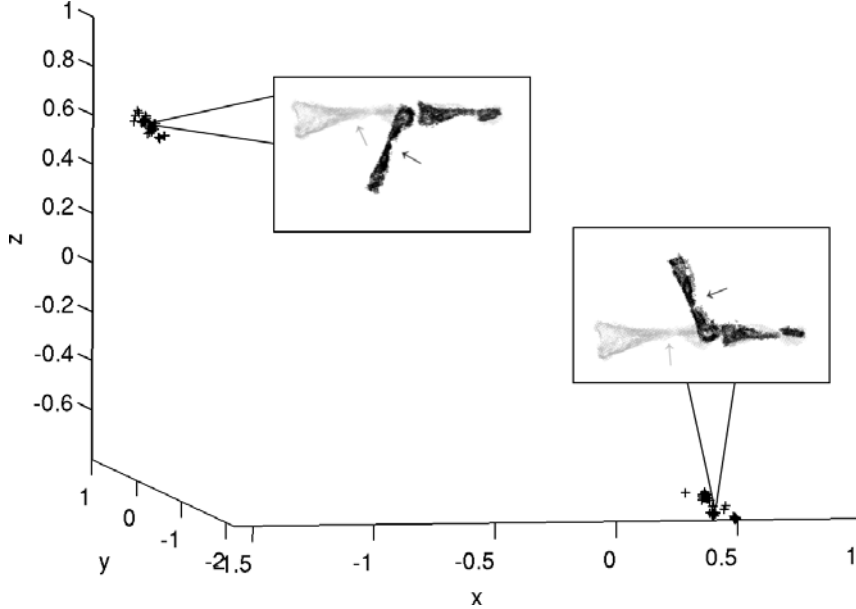


Figure 3.2: Visual inspection of pose estimates. The rotational part of 100 randomly repeated pose estimates is plotted in three dimensions as the product of rotation axis and angle. In this example there are two distinct clusters. One element in each cluster is inspected by regarding the more strongly curved side of the neighbouring bone (arrows). The motion of the *bottom right* cluster element implies a large, anatomically impossible, longitudinal rotation of the bones. Therefore the *top left* cluster is taken as the correct cluster \mathcal{C} . Reproduced from Stillfried et al. [2014].

mean rotation in the difference-rotation-angle metric,

$$\bar{R} = \arg \min_{R' \in \text{SO}(3)} \left[\sum_{i \in \mathcal{C}} \text{RotationalDistance}(R', R_{ei})^2 \right]. \quad (3.3)$$

Likewise, the final translation estimate $\bar{\mathbf{t}}$ is determined as the translation that minimises the sum of squared Euclidean distances to all translations in the cluster, that is, the ordinary mean value of valid translations,

$$\bar{\mathbf{t}} = \frac{1}{n} \sum_{i \in \mathcal{C}} \mathbf{t}_{cei}, \quad (3.4)$$

where n is the number of elements in the correct cluster \mathcal{C} , and \mathbf{t}_{cei} is the i -th translation estimate of the bone centroid. The translation estimate of the bone centroid is calculated as follows:

$$\mathbf{t}_{cei} = R_{ei} \mathbf{c} + \mathbf{t}_{ei} - \mathbf{c},$$

where \mathbf{c} is the bone centroid, that is, the mean of all points in X . If the correct cluster contains less than ten elements, the respective bone pose is discarded

from the modelling process. Furthermore, all pose estimates are checked optimally and obviously wrong estimates are discarded.

A natural confidence weight of the final rotation estimates is obtained from the variance of the sample mean values, that is,

$$\sigma_r^2 = \frac{1}{n(n-1)} \sum_{i=1}^n \text{RotationalDistance}(\bar{R}, R_{ei})^2. \quad (3.5)$$

This confidence weight enters in the estimation of orientation of rotational axes for the kinematic hand model below. Likewise, a confidence weight of the final translation estimates is given by

$$\sigma_t^2 = \frac{1}{n(n-1)} \sum_{i=1}^n \|\bar{t} - t_{cei}\|^2, \quad (3.6)$$

and used in the estimation of the position of rotational axes for the kinematic hand model below.

The standard deviation of the rotation and translation estimate over the 100 repetitions with randomly permuted point sets, that is, the square root of the variance described in Equations (3.5) and (3.6), is a measure of the repeatability of the motion estimations.

List of postures

The postures of which [MRI](#) recordings are made are selected such that the [RoM](#) of each joint is covered. They include the thumb–finger oppositions of the thumb function test by Kapandji [1986], as well as variations of these. The complete list of recorded postures is shown in Table 3.1, Figure 3.3 and Figure 3.4.

The list includes 51 postures. Since the aim of the kinematic modelling based on these measurements is to recreate the *active* kinematics of the hand, six postures that involve passive motion due to external forces are excluded, so that 45 postures are used for the identification of joint axes.

Table 3.1: List of recorded hand postures

number	description
1*	opposition of finger tips of thumb and index finger
2	opposition of finger tips of thumb and middle finger
3	opposition of finger tips of thumb and ring finger
4	opposition of finger tips of thumb and little finger
5	opposition of finger nails of thumb and index finger

Table 3.1: (continued)

number	description
6*	opposition of finger nails of thumb and middle finger
7	opposition of finger nails of thumb and ring finger
8	opposition of finger nails of thumb and little finger
9	flexion of thumb
10*	adduction of thumb
11	flexion of PIP and DIP
12*	extension of all joints (planar hand)
13	opposition of finger pads of thumb and index finger (flat IP and DIP joints)
14	opposition of finger pads of thumb and middle finger (flat IP and DIP joints)
15	opposition of finger pads of thumb and ring finger (flat IP and DIP joints)
16*	opposition of finger pads of thumb and little finger (flat IP and DIP joints)
17*	flexion of thumb
18*	relaxed posture (reference posture)
19	maximum flexion of MCP and PIP with extended DIP
20	opposition of thumb and interdigital space between DIP2 and DIP3
21	opposition of thumb and interdigital space between DIP3 and DIP4
22*	opposition of thumb and interdigital space between DIP4 and DIP5
23*	maximum flexion of PIP and DIP with extended MCP
24	opposition of thumb with index finger near the DIP2 joint
25	opposition of thumb with middle finger near the DIP3 joint
26*	opposition of thumb with ring finger near the DIP4 joint
27	opposition of thumb with little finger near the DIP5 joint
28	opposition of thumb with index finger near the PIP2 joint

Table 3.1: (continued)

number	description
29*	opposition of thumb with middle finger near the PIP3 joint
30	opposition of thumb with ring finger near the PIP4 joint
31	opposition of thumb with little finger near the PIP5 joint
32	opposition of thumb with index finger near the MCP2 joint
33	opposition of thumb with middle finger near the MCP3 joint
34	opposition of thumb with ring finger near the MCP4 joint
35	opposition of thumb with little finger near the MCP5 joint
36*	flexion of MCP joints with extended PIP and DIP joints
37*	extension of MCP joints
38	flexion of MCP1 joint
39	flexion of CMC1 joint
40*	maximum extension of MCP1 joint
41*	ulnar abduction of the MCP joints
42*	radial abduction of the MCP joints
(43)	passive dorsal flexion of the DIP joints)
44*	palmar flexion of ulnar metacarpal bone (MC5) around IMC4–5
45	holding a hammer
(46)	holding a medium-sized cylindrical object while pressing)
(47)	holding a medium-sized cylindrical object without pressing)
(48*)	holding a screw driver)
(49)	holding a pen)
(50)	holding a key)
51*	lateral movement of the MCP1 joint in dorsal-ulnar direction
*	flexion of MCP2–5 while spreading the fingers

Table 3.1: (continued)

number	description
	Notes: Postures in parentheses are not used for identifying the model parameters, because they involve external forces on the fingers. The postures marked with an asterisk (*) are also used with recordings of another subject in Chapter 5 and Chapter 6.

The process of kinematic modelling is essentially a process of dimensionality reduction. For example, consider a pair of bones that are connected by a joint. The relative pose of the distal bone with respect to the proximal bone is generally described by six variables that define its position and orientation in 3D space. If it is possible to find a single rotation axis that appropriately describes the movement of the distal bone with respect to the proximal bone, only a single variable is necessary to describe its relative pose.

To properly understand the process of modelling, it is necessary to see the difference between static and dynamic parameters. In above example, the parameters that describe the position and orientation of the rotation axis, the initial pose of bone and the joint limits are static, which means that they do not change during movement; the rotation angle is dynamic, which means that it changes during movement.

The aim of kinematic modelling is to find a representation of posture that is accurate, as well as generative. *Accurate* means that the modelled posture is close to the real posture. *Generative* means that varying the dynamic parameters within their allowed limits leads to postures that are close to real postures. In the example, the general pose description with six parameters per rigid body can be used to describe any measured pose with 100% accuracy. However, these parameters may be varied in such a way that strange and unnatural poses are generated. On the other hand, when the single-axis model is used, all poses generated by varying the rotation angle within the joint limits are close to natural poses (even though there may be some residual difference). A further aim is that the model is simple. Simplicity is primarily shown by a low number of dynamic parameters; further by a low number of static parameters and by other considerations such as that the model should be easily implementable in a robot.

In this Chapter, different methods for kinematic hand modelling are presented. Each of the modelling assumptions may introduce errors. The size of the errors depends on the quality of the model, that is, how closely the model matches reality.

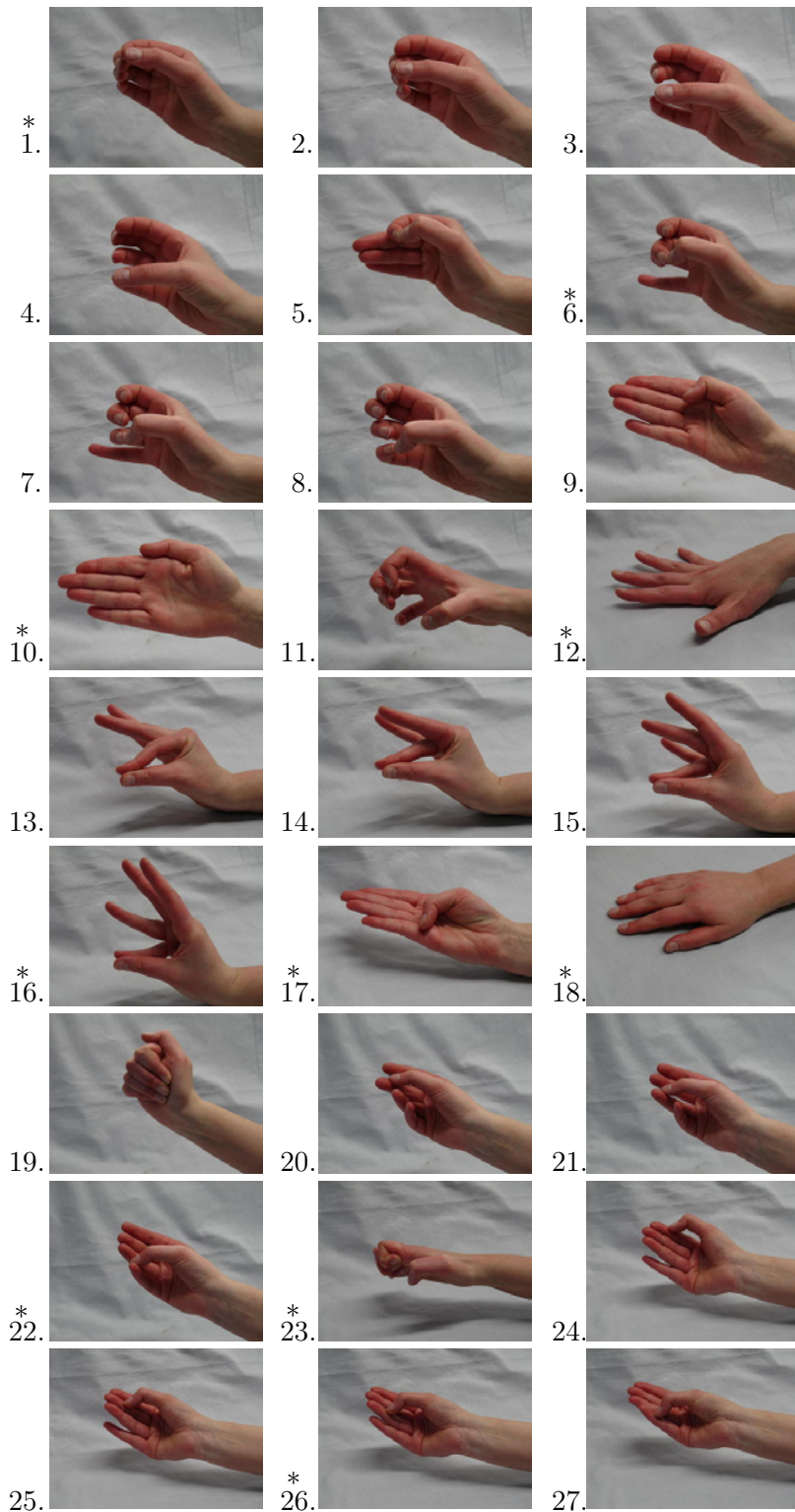


Figure 3.3: The recorded hand postures (see Table 3.1). Postures 1–27. Adapted from Stillfried [2009].

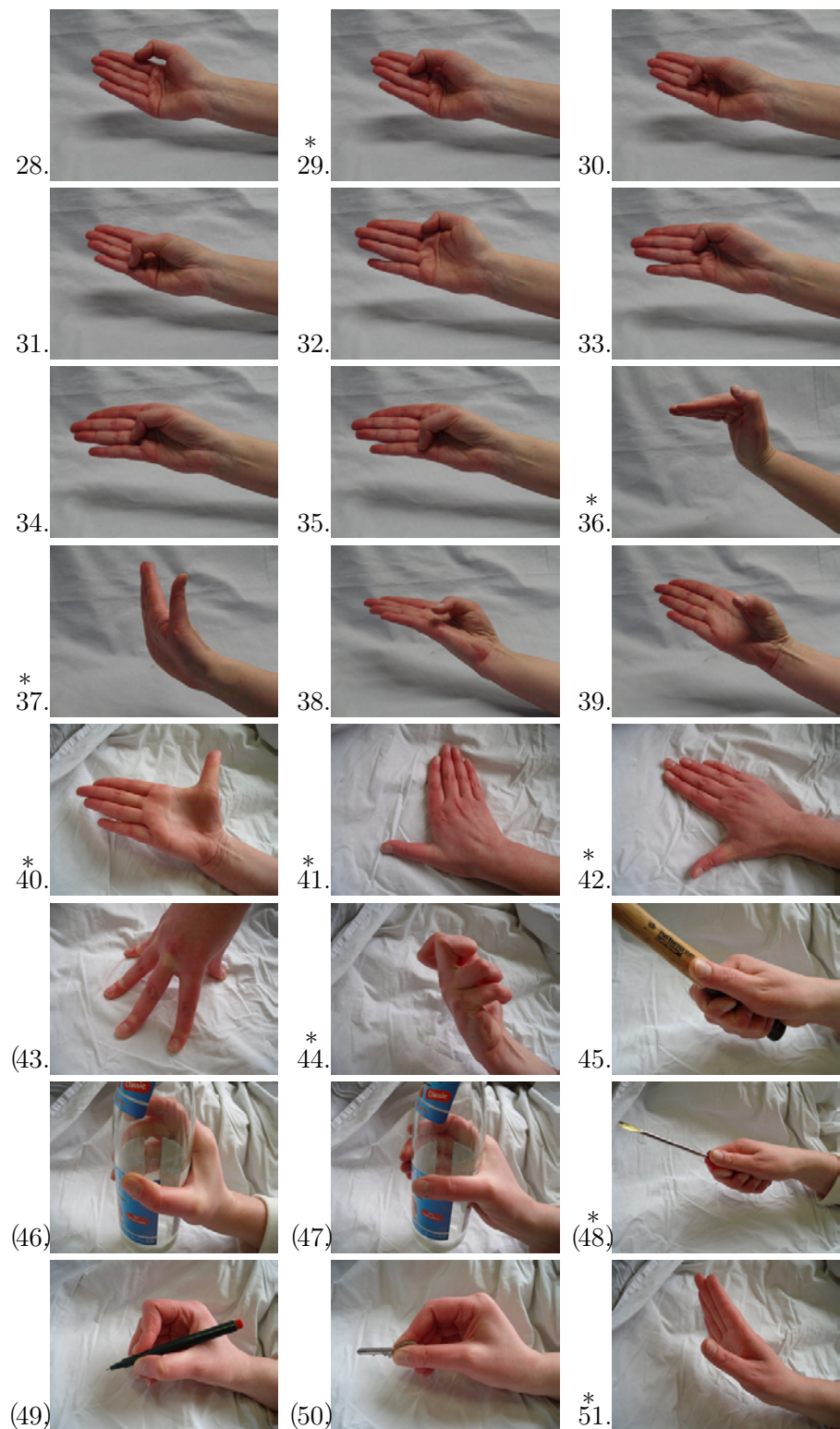


Figure 3.4: The recorded hand postures (see Table 3.1). Postures 28–51. Adapted from Stillfried [2009].

3.1.2 Modelling assumptions

By making some assumptions, the optimisation problem may be simplified, it may work with less samples, it may reflect more concentratedly the functionality and the resulting model may be simpler. The assumptions need to be made carefully, so that no large errors are introduced by false assumptions.

The first two assumptions that shall be made here is that the bones are rigid bodies and that interesting aspects of hand functionality are reflected by the movement of the bones. The first assumption is backed by the measured material properties of the bone. Cortical bone is a quite stiff material with a Young's modulus of 4500–20.000 N/mm², depending on the direction of the force and the apparent density of the cortical bone [Wirtz et al., 2000]. A large force of 200 N on a small bone with 25 mm² cross-sectional area of cortical bone would therefore compress the bone by only 0.04–0.18%. As for the second assumption, the functional role of kinematics for mechanical interaction with the environment is to properly position and orient the contact surfaces, so that appropriate forces can be applied. The position and orientation of the contact surface, that is, the skin, is primarily governed by the position and orientation of the underlying bone.

The rigid bone is described by its pose in space (that is, the transformation from the bone's own coordinate system to an external coordinate system) and the coordinates of its surface with respect to its own coordinate system. The poses in space can be extracted from the MRI images as described in Section 3.1.1.

Thirdly it is assumed here that the joints that connect the bones behave as serial rotation axes whose pose is fixed to the parent segment or parent axis. There can be more than one axis per joint. This assumption is often made, and it is supported by somewhat roughly circular cross sections of the joint surfaces (Figure 3.5). Since the cross sections are not exactly circular, some modelling error is made.

3.1.3 Single joint parameter identification

The advantage of modelling single joints is that it is conceptually and computationally simpler. The disadvantage, compared to modelling whole fingers or hands, is that some information for identifying the parameters of the joints is lost. When modelling a single joint, one segment is generally considered to be stationary and the other segment is considered to be mobile. Whenever it is inconvenient to mechanically fix one segment during measurement, alternatively the full pose of one segment can be measured, and all measurements can be

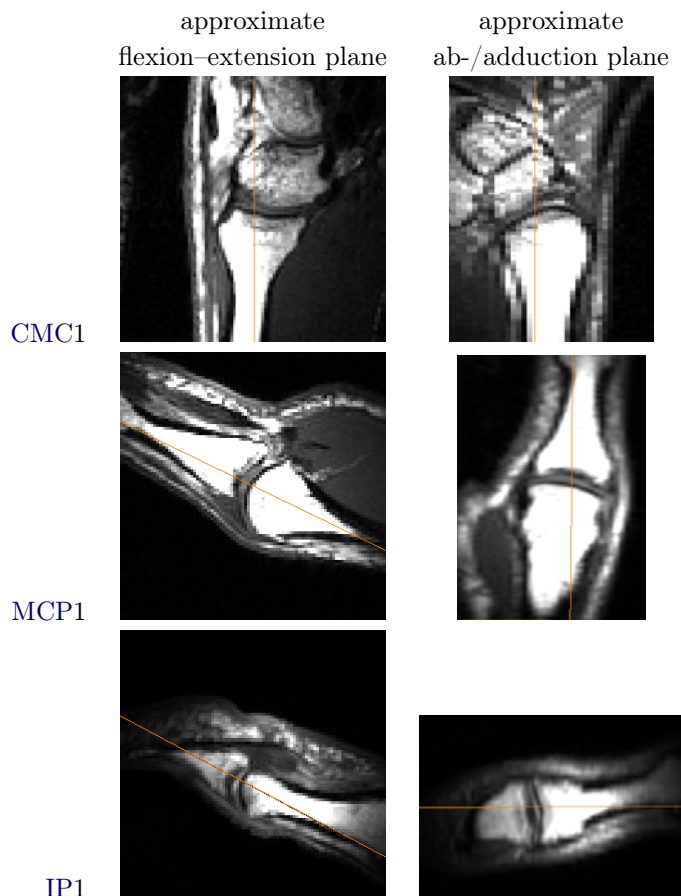


Figure 3.5: MRI images of the three thumb joints in two orthogonal cross sections each. The orange lines show the location of the other cross section of the same joint. The joint surfaces are somewhat roughly circular in the planes in which the joint moves (both planes in CMC1 and MCP1, only flexion-extension in IP1).

transformed into a coordinate system rigidly attached to that segment. Let us, without loss of generality, consider the proximal segment fixed and the distal segment mobile:²

$${}^{\text{prox}}T_{\text{dist}}(t) = \left({}^{\text{lab}}T_{\text{prox}}(t)\right)^{-1} {}^{\text{lab}}T_{\text{dist}}(t),$$

where ${}^{\text{lab}}T_{\text{dist}}(t)$ is the measured pose of the distal segment in the laboratory coordinate system, $({}^{\text{lab}}T_{\text{prox}}(t))^{-1}$ is the inverse of the measured pose of the proximal segment in the laboratory coordinate system, and ${}^{\text{prox}}T_{\text{dist}}(t)$ is the pose of the distal segment in the coordinate system of the proximal segment. Similarly, if only the position ${}^{\text{lab}}\mathbf{p}_{\text{dist}}$ of the distal segment is measured, the position is transformed to the coordinate system of the proximal segment:

$${}^{\text{prox}}\mathbf{p}_{\text{dist}}(t) = \left({}^{\text{lab}}T_{\text{prox}}(t)\right)^{-1} {}^{\text{lab}}\mathbf{p}_{\text{dist}}(t).$$

The general approach to joint model parameter identification is calculating modelled segment poses using a set of static and dynamic parameters (forward kinematics) and iteratively optimising the parameters so that the distances between the modelled segment poses and some measured segment poses are minimised. Note that “distance” can refer to a translational distance as well as a rotational distance. Any joint model can be used in this approach, as long as its forward kinematics can be calculated. This approach was used, for example, by Sommer and Miller [1980] to model a human wrist joint.

The forward kinematics function $f(\boldsymbol{\xi}, \mathbf{q})$ of a single joint generates a modelled pose ${}^{\text{prox}}T_{\text{dist,mod}}$ of the distal bone with respect to the proximal bone, depending on the static parameters $\boldsymbol{\xi}$ and the dynamic parameters \mathbf{q} :

$${}^{\text{prox}}T_{\text{dist,mod}} = f(\boldsymbol{\xi}, \mathbf{q}).$$

The static and dynamic parameters are optimised to minimise the distance between measured and modelled markers. The cost function ϵ is a weighted combination of rotational and Euclidean distance:

$$\{\boldsymbol{\xi}_{\text{opt}}, \mathbf{q}_{\text{opt}}(t)\} = \arg \min_{\boldsymbol{\xi}, \mathbf{q}} (\epsilon), \quad (3.7)$$

²The left superscript before a vector denotes the coordinate system in which the coordinates of the vector are given, for example, the coordinates of ${}^A\mathbf{v}$ are given in coordinate system A. The notation ${}^A T_B$ denotes a transformation from coordinate system B to coordinate system A, such that ${}^A \mathbf{v} = {}^A T_B {}^B \mathbf{v}$.

with

$$\epsilon = \underset{t \in \mathcal{P}}{\text{mean}} \left[w_t \left\| {}^{\text{prox}}T_{\text{dist}}(t)_{(1:3,4)} - f(\xi, \mathbf{q}(t))_{(1:3,4)} \right\| + w_r \text{RotationalDistance}\left({}^{\text{prox}}T_{\text{dist}}(t)_{(1:3,1:3)}, f(\xi, \mathbf{q}(t))_{(1:3,1:3)}\right) \right], \quad (3.8)$$

where t is a time instant and \mathcal{P} is the set of time instants in which postures are measured. Since the Euclidean and rotational distances have different units, the weighting factors w_t and w_r are used to explicitly set the weights of both types of distances. The sub-vector $T_{(1:3,4)}$ of a transformation matrix T describes its translational part and the sub-matrix $T_{(1:3,1:3)}$ describes the rotational part (for the sub-matrix notation see Section [Mathematical notation](#) near the beginning of the document).

Note that a simple mean of errors is used. While minimising the mean of squared errors would give an optimal estimate in the case of normal distributions, it is sensitive to outliers in case that the distribution is not exactly normal. The simple mean of errors is used because it is more robust in this regard.

The optimisation was split into two parts—first the optimisation of the axis orientations with the weight w_t of the translational error set to zero and subsequently the optimisation of the axis positions with the weight w_r of the rotational error set to zero.

The choice of the model $f(\xi, \mathbf{q})$ is not a trivial task. Often a single model is used based on the experience of the experimenters. In [[Sommer 3rd and Miller, 1980](#)], the wrist is modelled by two serial, non-intersecting, non-orthogonal axes of rotation.

In this optimisation problem, the dynamic parameters need to be optimised, even though only the static parameters may be of interest. For the special cases of a spherical joint (rotations around a single point) and a hinge joint (rotations around a single axis) there are methods to find the optimal [CoR](#) and optimal axis of rotation that do not require the optimisation of dynamic parameters [[Chang and Pollard, 2007a,b](#)].

Details on the parameter identification of single joint models

The joint parameters (positions and orientations of the rotation axes) are identified on a joint-by-joint basis by numerically minimising the discrepancy between the measured and modelled relative motion of the joint's distal bone with respect to the proximal bone. To calculate the relative motion, the absolute motion of

the proximal bone is inversely applied to the absolute motion of the distal bone:

$$R_r = \bar{R}_p^{-1} \bar{R}_d \quad (3.9)$$

and

$$\mathbf{t}_r = \bar{R}_p^{-1} (\mathbf{c}_d + \bar{\mathbf{t}}_d - \bar{\mathbf{t}}_p - \mathbf{c}_p) + \mathbf{c}_p - \mathbf{c}_d, \quad (3.10)$$

where $\{R_r, \mathbf{t}_r\}$ is the relative motion of the distal bone with respect to the proximal bone, $\{\bar{R}_p, \bar{\mathbf{t}}_p\}$ and $\{\bar{R}_d, \bar{\mathbf{t}}_d\}$ are the absolute motions of the proximal and distal bone that result from the bone localisation (Section 3.1.1), and \mathbf{c}_p and \mathbf{c}_d are the vectors of Cartesian coordinates of the centroids of the proximal and distal bone.

In order to reduce the dimensionality of the search space, the identification of the axis orientations and positions is split up into two steps. In the first step, the axis orientations are identified by minimising the rotational distance between the measured orientations and the modelled orientations.

The modelled orientation R_m of the bone is calculated as follows:

$$R_m = \prod_{k=1}^{n_a} \text{Rot}(\mathbf{a}_k, q_k) \quad (3.11)$$

where $n_a \in \{1, 2, 3\}$ is the number of rotation axes of the joint, \mathbf{a}_k is the orientation of the k^{th} axis and q_k is the rotation angle around the k^{th} axis, and $\text{Rot}(\cdot, \cdot)$ is the rotation matrix (Equation (1)). The position and orientation vectors of the rotation axes are given in the coordinate system of the MRI system, and with respect to the bones in the reference posture.

The orientations of the rotation axes and the rotation angles are identified by numerically minimising the weighted mean square angular difference over all postures:

$$\begin{aligned} &(\mathbf{a}_1, \dots, \mathbf{a}_{n_a}, \mathbf{q}_1, \dots, \mathbf{q}_{n_p}) = \\ &\arg \min_{(\mathbf{a}'_1, \dots, \mathbf{a}'_{n_a}, \mathbf{q}'_1, \dots, \mathbf{q}'_{n_p})} \left[\sum_{j=1}^{n_p} w_{rj} \text{RotationalDistance} (R_{rj}, R_{mj}(\mathbf{a}'_1, \dots, \mathbf{a}'_{n_a}, \mathbf{q}'_j))^2 \right], \end{aligned} \quad (3.12)$$

with

$$w_{rj} = \frac{1}{\sigma_{rpj}^2 + \sigma_{rdj}^2} \quad (3.13)$$

where n_p is the number of postures, $\mathbf{a}_1, \dots, \mathbf{a}_{n_a}$ are the orientation vectors of the rotation axes, $\mathbf{q}_1, \dots, \mathbf{q}_{n_p}$ are the vectors of joint angles for each posture

$j \in \{1, \dots, n_p\}$, where $\mathbf{q}_j = (q_{1j}, \dots, q_{n_a j})^T$ contains the joint angles for each rotation axis, w_{rj} is the confidence weight due to the variances σ_{rpj}^2 and σ_{rdj}^2 of the rotation estimates of the proximal and distal bone in posture j resulting from the bone localisation (Section 3.1.1), RotationalDistance gives the angle of the smallest rotation that needs to be added to one of the rotations to make it equal to the other rotation, R_{rj} is the measured relative orientation of the bone in posture j according to Equation (3.9) and R_{mj} is the modelled relative orientation of the bone according to Equation (3.11).

The positions of the rotation axes are identified by minimising the mean squared distance between the measured and modelled position of the bone centroid:

$$(\mathbf{p}_1, \dots, \mathbf{p}_{n_a}) = \arg \min_{(\mathbf{p}'_1, \dots, \mathbf{p}'_{n_a})} \left[\sum_{j=1}^{n_p} w_{tj} \|\mathbf{t}_{mj}(\mathbf{p}'_1, \dots, \mathbf{p}'_{n_a}) - \mathbf{t}_{rj}\|^2 \right], \quad (3.14)$$

with

$$\mathbf{t}_{mj}(\mathbf{p}'_1) = \left(\prod_{k=1}^{n_a} \text{Rot}(\mathbf{a}_k, q_{kj}) \right) (\mathbf{c}_d - \mathbf{p}'_1) + \mathbf{p}'_1 - \mathbf{c}_d$$

for joints with intersecting axes,

$$\begin{aligned} \mathbf{t}_{mj}(\mathbf{p}'_1, \dots, \mathbf{p}'_{n_a}) = \\ \left(\prod_{k=1}^{n_a} \text{Rot}(\mathbf{a}_k, q_{kj}) \right) \mathbf{c}_d + \left(\sum_{k=1}^{n_a} \left(\prod_{l=1}^{k-1} \text{Rot}(\mathbf{a}_l, q_{lj}) - \prod_{l=1}^k \text{Rot}(\mathbf{a}_l, q_{lj}) \right) \mathbf{p}'_k \right) - \mathbf{c}_d \end{aligned}$$

for joints with non-intersecting axes and

$$w_{tj} = \frac{1}{\sigma_{tpj}^2 + \sigma_{tdj}^2}, \quad (3.15)$$

where $\mathbf{p}_1, \dots, \mathbf{p}_{n_a}$ are the position vectors of the rotation axes, \mathbf{t}_{mj} are the modelled translations of the bone centroid, \mathbf{t}_{rj} are the measured translations of the bone centroid, \mathbf{a}_k and q_{kj} are the rotation axes and angles as derived from Equation (3.12) and \mathbf{c}_d is the position vector of the distal bone centroid.

In order to perform the optimisations described in Equations (3.12) and (3.14), the `fminsearch` function of the Matlab computation software is used, which implements the Nelder-Mead simplex algorithm [1965]. The algorithm is called with broadly different starting points to increase the chance of finding the global optimum, and not only a local optimum. For Equation (3.12), a nested optimisation is conducted, with an outer optimisation for the axis orientations $\mathbf{a}_1, \dots, \mathbf{a}_{n_a}$. Within each iteration step of the outer optimisation, a number of n_p

inner optimisations are carried out to find the optimum joint angles $\mathbf{q}_1, \dots, \mathbf{q}_{n_p}$. For the outer optimisation, the axis orientations are parametrised by two spherical coordinates (azimuth and elevation), in order to reduce the search space by one dimension as compared to Cartesian coordinates for axis orientation.

Cross-validation of the modelling error

In order to check to what extent the results apply to the investigated hand in general as opposed to being overfit to the investigated postures, a leave-one-out cross-validation (LOOCV) is performed. For this, the parameters of the joints are identified n_p times, with n_p being the number of measured bone poses, where in each round one of the poses is left out. The joint parameters (axis orientations and positions) resulting from each identification are used to move the bone as close as possible to the omitted pose. The rotational and translational discrepancy between the modelled and measured bone pose is calculated, and the weighted mean of rotational and translational discrepancies between the modelled and measured bone poses is calculated.

3.1.4 Definition and selection of joint types

Joints with one, two, or three axes of rotation are considered. Two constraints are selectively applied: that the axes intersect, and/or that the axes are perpendicular to each other. Figure 3.6 shows the joint types. For one-axis joints the constraints (perpendicular and/or intersecting) do not make sense, so there is one joint type 1a. For the two-axis joints, all combinations of constraints are used, leading to four joint types 2oia, 2ia, 2ona and 2na.

In three-axis joints with intersecting axes, an optimisation of axis orientations does not make sense, since any orientation of the distal bone can be achieved with any combination of joint axes where the second axis is perpendicular to both the first and third axis. So in the joint types 3oia and 3ona, the axis orientations are predefined and only the axis positions are optimised.³ The joint type 2cia is a special type of a two-axis joint with one DoF, where the second axis is located along the distal bone and its rotation angle is coupled to the rotation angle of the first axis.

The joint types are selected according to the following criteria: accuracy, simplicity and generativeness.

³In fact, the orientation of the joint axes *does* influence the position of the distal bone if the axes are *non-intersecting*. So in future work, a third three-axis joint type “3na” with free, non-intersecting axes should be added for completeness.

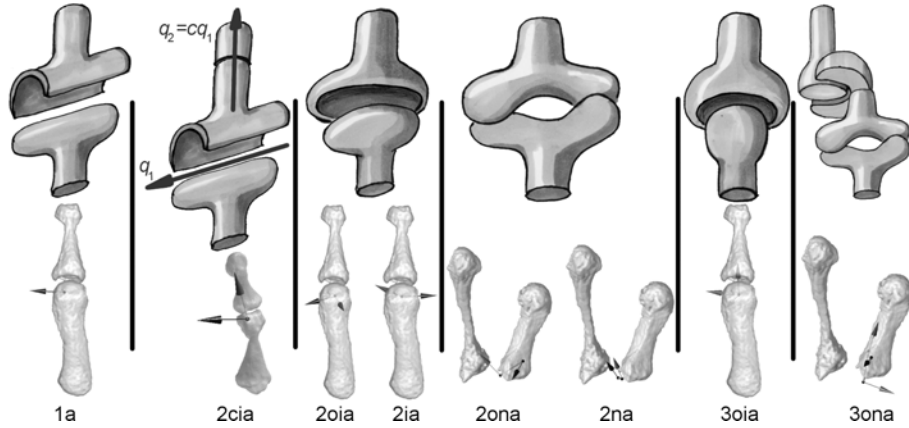


Figure 3.6: Joint types used in the presented method. From left to right: Hinge joint (one axis, 1a), hinge joint with combined longitudinal rotation (two coupled intersecting axes, 2cia), condyloid joint (two orthogonal/oblique intersecting axes, 2oia/2ia), saddle joint (two orthogonal/oblique non-intersecting axes, 2zona/2na), ball joint (three orthogonal intersecting axes, 3oia) and 3-Dof joint with orthogonal non-intersecting axes (3ona, combination of a saddle and a pivot joint). Reproduced from [Stillfried et al., 2014], with drawings from http://en.wikipedia.org/wiki/Hinge_joint.

Table 3.2: Complexity of the joint types in terms of dynamic and static parameters.

joint type	no. of dynamic parameters	minimal no. of static parameters
1a	1	4
2cia	1	5
2oia	2	6
2zona	2	7
2ia	2	7
2na	2	8
3oia	3	3
3ona	3	6

Accuracy can simply be calculated as the differences between the measured poses and closest-possible modelled poses, which corresponds to the cost function in Equation (3.7), where a lower mean weighted residual error ϵ means higher accuracy.

An approximate ranking of complexity is achieved by sorting the joint types primarily according to the number of dynamic parameters (number of **DoF**) that are needed to describe their movements. The **DoF** correspond to the minimum number of actuators that are required to move the joint, and generally, a device with more actuators is more complex than a device with less actuators. Joints with the same number of **DoF** are ranked by the number of static parameters. The static parameters define the concrete design of the joint. Less static parameters mean firstly that less design decisions need to be taken. Secondly, constraining the axis orientations to orthogonal, which reduced the number of static parameters, leads to a joint type which is some cases easier to implement technically than a joint with arbitrary axis orientations. Table 3.2 shows the measures of complexity of the joint types in terms of dynamic and static parameters.

It is difficult to decide whether a joint model is generative, that is, whether it only produces realistic postures. One method to judge this question is to generate movements and intuitively decide whether they look realistic. Furthermore, the generativeness is closely related to the complexity of the joint type: a joint with more dynamic parameters provides more possibilities for unnatural poses. There is typically a trade-off between the accuracy of a joint on the one hand and simplicity and generativeness on the other hand. The trade-off is visualised in a trade-off curve, which connects those points in which improving one criterion necessarily leads to worsening of another criterion. An example of a trade-off curve is shown in Figure 3.7.

3.2 Results

The following paragraphs describe results regarding the selection of joint types and the amount of modelling error.

3.2.1 Repeatability of the bone registration with different sampling of points

The repeatability of the motion estimations is examined by repeating it 100 times with randomly permuted point sets (Section 3.1.1). In cases with very different clusters of pose estimates, the correct clusters were selected manually.

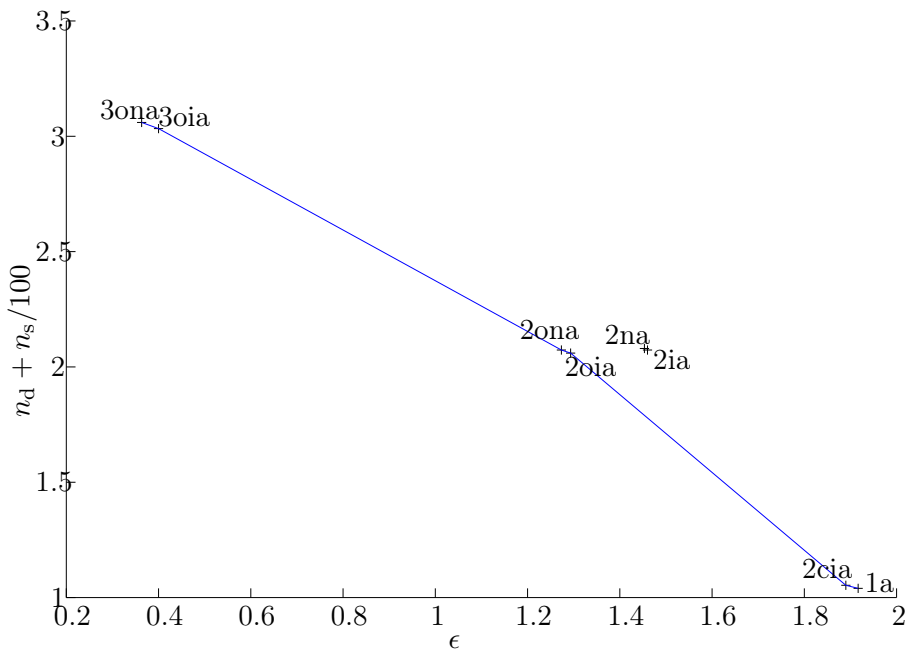


Figure 3.7: Trade-off curve of different joint types for the PIP3 joint. In the abscissa, the accuracy is plotted in terms of ϵ (Equation (3.8)) with $w_t = 0.5 \text{ mm}^{-1}$ and $w_r = 0.5 \text{ degrees}^{-1}$. In the ordinate, the complexity is plotted in terms of primarily dynamic parameters n_d and secondarily static parameters n_s . On both axes, lower values are better. The joint types 2ia and 2na are in the so-called inefficient region: their accuracy criterion can be improved without worsening their complexity criterion.

Table 3.3: Standard deviation over the correct repetitions (up to 100) of the motion estimation for the rotational (σ_r) and translational (σ_t) part. The minimum, maximum and mean over all n usable images are given. Those images where none of the repetitions were correct were not usable.

bone	σ_r (°)			σ_t (mm)			n
	min	max	mean	min	max	mean	
MC1	1.0	5.3	2.9	0.1	0.2	0.1	48
PP1	1.6	5.7	3.2	0.1	0.3	0.1	47
PD1	1.2	5.4	2.2	0.1	0.3	0.1	43
MC2	1.7	8.0	3.4	0.1	0.4	0.2	50
PP2	1.0	4.5	2.8	0.1	0.1	0.1	42
PM2	1.2	3.7	2.2	0.0	0.1	0.1	39
PD2	2.1	7.6	3.9	0.0	0.5	0.1	33
MC3	1.1	4.9	2.6	0.1	0.3	0.2	44
PP3	1.3	5.8	3.2	0.1	0.1	0.1	42
PM3	1.0	2.9	1.7	0.0	0.1	0.1	39
PD3	1.9	5.9	2.9	0.1	0.7	0.1	37
MC4	1.4	7.6	3.5	0.1	0.2	0.1	44
PP4	0.9	8.9	3.4	0.1	0.2	0.1	42
PM4	1.2	3.5	2.4	0.0	0.2	0.1	38
PD4	1.2	4.3	2.6	0.0	0.2	0.1	36
MC5	1.4	11.2	4.1	0.1	0.4	0.1	44
PP5	1.5	7.1	3.7	0.0	0.1	0.1	43
PM5	1.0	4.3	2.8	0.0	0.1	0.1	39
PD5	1.7	9.7	3.4	0.0	0.1	0.0	35
all	0.9	11.2	3.0	0.0	0.7	0.1	39.2

The standard deviation of the rotation and translation estimate is given in Table 3.3 as the square root of the variance described in Equations (3.5) and (3.6).

The rotational standard deviation σ_r ranges from 0.9° to 11.2° , with a mean of 3.0° , and the translational standard deviation σ_t ranges from less than 0.05 mm to 0.5 mm, with a mean of 0.1 mm, depending on the bone and the posture. The values for all bones are given in Table 3.3.

3.2.2 Joint types

The main results of the presented method are movement models of the analysed human hand. The joint types of the movement model represent a compromise between accuracy, simplicity and generativeness. In Figure 3.7, the trade-off curve of different joint types is shown at the example of the PIP3 joint. In

the abscissa, the accuracy is plotted in terms of ϵ (Equation (3.8)) with $w_t = 0.5 \text{ mm}^{-1}$ and $w_r = 0.5 \text{ degrees}^{-1}$. In the ordinate, the complexity is plotted in terms of primarily dynamic parameters and secondarily static parameters.

In the example, the non-orthogonal joint types 2ia and 2na are not on the trade-off curve, because the criterion of accuracy can be improved without worsening the criterion of complexity by moving to 2oia or 2ona.

Depending on the desired accuracy in terms of discrepancy between modelled and measured bone poses, hand models with different complexity are generated. In Figure 3.8, different hand models from simple and less accurate (*top*) to complex and more accurate (*bottom*) are presented.

In the simple model, four joints are modelled as 2-DoF universal joints: thumb, index, ring and little finger MCP. The other joints are modelled as 1-DoF hinge joints.

The intermediately complex hand model (*middle*) differs from the simple one by providing two DoF each to MCP3 and CMC1. The joint axes of MCP3 intersect, while the ones of CMC1 do not.

The most complex model (*bottom*) models CMC1 with three non-intersecting axes, with the third one allowing a longitudinal rotation (pro-/supination) of MC1. A longitudinal rotation is also enabled in DIP2 and PIP5, while PIP2 allows a combined longitudinal rotation and sideways movement. The little finger DIP joint allows a longitudinal rotation only in an extended position. Additional DoF for sideways movement are found in DIP2, DIP3, DIP4 and IP1.

The weighted-mean rotational deviation per joint ranges from 1.6° in IMC3 to 5.5° in IP1. The maximum rotational deviation in a single hand posture is 17.2° in CMC1. Weighted-mean translational deviation ranges from 0.9 mm (PIP4) to 2.6 mm (CMC1), and the maximum translational deviation in a single hand posture is 7.2 mm, and also occurs in CMC1.

Table 3.4 shows the residual error of different joint types, as well as their range of motion and joint axis inclinations. The examples in Figure 3.9 are supposed to give the reader a feeling of these values.

3.2.3 Cross-validation

For most joints, there is only a slight increase of the rotational and translational modelling error from the whole data mean error to the LOOCV mean error. For example, in the thumb MCP joint, the mean rotational error when using all poses is 2.5° , and the mean rotational error of the LOOCV is 2.9° . In the same joint, the mean translational error is 1.2 mm when taking into account all poses and

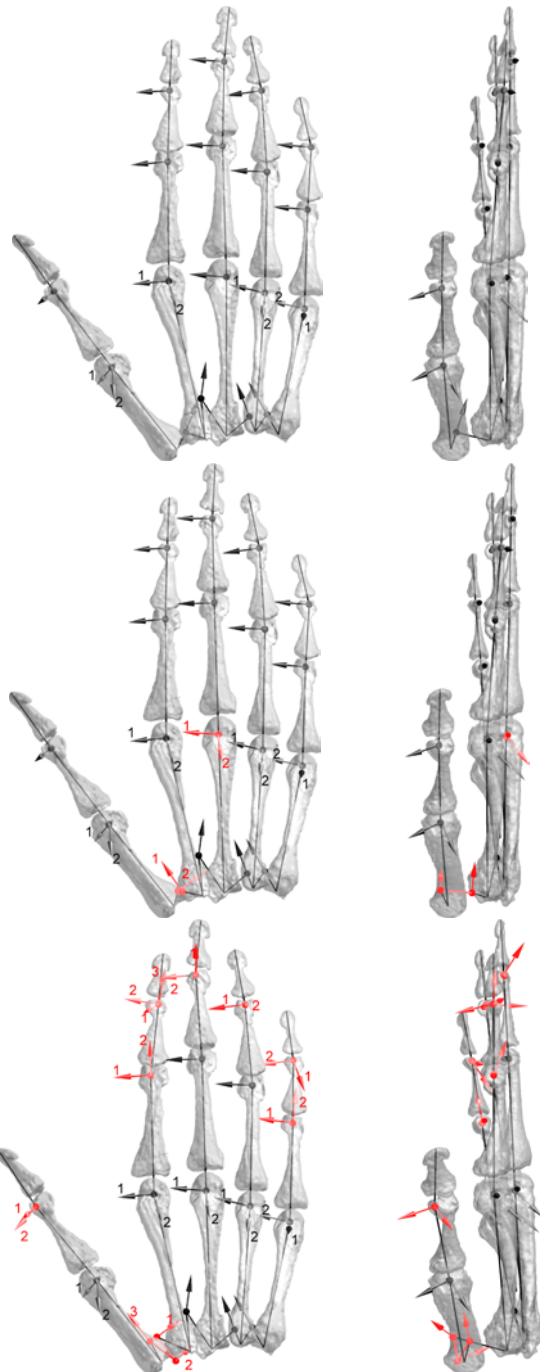


Figure 3.8: Variants of the kinematic model at different accuracy constraints, dorsal view (left) and radial view (right). In the colour version, the changes with respect to the next simpler variant are marked in red.

Top: 22 DoF, rotational deviation $< 9^\circ$, translational deviation $< 6\text{ mm}$. *Middle:* 24 DoF, rotational deviation $< 6^\circ$, translational deviation $< 3\text{ mm}$. (This is the hand model that shows the Chapter numbers.) *Bottom:* 33 DoF, rotational deviation $< 3^\circ$, translational deviation $< 2\text{ mm}$. In joints with more than one axis, the first one is marked “1”, the second one “2”, and, if existing, the third one “3”. Adapted from Stillfried et al. [2014].

1.3 mm in the LOOCV analysis. This means that the results are generally valid for the investigated individual hand and do not depend on certain postures.

All differences for the translational error are within 0.2 mm and all differences for the rotational error are within 1.0° except for the thumb interphalangeal joint, where the difference is 1.2° and the little finger metacarpophalangeal joint, where it is 3.0°. In these exceptional cases the joint parameters depend strongly on the selection of the subset of bone poses. This means that there are single extreme poses in the data that are not adequately represented by the other poses. The results are given in detail in Table 3.4.

Table 3.4: Properties of the 22-, 24- and 33-DoF models (Figure 3.8): joint name, joint type, weighted mean rotational (d_r) and translational error (d_t) on the whole data (all) and from the LOOCV, RoM, and inclination of the rotation axis in 1-DoF interphalangeal joints. Inclination is the angle between the rotation axis and the plane perpendicular to the longitudinal axis of the proximal bone. For the joint type abbreviations see Figure 3.6.

joint name	joint type	mean(d_r)		mean(d_t)		axis no.	RoM	inclination
		all	LOOCV	all	LOOCV			
CMC1	1a	7.8°	8.1°	4.9 mm	4.9 mm	1	75.1°	
CMC1	2ona	2.9°	3.2°	2.1 mm	2.2 mm	1	60.1°	
						2	64.4°	
CMC1	3ona	0.0°	0.0°	1.3 mm	1.3 mm	1	46.9°	
						2	59.0°	
						3	58.1°	
MCP1	2oia	2.5°	2.9°	1.2 mm	1.3 mm	1	92.5°	
						2	52.0°	
IP1	1a	4.8°	5.0°	1.0 mm	1.0 mm	1	103.1°	2.0° proximal
IP1	2oia	2.1°	3.3°	0.9 mm	0.9 mm	1	103.0°	
						2	18.2°	
MCP2	2oia	2.8°	3.2°	1.2 mm	1.3 mm	1	110.3°	
						2	43.3°	
PIP2	1a	3.9°	4.0°	0.8 mm	0.8 mm	1	121.1°	7.3° proximal
						2	24.3°	
DIP2	1a	4.5°	4.7°	0.9 mm	0.9 mm	1	101.0°	4.4° proximal
						2	16.9°	
DIP2	3oia	0.0°	0.0°	0.8 mm	0.8 mm	2	100.7°	
						3	31.2°	
IMC3	1a	1.6°	1.6°	0.9 mm	0.9 mm	1	11.5°	
MCP3	1a	7.5°	7.8°	3.0 mm	3.2 mm	1	119.7°	

Table 3.4: (continued)

joint name	joint type	mean(d_r)		mean(d_t)		axis no.	RoM	inclination
		all	LOOCV	all	LOOCV			
MCP3	2oia	1.6°	2.1°	1.0 mm	1.2 mm	1	119.0°	
						2	41.1°	
PIP3	1a	2.9°	3.0°	0.9 mm	0.9 mm	1	122.8°	2.7° distal
DIP3	1a	4.7°	4.9°	1.1 mm	1.1 mm	1	110.4°	2.5° proximal
DIP3	2oia	2.7°	3.5°	1.0 mm	1.1 mm	1	23.4°	
						2	109.8°	
IMC4	1a	1.6°	1.6°	0.8 mm	0.8 mm	1	15.2°	
MCP4	2oia	2.8°	3.2°	1.5 mm	1.6 mm	1	127.5°	
						2	38.5°	
PIP4	1a	2.5°	2.7°	0.7 mm	0.7 mm	1	123.7°	8.1° distal
DIP4	1a	3.6°	3.7°	0.6 mm	0.6 mm	1	93.2°	1.9° distal
DIP4	2oia	2.6°	3.0°	0.5 mm	0.6 mm	1	93.3°	
						2	8.3°	
IMC5	1a	2.2°	2.3°	0.9 mm	1.0 mm	1	22.0°	
MCP5	2oia	2.8°	5.8°	1.5 mm	1.7 mm	1	46.9°	
						2	147.1°	
PIP5	1a	4.7°	4.9°	0.8 mm	0.8 mm	1	118.9°	2.9° distal
PIP5	2oia	1.3°	2.3°	0.8 mm	0.8 mm	1	118.9°	
						2	17.5°	
DIP5	1a	5.6°	5.9°	0.8 mm	0.8 mm	1	92.1°	13.3° distal
DIP5	2oia	2.5°	2.9°	0.7 mm	0.7 mm	1	39.1°	
						2	90.1°	

3.3 Discussion

A work flow for creating a kinematic hand model from [MRI](#) measurements was presented. It includes the selection and recording of hand postures, the segmentation of the [3D](#) volumes of the bones, the creation and registration of bone point clouds, a manual selection in the case of ambiguous registration, an optimisation of the static and dynamic joint parameters and the selection of the appropriate joint types.

While 45 hand postures were used for the identification of the axis parameters, some of them were rather similar. For example many of the oppositions of the

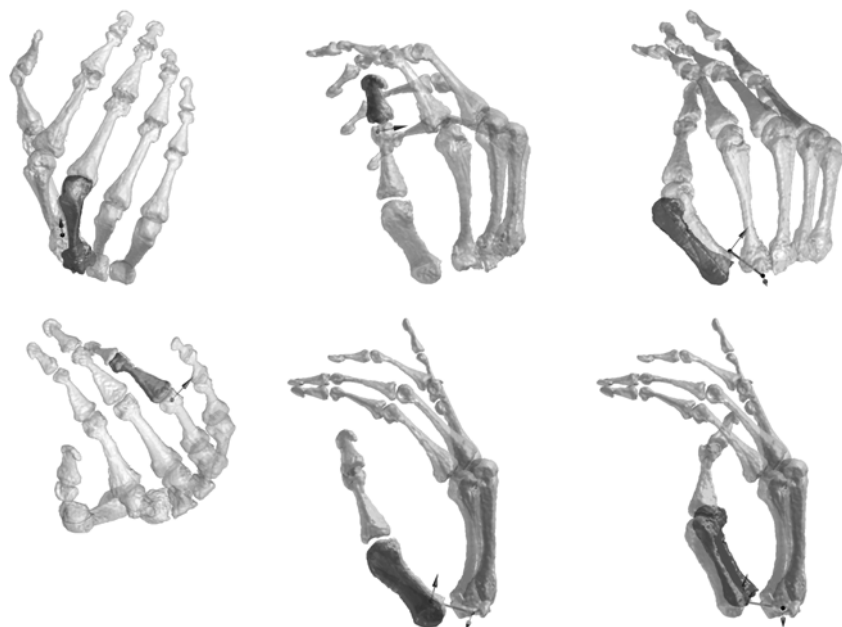


Figure 3.9: Comparison of measured (bright) and modelled (dark) bone poses in several postures. Top left: Pose of the bone **MC4** relative to **MC3** in posture 36. The rotational discrepancy is 1.6° and the translational discrepancy is 1.0 mm. The arrow is the rotation axis of the modelled **IMC4** joint that connects **MC3** and **MC4**. Top middle: **PD1** relative to **PP1** in posture 1. Discrepancy: 5.5° , 1.4 mm. **IP1** joint. Top right: **MC1** relative to **MC2** in posture 29. Discrepancy: 17.2° , 6.4 mm. **CMC1** joint. Bottom left: **MC4** relative to **PP4**. Discrepancy: 2.6° , 0.9 mm. **PIP4** joint. Bottom middle: **MC1** relative to **MC2** in posture 24. Discrepancy: 5.5° , 2.6 mm. Bottom right: **MC1** relative to **MC2** in posture 35. Discrepancy: 5.1° , 7.2 mm.

thumb with the fingers in the Kapandji test involve only small movements in the thumb and very similar finger postures. Some of them might be omitted in future recordings in order to save costs and effort.

Especially the segmentation of the MRI images is labour-intensive, with a well-trained operator taking one to three hours to segment all the bones of one image. Possibly some of the segmentation can be automated (see for example Rusu [2012]), but MRI poses the difficulty that the grey value is not absolutely correlated to the tissue type, but rather that the contrast to the surrounding tissue needs to be considered.

The selection of the joint types depending on the limit on the mean discrepancy between measured and modelled bone poses showed interesting results. For example, with a limit of 9° and 6 mm, both the thumb CMC joint and the middle finger MCP joint could be modelled with only one DoF.

It seems that the second DoF in the metacarpophalangeal (MCP) joint of the thumb is more important than the second DoF in the carpometacarpal (CMC) joint. This is in contrast to many robotic hands, which implement two DoF at the base joint and only one DoF at the other joints of the thumb.

It also seems that the abduction/adduction DoF of the middle finger is not as important as those of the index, ring and little finger. Interestingly, the software that is shipped with the CyberGlove data glove also models the middle finger without an abduction/adduction DoF.

Cerveri et al. [2008] did a similar comparison for the CMC1 joint based on MoCap data. Their RMSE translational discrepancy of the marker positions over 10 subjects and a large set of postures were 2.0 mm for using the 2na joint type and 3.7 mm using the 3oia joint type during a circumduction movement.

These results may provide possibilities to improve the dexterity or save an actuator in a robotic hand. However, the results also depend on the recorded postures. While care was taken to include the whole range of motion of each joint in the set of postures, DoF that are excited more automatically obtain a higher weighting in the calculation of the mean discrepancy. This dependency of the result on the selected postures should be kept in mind when designing a robotic hand for a special purpose. All of the important postures that the robotic hand is supposed to support should be represented in the recorded postures. A possible enhancement of the joint type selection would be to introduce different weights for selected postures in order to reflect their importance for the tasks that the robotic hand should fulfill.

Other enhancements of the method might include a test of leaving out some joints entirely (for example, the palm joints), and calculating the discrepancies

between whole finger or hand postures instead of single joints. However, due to the combinatorics, the lists of joint types per joint should be limited, in order to avoid excessive computation times.

There are six sources for errors in the kinematic modelling process based on [MRI](#):

1. selection of postures,
2. [MRI](#) acquisition,
3. segmentation,
4. motion estimation,
5. joint definition, and
6. joint parameter identification.

It is impossible to consider all possible postures of each joint as they are infinite. Ideal, therefore, would be a very dense sampling of postures during a large number of different movements. This is not possible in [MRI](#) due to cost and time constraints. Hand postures for this work are selected so that for each joint, the extremes and some intermediate positions are covered. The selection of postures influences the resulting model in the way that multiple recordings of similar joint postures assign them a greater weight compared to postures that occur only once. A possible overfit to the selected postures is detected by cross-validation of the results, for example, by [LOOCV](#). The combined error of steps 2 to 6 is represented by the mean rotational and translational deviation between modelled and measured poses in Table 3.4, columns 3–6. The modelling error introduced by the choice of postures (step 1) is reflected by the difference between the overall error (columns 3 and 5) and the [LOOCV](#) error (columns 4 and 6).

In [MRI](#) acquisition, same tissue can be represented by different grey values. Artefacts such as missing parts, motion artefacts, artefacts due to the surrounding tissue and possibly distortions can occur. A discretisation error occurs due to the spacial resolution of (0.76 mm)³.

In the segmentation process, the segmented shape depends on the way the operator defines the grey value thresholds and manually refines the selection. The combined error of [MRI](#) acquisition and segmentation is illustrated by the distributions of grey value and segmented volume (Figures 3.10 and 3.11).

An attempt was made at measuring the error of the [MRI](#) image acquisition by taking images of an animal bone without surrounding tissue, in order to discard

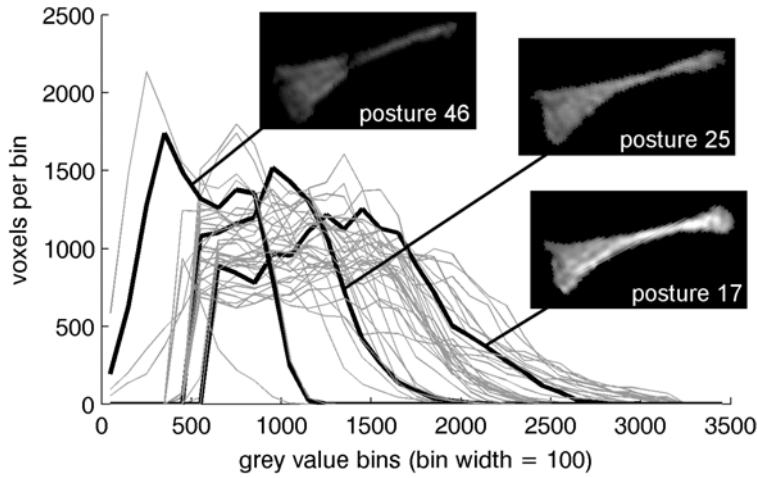


Figure 3.10: Histograms of the grey value distributions of middle finger medial phalanx in different segmented MRI images. Three clearly different examples are highlighted. Of these the central sagittal slice of the MRI image is shown. Reproduced from Stillfried et al. [2014].

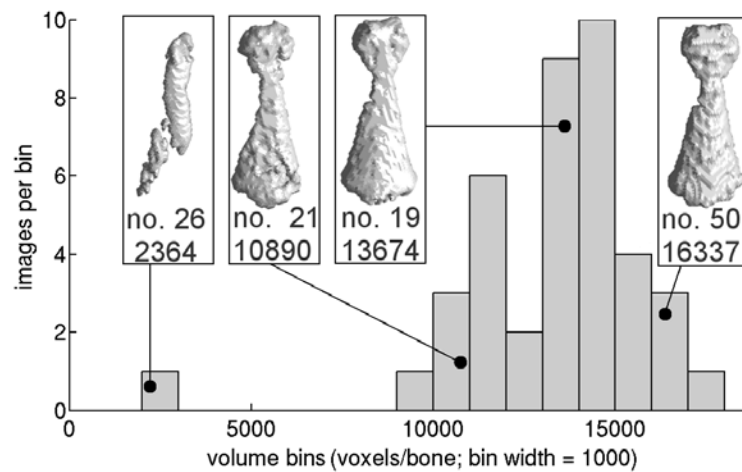


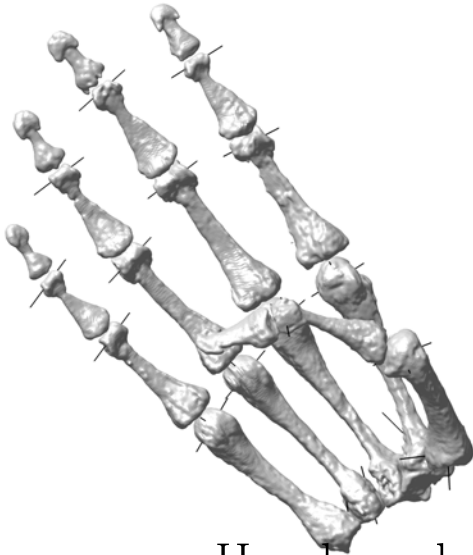
Figure 3.11: Histogram of the segmented volumes of the middle finger medial phalanx in different MRI images. Surface renderings of four examples are shown, with the image numbers and volumes in number of voxels. Reproduced from Stillfried et al. [2014].

the need for segmentation. However, the images showed hardly any signal, which might be due to the missing surrounding tissue or to a lack of humidity within the bone.

The motion estimation error depends on the quality of the segmented point clouds and the robustness of the algorithm with respect to differences in shape and grey value distribution. The combined error of steps 2 to 4 is partly expressed by the repeatability values in Table 3.3, which however do not reflect a potential bias.

In this work, joints are modelled as rotational joints with constant parameters. In the case of a 1-DoF joint, this corresponds to rigid joint surfaces with perfectly circular cross-sections orthogonal to the joint axis. The 3-DoF joint with intersecting axes would be ideally represented by spherical joint surfaces. These are simplifications of the human joints with elastic cartilage and more complex surfaces.

The parameters of the defined joints are identified by numerical optimisations using the Nelder–Mead simplex algorithm. In non-convex optimisation problems it can happen that the optimiser finds a local optimum instead of the global optimum. The trade-off curve of the PIP3 joint (Figure 3.8) reveals a local optimum problem when optimising Equation (3.7): an ideal optimiser of 2ia and 2na should have found at least the orthogonal axes (2oia or 2ona) as a special case. Due to local optima, the result of the parameter identification may be sensitive to the optimisation starting point. Therefore, three equally spaced starting points for each axis were used. Some of the results were influenced by the starting point while others were not. For example, the parameters of the CMC1 joint (2ona) were optimised with three different starting points for each of the two axis orientations and three different starting points for the axis offset. The results are slightly sensitive to the axis orientation starting points, with the rotational error ranging from 3.0° to 3.2° and the translational error ranging from 2.1 mm to 4.0 mm. The variation of the axis offset starting point has no effect on the results. In some other joints, for example the IP1 joint (1a), optimisation starting points have no effect on the result, with a rotational error of 4.8° and a translational error of 1.0 mm for all starting points.



4

Hand models for grasp simulation

The designer of a robotic hand is faced with the question, among others, how many axes of rotation the robotic hand should have, and how they should be placed and oriented. For anthropomorphic hands, it is interesting what the functional consequences of the axis locations in the human hand are.

Testing hand models with different number and placement of rotation axes in simulation may save costly iterations in hardware. In this Chapter, such simulations are demonstrated at the example of the three human hand models with different thumb configurations and one robotic hand model performing six prescribed grasps.

4.1 Methods

In this Section, the hand models and prescribed grasps are presented and the functionality of the grasp simulation is explained. Furthermore, the use of one of the hand models in the simulation of an astronaut is described.

4.1.1 Grasp simulations

The human hand models are based on [MRI](#) images of the hand of one 29-year-old female subject [Stillfried et al., 2014] (Chapter 3). Three variants are used: The first model has 22 [DoF](#), where the thumb [CMC](#) joint has two non-

intersecting non-orthogonal axes, the **MCP** joints of thumb and fingers have two intersecting orthogonal axes each and the remaining joints have one axis each, including one joint between the ring and little finger **MC** bone (Figure 4.1a). The second model is the same as the first one except that the joint axes of the thumb **CMC** joint are orthogonal, since orthogonal axes are probably more easily copied in robotic hands (Figure 4.1b). The third model is the same as the first one except for the thumb **MCP** joint, which has only one axis, which is another simplification often found in robotic hands (Figure 4.1c).

The robotic hand model is a model of the DLR/HIT Hand II [Liu et al., 2008]. It has 15 **DoF**: one for ab-/adduction and two for flexion of **MCP** and coupled **PIP** and **DIP** joints, in each of five identical fingers.

Grasp experiments are carried out using a graphical user interface (**GUI**) developed by Theodoros Stouraitis. The **GUI** is based on OpenRAVE. In each grasp experiment, a pair of a hand and an object is loaded, out of four hand models and six object models, respectively. The pose of the hand with respect to the object is manually adapted for each desired grasp, such that a feasible grasping pose for the hand is obtained. The joint angles are manually changed to bring the fingers into the desired posture close to the object, so as to generate the desired hand preshape. Subsequently the joint angles are automatically driven until finger surfaces contact the object. The contact points and normals are retrieved and it is tested whether force closure is possible with the given grasping configuration.

The force closure criterion is achieved when the contact forces are able to balance finite forces and torques applied to the object in any direction. The forces are considered to always lie within the friction cone of each point. For determining the angle of the friction cones to the normal vectors, a static friction coefficient of 0.4 is assumed.

In the case of a successful force closure, a grasp score is calculated. For this, the force-torque wrenches on the centre of the object are calculated. The wrenches result from assumed forces with a magnitude of 1 (unit forces) along the edges of the discretised friction cones at the contact points. The grasp score is defined as the volume of the convex hull that spans over the wrenches. The distances used for calculating the torques are scaled by the maximum position coordinate of the grasp locations:

$$\text{GraspScore} = \text{Volume} \left(\text{ConvexHull} \left(\left(\frac{\mathbf{f}_{i,j}}{(\mathbf{r}_{\text{COM},i}/x_{\max}) \times \mathbf{f}_{i,j}} \right) \right) \right), \quad (4.1)$$

where $\mathbf{f}_{i,j}$ is the j -th unit force at contact location i , $\mathbf{r}_{\text{COM},i}$ is the vector from

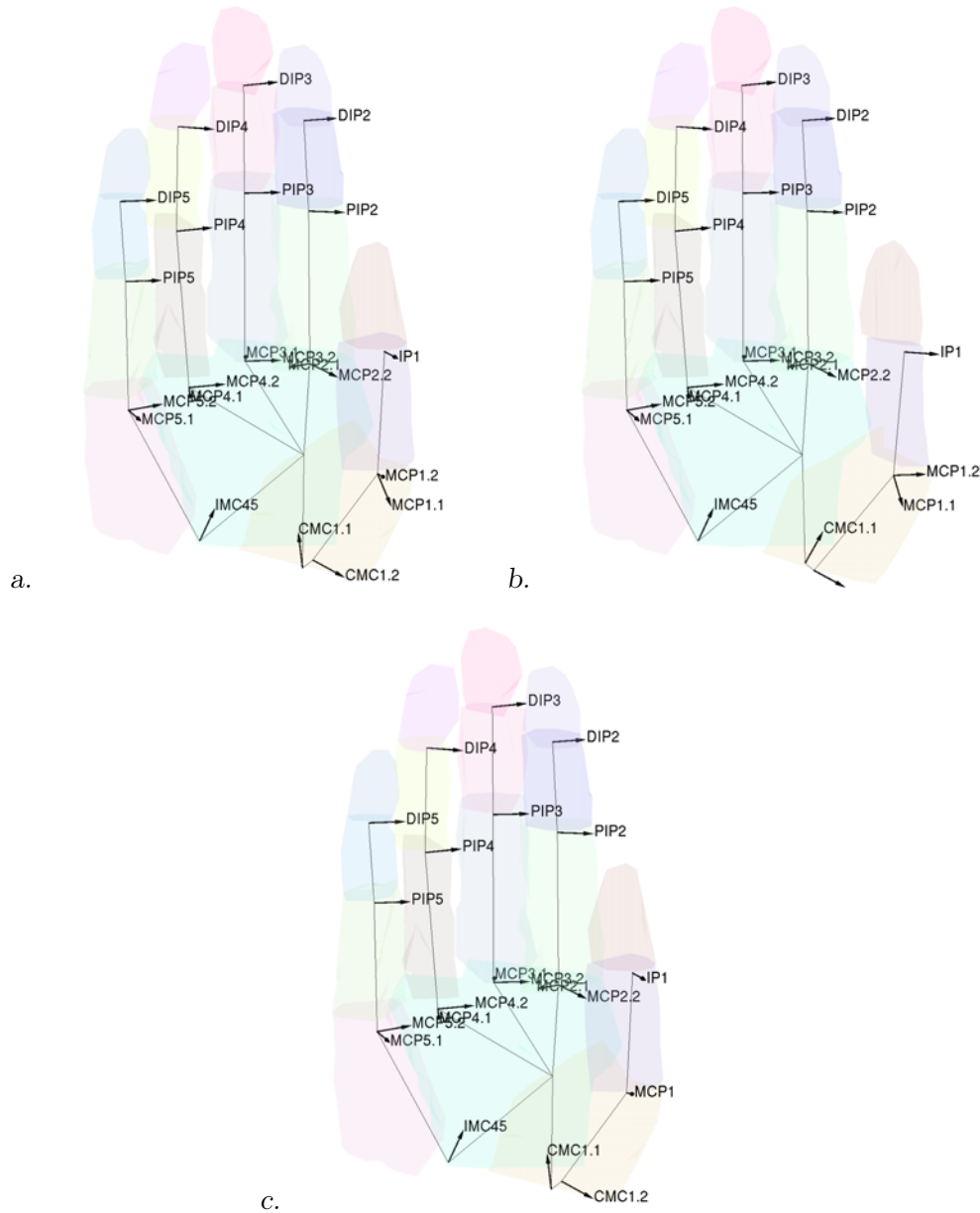


Figure 4.1: The kinematics of the three human hand models that are compared in the grasp simulations. a. 22-DoF model where the **CMC1** joint is of type **2na** and the **MCP1** joint is of type **2oia**. b. 22-DoF, **CMC1:2ona**, **MCP1:2oia**. c. 21-DoF, **CMC1:2na**, **MCP1:1a**

the centre of mass to the contact location i , and x_{\max} is the maximum position coordinate of all grasp locations.

Six different grasps are tested: power grasps of a small and a large elliptical cylinder; a precision grasp of a sphere; a grasp of a mug with two fingers through the handle and the thumb on top of the handle; the grasp of a ballpoint pen where the thumb is in a suitable position to press the retraction button; and the grasp of a power drill where the index finger is in a suitable position to press the trigger. The grasps are inspired by typical human grasps from the taxonomy by Cutkosky [1989] (Figure 4.2). In order to increase the similarity to the human grasps and to make the grasp description more specific, the following constraints are introduced: In the grasps of the cylinders and the power drill, the object shall touch the palm. In the grasps of the sphere, pen and mug, palm contact shall be avoided.

The grasp of the large cylinder with the second hand model (22-DoF and orthogonal axes) and with the DLR/HIT Hand II model is simulated by five operators. The differences between the mean grasp scores of both models are statistically analysed using a repeated-measures one-factor analysis of variance (ANOVA) [Salarian, 2008].

4.1.2 Astronaut hand simulation for exoskeleton design

The hand model created in this thesis is also used in STAMAS [2013], an EC-funded project that investigates the use of smart materials in space applications, as part of the master's thesis of González Camarero [2014]. One of the sub projects is the creation of a hand exoskeleton device that shall help astronauts to perform tasks during extra-vehicular activity (EVA). These tasks are particularly stressful for the astronaut, because the pressurised gloves that they wear during EVA impose additional effort during grasps.

The hand model is used for calculating the force vectors that the external device applies on the glove and the hand, and to visualise the system. The goal is a simulation of the astronaut, glove and support system for evaluating designs before manufacture.

4.2 Results

As expected, it was possible to achieve power grasps with most of the hand model-object combinations. The results are shown in Figure 4.3.

By this experiment, no difference could be identified between the different simplifications of the human hand model.

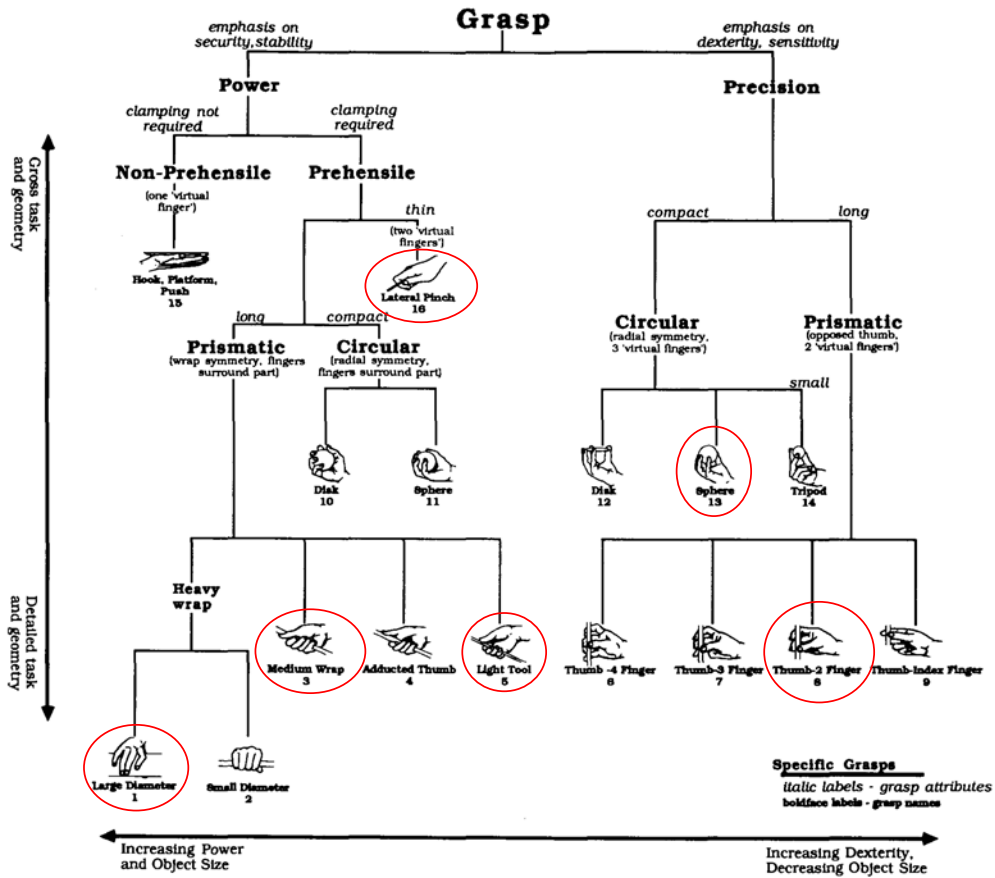


Figure 4.2: The partial grasp taxonomy by Cutkosky [1989]. The grasp of the small and large cylinder correspond to the Medium Wrap and Heavy Wrap (Large Diameter) grasps, the Precision Grasp of a sphere is part of the taxonomy, the grasp of the mug is a special case, possibly represented by a combination of the Thumb-2 Finger grasp and the Lateral Pinch grasp, the grasp of the ballpoint pen is a Light Tool grasp augmented by a manipulating thumb and power drill grasp is a Heavy Wrap (Large Diameter) grasp augmented by a manipulating index finger. Adapted from Cutkosky [1989] ©1989 IEEE (ovals added).

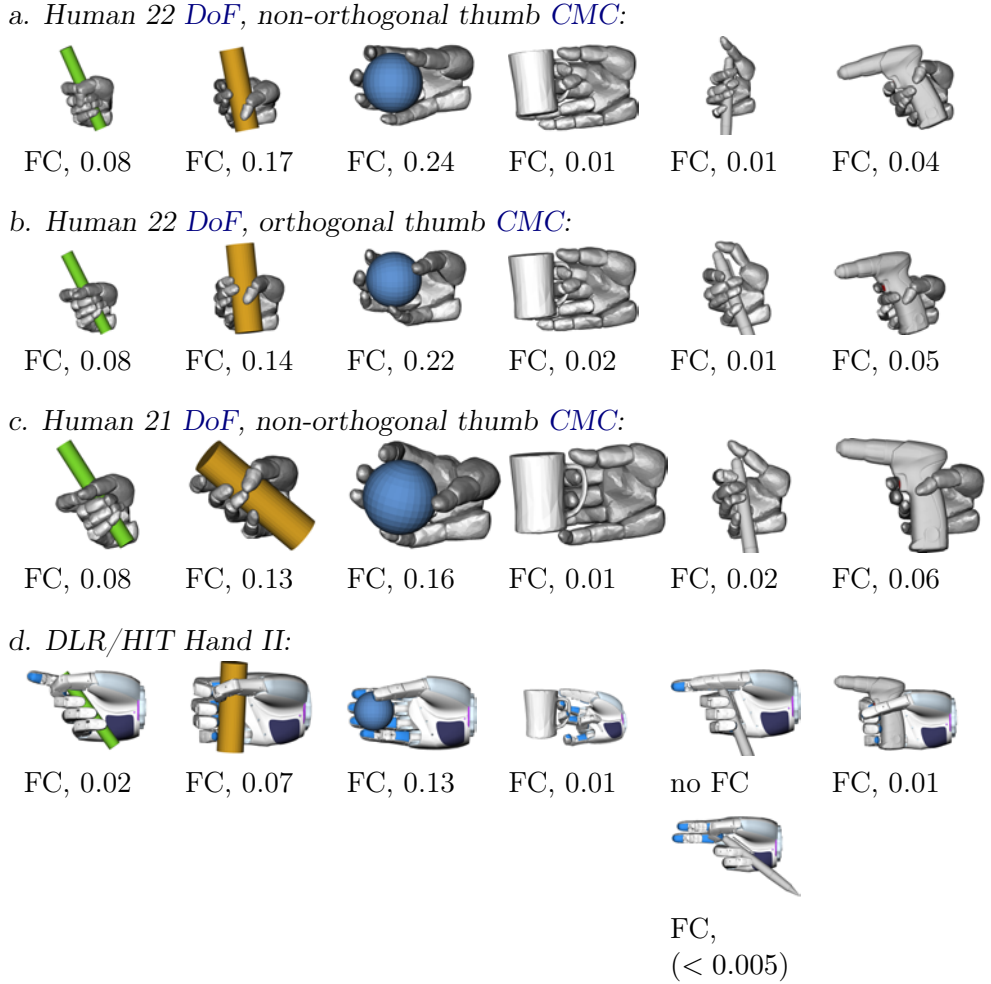


Figure 4.3: Results of the simulated grasp experiments of a human hand model and several artificial hand models grasping a small and large elliptical cylinder, a sphere, a mug, a pen and an electric screwdriver. Grasps in which force closure is achieved are marked with the letters “FC” and the grasp score is given. For the definition of the grasp score, see the text in Section 4.1.1 and Equation (4.1). Note that the grasp of the mug by the robotic hand would be extremely difficult to achieve with a real robot, because the gaps between finger and mug are extremely small.

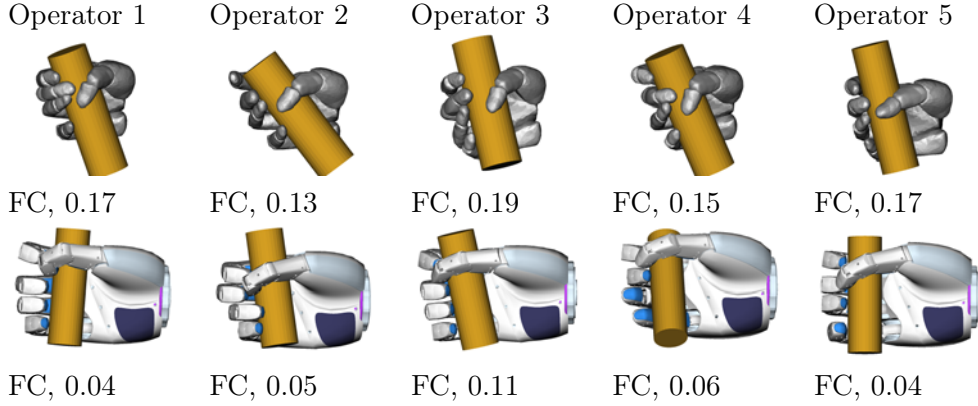


Figure 4.4: Simulated grasps of the large cylinder by five operators. There is some variation of the grasp score between the operators, but there is a significant difference between the mean grasp scores of the two hand models. FC: force closure.

The DLR/HIT Hand II is also able to perform all six grasps. An exception is the pen grasp. The DLR/HIT Hand II achieves a power grasp of the pen with an oblique but possibly functional position of the thumb tip on the retraction button. However, the grasp is different from the grasp usually applied by humans. Whereas humans usually hold the pen between the **PP** and the **PD** of each finger in order to work the button with the thumb, the DLR/HIT Hand II needs to hold the pen between the palm and the **PD** of only ring and middle finger (see the respective grasp in Figure 4.3).

The grasp of the large cylinder with the DLR/HIT Hand II model and with the human hand model with 22 **DoF** and orthogonal thumb **CMC** axes was simulated by five operators. The results are shown in Figure 4.4. The mean \pm standard deviation (**SD**) grasp score over all operators is 0.16 ± 0.02 for the human hand model and 0.06 ± 0.03 for the robotic hand model. The results of the **ANOVA** show a statistically significant difference of the mean grasp scores ($p < 0.001$).

4.3 Discussion

Using the grasp simulations, it was not possible to find any substantial difference between the different thumb models (4 or 5 **DoF**, orthogonal or non-orthogonal axes). However, the robotic hand model was not able to hold one of the six objects (the pen) using the prescribed grasp type. Furthermore, the grasp scores for the human hand models were mostly higher than the ones for the robotic hand model.

A possible explanation for the fact that the DLR/HIT Hand II cannot hold the pen between **PP** and **PD** is that the finger segments are quite thick in relation

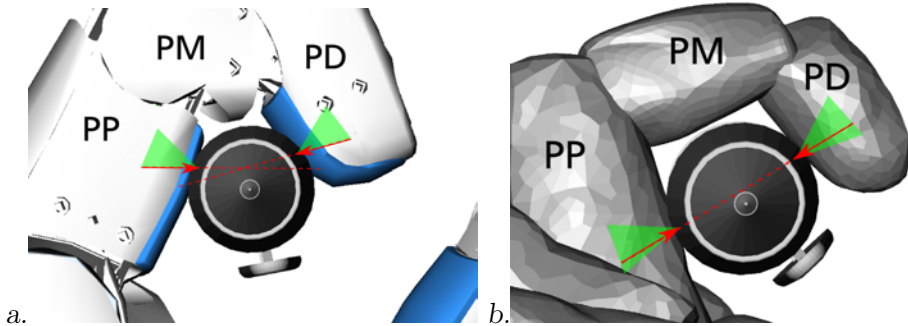


Figure 4.5: Grasp of a pen between the phalanges of a finger. *a.* Attempted grasp by the DLR/HIT Hand II. The angles of the the **PP** and the **PD** are such that the normals point away from the **PM**. There are no grasp forces (arrows) within the friction cones that can balance each other (dotted lines). *b.* Successful grasp by the human hand model. While still pointing away from the **PM**, the angle between the normals of the **PP** and the **PD** is much smaller, so that forces within the friction cones can be found that balance each other.

to their length. Therefore, when trying to hold the pen between the **PP** and the **PD**, the closing motion is stopped early by the pen, so that the surface normals of the **PP** and the **PD** point away from the **PM**. This means that the normal forces drive the pen away from the **PM**. The only possibility for keeping the pen close to the **PM** is given by the friction forces. However, with the assumed friction coefficient, they are too low (Figure 4.5). This limitation does not only apply to the grasp of the pen, but to all grasps of the type Light Tool (Figure 4.2).

The reason that only ring and little finger are used in the alternative grasp of the pen is that the abduction range of the thumb is small compared to the size of the hand, so that the button of the pen needs to be close to the middle finger so that it is reachable by the thumb.

Even though not all grasps can be achieved, with some creativity, other grasps can be found that fulfil the same function.

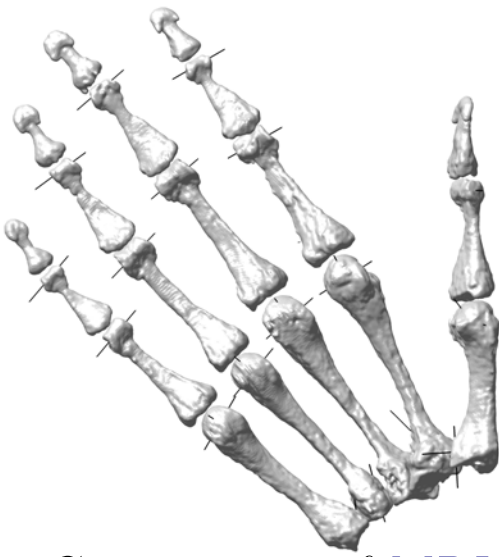
A possible explanation for the higher grasp scores of the human hand model is that it has more **DoF** (human: 22 **DoF**, robot: 13 **DoF**). Therefore, more contact points can be obtained, for example, at all three phalanges. Since the grasp simulation assumes unit forces at each contact location, the volume spanned by the force-torque wrenches can be higher.

A limitation of the grasp simulations is that the tissue softness is not modelled. The softness of the tissue enables much larger contact areas and more widespread contact points than the rigid contact, which increases the stability of the grasp. On the downside, the soft tissue could lead to a lower grasp stiffness in the face of external perturbations.

A further limitation is that unit forces are assumed at each contact location instead of the real force capabilities. Because of both limitations, the calculated grasp score should not be treated with too much of importance.

The results of the grasp simulations contain a subjective element, because the grasps are pre-shaped manually by a human operator. Repeated grasps of one object with five operators show that there are indeed differences between the operators. However, the differences between the operators are small in comparison to the differences between the hand models. Therefore, the subjectivity does not destroy the ability of the grasp score to roughly indicate the grasp stability of hand model–object combinations.

In summary, an application of an MRI-based hand model has been shown that takes advantage of the joint axes which were optimised in the modelling process Chapter 3 as well as of the surface geometries extracted from one of the MRI images.



5

Comparison of MRI and MoCap for hand modelling

A common method for measuring hand and finger postures is optical surface marker tracking, where markers are attached to the skin and the fingernails of the subject's fingers and hand. The workspace is surrounded by multiple cameras, and the marker positions are triangulated from the camera images. Often the markers are covered with a retro-reflective layer and the cameras are equipped with an infra-red light source for a high contrast between the markers and the background.

The advantages of optical tracking over [MRI](#) are that the equipment is much more affordable, and the acquisition times are not as high: while an [MRI](#) recording of a hand with a resolution of 1 mm^3 per voxel takes about two to three minutes, optical tracking systems typically record at least 100 frames per second. Furthermore, the computation of the pose of a segment is very efficient with [MoCap](#) and can be done online (for example, with the closed-form solution by Horn [1987]), whereas the registration of the bones from [MRI](#) images is computationally intensive.

On the downside, [MoCap](#) of surface markers measures the movement of the skin and not of the bones. Since the skin is soft and elastic, it does not fit well with the rigid-body approach that is commonly used with skeletal modelling.

Therefore, the skin movement with respect to the bone is often ignored and the skin markers are assumed to be rigidly connected to the underlying bone. The modelling error that comes from ignoring the skin movement is known as soft tissue artefact (**STA**).

It is conjectured that the **MRI** method will lead to lower residuals than **MoCap**, because the measurements are not disturbed by **STA**. The null hypothesis is that the mean residuals are equal. In this Chapter, it is tested whether the measurement of bone poses with **MRI** really leads to more accurate results than the measurement of skin marker positions with **MoCap**, when a hand is modelled as a chain of rigid bodies. Furthermore, if this is the case, it investigated how much worse **MoCap** is with respect to **MRI**.

5.1 Methods

Kinematic hand models are built based on **MRI** data and based on **MoCap** data. The residual rotational and translational discrepancies of both models are compared.

5.1.1 **MRI** measurements of finger segment poses

The **MRI** measurements for this comparison are similar to the measurements described in Section 3.1.1.

Both the **MRI** and the **MoCap** measurements are taken of the same subject, a 30-year-old male with no history of hand injuries who gave informed consent to the procedure. Due to time constraints, only one reference posture and 19 other postures are recorded with **MRI**, using a so-called turboFFE sequence and a spatial resolution of (1 mm)³. These are a subset of the postures in Table 3.1, namely the ones marked with an asterisk.

5.1.2 **MoCap** measurements of finger segment poses

For **MoCap**, a Vicon system (OMG plc, Oxford, UK) with seven 0.3-megapixel cameras is used. One finger is recorded at a time, with three markers per finger segment (Figure 5.2). Markers with a diameter of about 4 mm are used. They are spherical except for a flat section at the bottom, where they are attached to the skin or to a piece of cardboard using double-sided adhesive tape. The pieces of cardboard are attached to the skin, as well. The markers are covered with retro-reflective material. The cameras are placed in a semi-circle around the workspace (Figure 5.1).



Figure 5.1: The setup of the cameras for the MoCap measurements. The cameras are placed around the workspace, approximately in a semi-circle with a radius of 1 m.

The cameras are fitted with infra-red light sources and a filter that transmits infra-red light. The light reflected by a marker appears as a circle on the camera images. The centres of the circles are used for determining the direction of the marker with respect to the cameras. The 3D position of the marker lies at the intersection of the direction lines (“rays”) of different cameras. To account for measurement noise, the software allows setting a distance threshold up to which rays are treated as intersecting. This method of optical measurements is also called stereo-photogrammetry.

One reference time sample and nineteen representative other samples are selected from the captured data.

Whenever there are at least three non-collinear markers per segment (MPS), the pose (position and orientation) of the segment can be measured. The pose in each time frame is calculated by placing a coordinate system in the following way: The first marker is the origin; the line between the first and second marker is the x direction; the y direction is perpendicular to the marker plane, along the cross-product between the x direction and the line between the first and third marker; the z direction is along the cross-product between the x and y direction. One finger is measured at a time, with the marker sets moved from finger to finger and a constant set of three markers on the back of the hand. This is done to facilitate automatic labelling of the markers according to the edge lengths of the triangles that they form: it is easier to find three different triangles for one finger than to find 15 different triangles for all five digits.



Figure 5.2: Placement of the markers on the fingers for the MoCap experiment. One finger is measured at a time, with the marker sets moved from finger to finger and a constant set of three markers on the back of the hand (Figure 5.2). This is done to facilitate automatic labelling of the markers according to the edge lengths of the triangles that they form.

5.1.3 Modelling of finger joints

One joint instead of three joints is used to model the palm, because the motion of the single metacarpal bones is difficult to discriminate with MoCap. The same fifteen joints for fingers and thumb as described in Chapter 3 are used. The thumb CMC joint is modelled with two non-orthogonal, non-intersecting axes (2na), the MCP joints are modelled with two orthogonal, intersecting axes (2oia) and the remaining joints are modelled with single axes (1a). The axis parameters and residual rotational and translational discrepancies are modelled as described Chapter 3.

5.1.4 Modelling of kinematic chains

Additionally, whole finger postures are matched with both methods. For this, the joints are concatenated to form kinematic chains. The global pose and the joint angles are optimised to minimise the mean rotational and translational discrepancies between the modelled and measured bone poses. For doing so, a weighting between the rotational and translational discrepancy is decided. One millimetre of translational discrepancy is treated with the same weight as one degree of rotational discrepancy.

Kinematic chains are sequences of joints and links such that parent joints and links influence the poses of child joints and links, for example, whole fingers or whole hands. There are three types of kinematic chains:

1. simple chains, in which each child segment has exactly one parent segment and each parent segment has one child segment, except for the first and last segment, which lack parent and child, respectively;
2. branching chains (tree kinematics), in which a segment may have multiple children but not multiple parents;
3. parallel chains, in which a segment may have multiple parents.

Here only simple chains shall be considered.

The advantages of modelling whole chains instead of single joints are:

1. pose measurements of more segments are used for the identification of the static parameters, leading to higher overall accuracy;
2. it is not necessary to measure the full pose of each segment—single position measurements or even missing information per segment are possible, as long as the information in the whole chain suffices to identify the static parameters. For example, the static parameters of a chain with not more than six axes can be identified using full pose information of only the last segment (end effector); this procedure is also applied in robotics [Khalil and Dombre, 2002].

The cost function for the optimisation of the static parameters of the kinematic chains differs from the one single joints (Equation (3.8)) in that the modelled and measured segment poses are compared not in the coordinate systems of their respective parents but in one common base coordinate system for all segments:

$$\{\boldsymbol{\xi}_{\text{opt}}, \mathbf{q}_{\text{opt}}(t)\} = \arg \min_{\boldsymbol{\xi}, \mathbf{q}} (\epsilon),$$

with

$$\epsilon = \underset{i \in \{1, \dots, n_s\}, t \in \mathcal{P}}{\text{mean}} \left[w_t \left\| {}^{\text{base}}T_{i,\text{meas}}(t)_{(1:3,4)} - {}^{\text{base}}T_{i,\text{mod}}(\boldsymbol{\xi}, \mathbf{q}(t))_{(1:3,4)} \right\| + w_r \text{RotationalDistance}\left({}^{\text{base}}T_{i,\text{meas}}(t), {}^{\text{base}}T_{i,\text{mod}}(\boldsymbol{\xi}, \mathbf{q}(t))\right) \right], \quad (5.1)$$

where $i \in \{1, \dots, n_s\}$ is the index of the segment.

The modelled posture ${}^{\text{base}}T_{i,\text{mod}}(\boldsymbol{\xi}, \mathbf{q}(t))$ is calculated recursively by reusing the pose of the parent segments and only calculating the forward kinematics between the segment and its parent:

$${}^{\text{base}}T_{i,\text{mod}}(\boldsymbol{\xi}, \mathbf{q}(t)) = {}^{\text{base}}T_{p(i),\text{mod}}(\boldsymbol{\xi}, \mathbf{q}(t)) f_i(\boldsymbol{\xi}_i, \mathbf{q}_i(t)),$$

where $p(i)$ is the number of the parent segment (in simple chains, $p(i) = i - 1$), and $f_i(\boldsymbol{\xi}_i, \mathbf{q}_i(t))$ is the forward kinematics function of the joint that connects the parent segment with the i -th segment.

5.1.5 Comparison of the residuals

The empirical distributions of the residuals are plotted in Figure 5.3 to see whether they are close enough to a normal distribution, so that a Student's t -

test can be applied meaningfully. The lines in Figure 5.3 connect points whose x -coordinates are the bin centres of variable-width histograms and whose y -coordinates are the number of data points (samples) in the respective bin divided by the bin width. The bin widths are chosen so that each bin contains an equal number of samples. The number of bins is determined according to the so-called Rice rule:

$$n_{\text{bins}} = \text{ceiling}((2 \times n_{\text{data_points}})^{1/3}).$$

The resulting histograms are different from normal distributions in a number of ways. Firstly, they lack a peak towards which the frequency density monotonically increases and from which it monotonically decreases. Secondly, the distributions possess a right tail but lack a left tails. Due to the definition of the residuals, they cannot assume negative values.

Since the histograms of the residuals look rather different from normal distributions, the means \pm SD of the residuals errors are plotted in Figure 5.4 and compared visually.

5.2 Results

The results of the comparison between MRI and MoCap are shown in Figure 5.4. On the left, single bone poses are compared, and on the right, whole finger postures. The bars show the mean of the residual rotational discrepancies in degrees and the residual translational discrepancies in mm, respectively. The error bars show the SD. The value n is the number of bone poses. There are 19 hand postures, 16 joints and 19 bones. The MC2 and MC4 bones are part of two finger chains each: MC2 is part of thumb and index finger and MC4 is part of ring and little finger. So the maximum number of bone poses is $19 \times 16 = 304$ for single joints and $19 \times (19+2) = 399$ for whole fingers. Whenever the numbers are lower, the image quality of the respective bone was too low or a marker was occluded.

The mean rotational residual for single joints is 4.4° for MRI data explained by the MRI-based model and 4.7° for MoCap data explained by the MoCap-based model. The mean translational residual for single joints is 1.4 mm (MRI) and 1.2 mm (MoCap) respectively. The mean rotational residual for whole fingers is 3.5° and 3.6° , respectively. The mean translational residual for whole fingers is 1.2 mm and 1.5 mm, respectively.

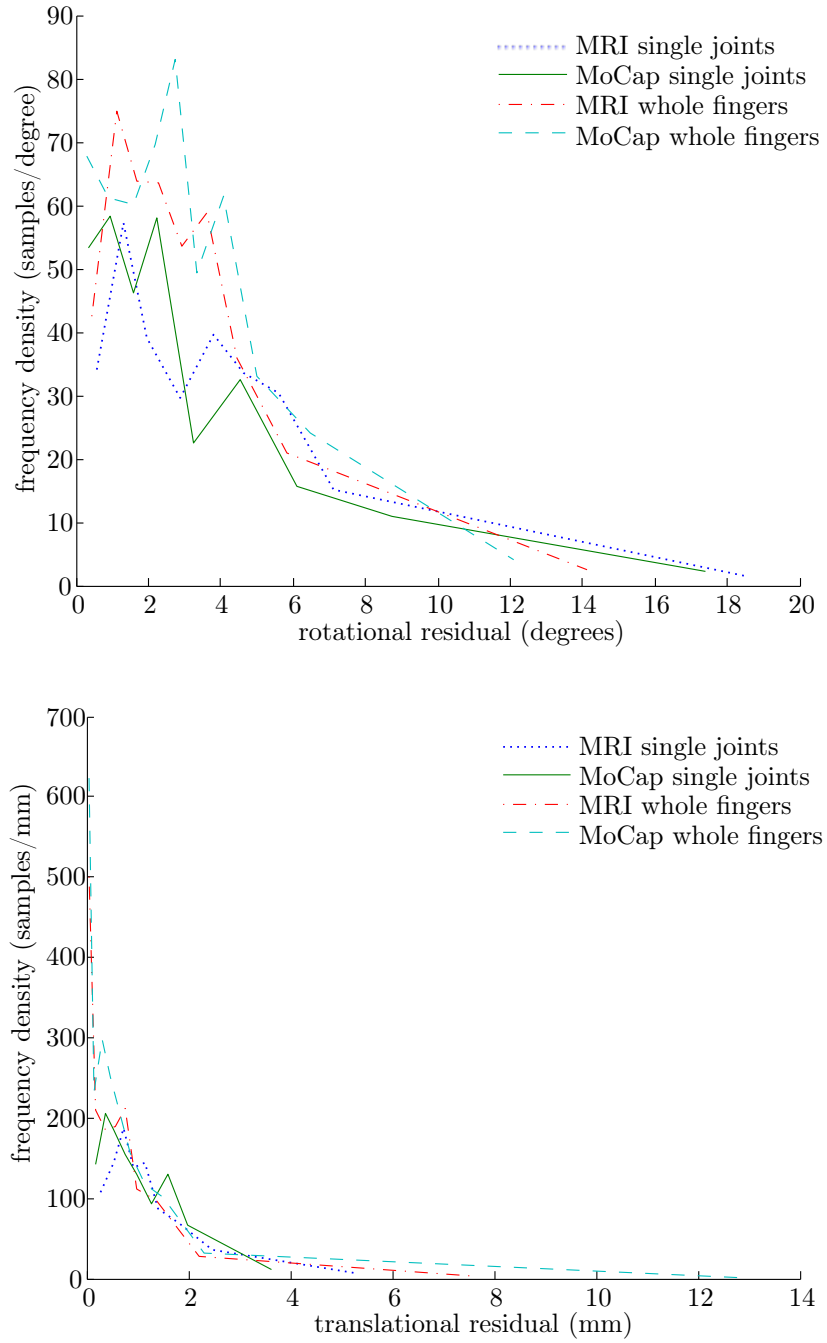


Figure 5.3: Histograms of the rotational and translational discrepancies between measured and modelled segment poses (residuals) in the comparison between MRI and MoCap (see Section 5.1.5).

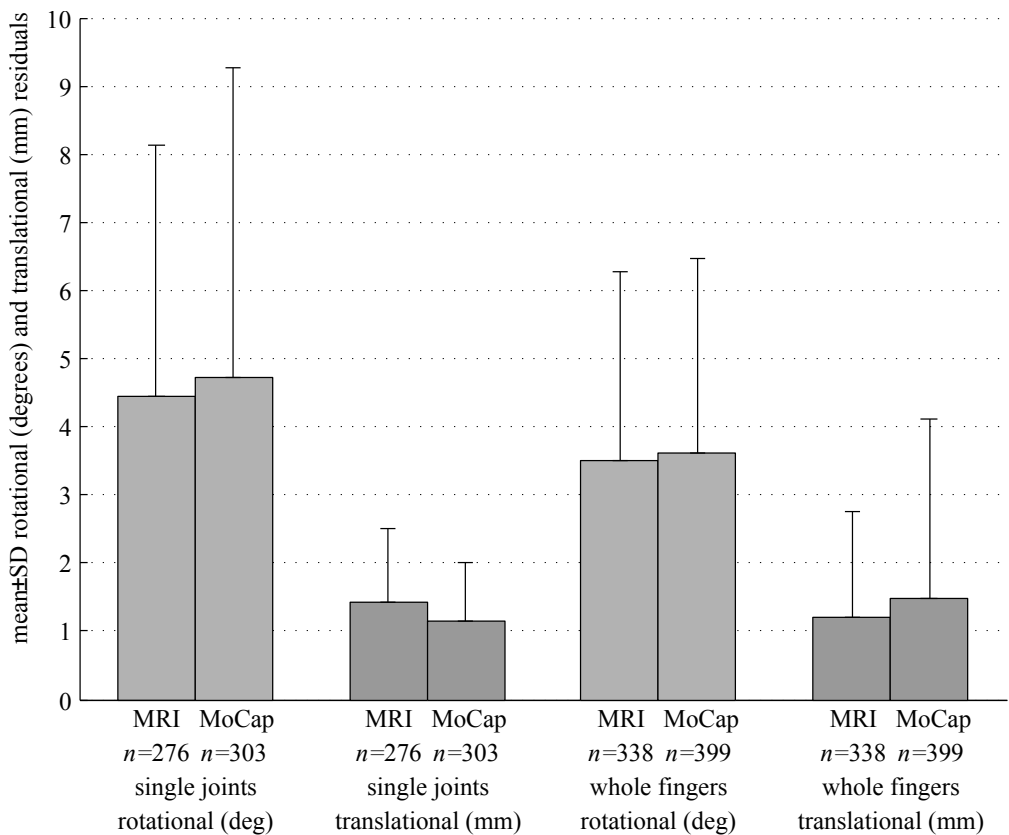


Figure 5.4: Comparison of MRI and MoCap. On the left, single bone poses are compared, and on the right, whole finger postures. The bars show the mean of the residual rotational discrepancies in degrees and the residual translational discrepancies in mm, respectively. The error bars show the SD of the residuals. The value n is the number of bone poses. Adapted from Stillfried et al. [2014].

5.3 Discussion

It was tested how well a reasonable rigid-body model with chains of rotation axes could be fitted to palm and finger segment poses which were measured using **MRI** and **MoCap**. The residual discrepancy between measured and modelled segment poses is caused by different factors:

1. measurement errors, that is, differences between the real movement and the measured movement;
2. numerical errors, mainly local optima in the identification of the static and dynamic joint parameters; and
3. model errors, that is, differences between the real joints and the modelled joints.

The same model was applied to both measurement sets, in which the postures of the same individual hand were recorded. Therefore, it can be expected that the model error affects both measurements similarly. Also, the same optimisation method was applied for the identification of the static and dynamic parameters based on both measurements. Furthermore, the risk of local minima was reduced by repeating the optimisations with different starting points. Therefore, it can be expected that any major differences in the residual errors of models based on both measurement methods are due to measurement errors.

It is believed that this is the first work that compares the residual modelling errors of the same individual limb whose movements were measured with two different methods. The advantage of this approach is that no ground-truth data of the movement is necessary. On the downside, the numerical errors of the parameter optimisation and the model errors themselves contribute to the total residual modelling error. Therefore, this method is not able to estimate the absolute value of the measurement error. However, it can be used to make a relative comparison between the measurement methods.

The experiment results do not show any substantial accuracy advantage of **MRI** over **MoCap**—contrary to the initial hypothesis. In one of the four tested categories, **MoCap** is even slightly better, but all in all, the values for both methods are very similar. Presumably the errors that occur due to the segmentation and registration of the bones in **MRI** are of similar size as the errors that occur due to **STA** in **MoCap**.

Therefore, it seems that accuracy is not a deciding criterion for the choice between **MRI** and **MoCap**. Other criteria can play a role. For example, with **MRI**, a model with surface geometries can be created (see Chapter 4), while

with [MoCap](#), continuous movements can be measured instead of only static postures.

The mean errors of 1–2 mm and 3–5° are moderate and in a similar range as the ones in Chapter 3. For example, the grasping of medium-sized objects is probably not affected by position and orientation differences in this order of magnitude. In human fingers, the mobility of a grasped object due to tissue softness is in the same range. However, the variance of the residual errors is rather large.

Interestingly, the method by [Cerveri et al. \[2007\]](#), which places the rotation axes according to the anatomical landmarks of the hand, resulted in similar ranges of position errors: their [RMSE](#) values over all samples of 15 task repetitions were between 0.4 and 3.3 mm, depending on the subject, task and marker. There were four subjects, four tasks, four markers on the thumb and three markers on the index finger.

On a first view, it appears surprising that the average residual errors are lower for whole fingers than for single fingers: when considering the posture of a whole finger, an error of a proximal joint can also affect joints that are situated distally to it, and therefore lead to a larger error. On the other hand, when considering a whole finger, the global pose of the first bone was optimised. This optimisation, which is not conducted when considering single joints, can lead to a reduction of the residual errors. Furthermore, in single joints the pose of the proximal bone is considered to be given and only the residual pose errors of the distal bone is considered. Since the proximal bones are larger than the distal bones, it is possible that their registration error is lower. Since they are included in the analysis of whole fingers, they may be able to reduce the mean residual error.

The creation of hand models based on [MoCap](#) may further be improved by using a larger number of postures and an explicit model for the skin movement (see Chapter 6).



6

Validation of the skin movement model by Zhang et al.

In order to accurately model the hand kinematics using surface marker measurements and to compensate for STA, the rigid-body approach for the skeletal posture needs to be complemented with elastic modelling elements that account for the movement of the skin relative to the bones.

Several elastic models for the skin have been proposed [Zhang et al., 2003, Dumas and Cheze, 2009, Corato et al., 2009]. The model by Zhang et al. [2003] is particularly interesting because it models the movement of the skin near joints, where the skin movement is the largest.

In this Chapter, the movement of the skin with respect to the bone is measured using MRI. It is tested how well the skin movement model by Zhang et al. [2003] is able to explain the measured skin movement.

6.1 Methods

For validating the skin movement model of Zhang et al. [2003], positions on certain points on the skin are measured using markers in MRI, the relative movement with respect to the bone is calculated and joint parameters are fitted to the bone poses. The marker positions are predicted using the joint angles and the skin model. The parameters of the skin model are optimised. The differences

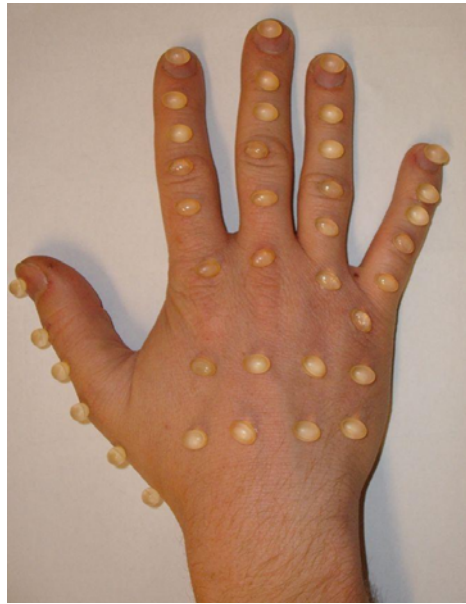


Figure 6.1: Photograph of Soledum capsules on CMC, MCP, PIP and DIP joints and MC, PP, PM and PD bones. Reproduced from Gustus et al. [2012].

between the measured and modelled marker positions are calculated.

6.1.1 Measurement of skin movement using MRI

MRI-sensitive Soledum capsules (Casella-med, Cologne, Germany; spheroids with diameter 7 mm and long axis 10 mm) are attached to the skin on the dorsal side of the hand of one subject (Fig. 6.1) over the CMC, MCP, PIP and DIP joints, as well as the MC, PP, PM and PD phalanx bones. For the validation of the skin model, the markers over the MCP, PIP and DIP joints are considered. MRI images of 20 different hand postures are recorded ($n_p = 20$). The postures are chosen such that each joint is moved through its whole range of motion (see postures with asterisks in Table 3.1). The volumes of the bones (cancellous part) and of the capsules are segmented from the MRI images.

One posture (flat hand) is designated as the reference posture. The poses of the bone coordinate system (BCS) and joint axes are determined as described in Stillfried et al. [2014]. The position of each skin marker is measured as the mean of the coordinates of the capsule volume weighted by the MRI intensity values. The marker positions are projected onto the sagittal plane¹ of the bone (Fig. 6.2).

The STA is quantified as the distance between the marker in the reference

¹flexion/extension plane, see Anatomical terms.

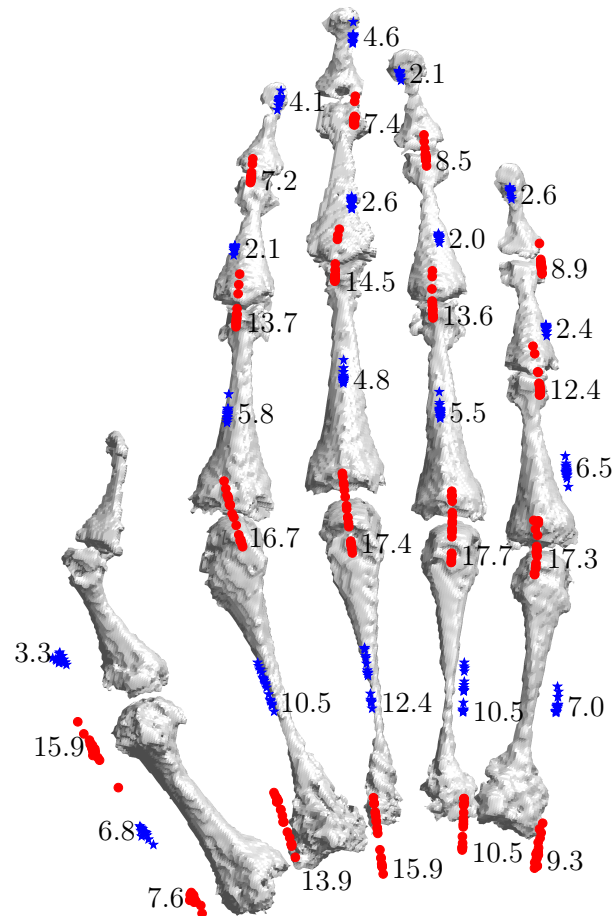


Figure 6.2: Relative movement of the markers in the sagittal planes of the closest bones; in the case of MCP, PIP and DIP markers, relative to the closest proximal bone (the surface between cancellous and cortical bone is shown). The range of the movement is given in mm. It is particularly large near joints (red dots in the colour version) and on the back of the hand, and comparatively small near the middle of the bones of the digits (blue asterisks in the colour version).

posture and the marker in another posture, both expressed in the BCS:

$$s_k = \|\mathbf{p}_{m,\text{meas},k} - \mathbf{p}_{m,\text{meas},\text{ref}}\|, \quad (6.1)$$

where s_k is the amount of uncompensated STA in posture k , $\mathbf{p}_{m,\text{meas},k}$ is the measured position of the marker with respect to bone B in posture k and $\mathbf{p}_{m,\text{meas},\text{ref}}$ is the measured position of the marker with respect to the bone in the reference posture. Here, the proximal bone is chosen as reference. The mean STA and its standard deviation are shown in the second column of Table 6.1 (mean STA \pm SD (mm), uncompensated).

6.1.2 Validation of the skin movement model of Zhang et al. [2003]

The amount $s_{\text{residual},k}$ of residual STA is the distance between the modelled and the measured marker position:

$$s_{\text{residual},k} = \|\mathbf{p}_{m,\text{meas},k} - \mathbf{p}_{m,\text{mod},k}\|, \quad (6.2)$$

where $\mathbf{p}_{m,\text{mod},k}$ is the modelled marker position.

The modelled marker position is calculated according to the model by Zhang et al. [2003] by rotating the marker from its initial position by an angle that is proportional to the skeletal joint angle:

$$\mathbf{p}_{m,\text{mod},k} = \text{Rot}(\mathbf{a}_1, c_1 \theta_{1,k}) (\mathbf{p}_{m0} - \mathbf{p}_1) + \mathbf{p}_1 \quad (6.3)$$

for 1-DoF joints and

$$\begin{aligned} \mathbf{p}_{m,\text{mod},k} = & \text{Rot}(\mathbf{a}_1, c_1 \theta_{1,k}) \left(\text{Rot}(\mathbf{a}_{2,\text{ref}}, c_2 \theta_{2,k}) (\mathbf{p}_{m0} - \mathbf{p}_{2,\text{ref}}) \right. \\ & \left. + \mathbf{p}_{2,\text{ref}} - \mathbf{p}_1 \right) + \mathbf{p}_1 \end{aligned} \quad (6.4)$$

for 2-DoF joints, where $\text{Rot}(\cdot, \cdot)$ is the rotation matrix (Equation (1)), \mathbf{a}_1 is the orientation of the first rotation axis, c_i is the factor that describes the proportionality between the i -th skeletal joint angle and the marker movement, $\theta_{i,k}$ is the i -th skeletal joint angle in posture k , \mathbf{p}_{m0} is the initial marker position when all joint angles are zero, \mathbf{p}_1 is a point of the first rotation axis, $\mathbf{a}_{2,\text{ref}}$ is the reference orientation of the second rotation axis (at $\theta_1 = 0$), and $\mathbf{p}_{2,\text{ref}}$ is a point on the second rotation axis at $\theta_1 = 0$.

As described in Section 2.4, the initial marker position \mathbf{p}_{m0} and the proportionality factors c_1 and c_2 can be optimised to best describe the skin movement.

The starting point of the optimisation is set as follows:

$${}^B\boldsymbol{p}_{m0,\text{start}} = {}^B\boldsymbol{p}_{m,\text{meas,ref}}, \quad (6.5)$$

$$c_{i,\text{start}} = 0.5. \quad (6.6)$$

The mean **STA** and its standard deviation obtained with these values are shown in the third column of Table 6.1 (mean **STA** \pm **SD** (mm), default values).

The optimal skin movement parameters minimise the mean amount of residual **STA** (Equation (6.2) with Equation (6.3) or Equation (6.4)):

$$\{{}^B\boldsymbol{p}_{m0,\text{opt}}, c_{i,\text{opt}}\} = \arg \min_{{}^B\boldsymbol{p}_{m0,c_i}} \left(\text{mean}_{k \in \{1, \dots, n_p\}} (s_{\text{residual},k}) \right). \quad (6.7)$$

The simplex algorithm by Nelder and Mead [1965], as implemented in Matlab, is used to find the optimal parameters.

The mean **STA** and its standard deviation using the optimised parameters, as well as the optimal parameters values, are shown in the fourth, sixth and seventh column of Table 6.1, respectively (mean **STA** \pm **SD** (mm), optimised values; optim. param.).

A leave-one-out cross-validation is performed, and the resulting mean and standard deviation of the **STA** are shown in column five of Table 6.1 (mean **STA** \pm **SD** (mm), cross-validated).

6.2 Results

The total amount of skin movement that was measured is shown in Figure 6.2. Its range is 7.6–15.9 mm near the **CMC** joints, 6.8–12.4 mm near the **MC** bones, 15.9–17.7 mm near the **MCP** joints, 3.3–6.5 mm near the **PP** bones, 12.4–14.5 mm near the **PIP** joints, 2.0–2.6 mm near the **PM** bones, 7.2–8.9 mm near the **DIP** joints and 2.1–4.6 mm near the **PD** bones. In all cases, the skin movement near joints is larger, often much larger, than near the middle of the neighbouring bones.

Further results of the skin movement measurement and the validation of the skin model by Zhang et al. [2003] are shown in Table 6.1. The first column shows the joint names in whose vicinity the marker movement is measured.

In the second column, the mean uncompensated marker movement (Equation (6.1)) and its **SD** are given. The mean over all postures and joints is 3.8 mm and the mean over all joints of the **SD** over the postures is 3.3 mm.

In the third column, the residual **STA** after applying the skin movement model

Table 6.1: Validation of the skin movement model using [MRI](#) measurements as ground truth.

joint name	mean STA \pm SD (mm)				optim. param.	
	uncompensated	default values	optimised values	cross- validated	c1	c2
MCP1	3.2 \pm 2.6	2.3 \pm 1.5	2.0 \pm 1.4	2.5 \pm 1.5	0.5	0.4
MCP2	6.8 \pm 4.0	3.7 \pm 2.3	3.2 \pm 1.7	3.7 \pm 1.7	0.5	0.8
PIP2	2.5 \pm 3.3	1.4 \pm 1.0	0.8 \pm 0.4	1.1 \pm 0.6	0.8	
DIP2	1.7 \pm 1.9	1.1 \pm 0.6	0.9 \pm 0.4	1.1 \pm 0.5	0.6	
MCP3	6.6 \pm 5.0	2.8 \pm 2.1	2.0 \pm 1.2	2.2 \pm 1.3	0.6	1.2
PIP3	3.6 \pm 4.4	1.7 \pm 1.1	1.4 \pm 0.9	1.6 \pm 0.9	0.6	
DIP3	1.7 \pm 1.6	1.7 \pm 1.2	1.2 \pm 0.9	1.1 \pm 0.9	0.4	
MCP4	7.2 \pm 5.4	3.1 \pm 2.5	2.0 \pm 1.3	2.4 \pm 1.2	0.8	0.7
PIP4	3.0 \pm 3.6	1.7 \pm 1.2	1.5 \pm 1.1	1.6 \pm 1.2	0.6	
DIP4	1.7 \pm 1.7	1.2 \pm 0.8	1.0 \pm 0.7	1.1 \pm 0.7	0.6	
MCP5	6.9 \pm 4.5	4.6 \pm 2.4	2.8 \pm 1.6	3.5 \pm 1.8	0.5	0.2
PIP5	2.9 \pm 3.1	2.3 \pm 1.4	1.7 \pm 1.2	1.9 \pm 1.3	0.7	
DIP5	2.1 \pm 1.7	1.7 \pm 1.1	1.3 \pm 1.0	1.4 \pm 1.0	0.7	
mean	3.8 \pm 3.3	2.3 \pm 1.5	1.7 \pm 1.1	1.9 \pm 1.1		

by Zhang et al. with the default values (Equation (6.2) with Equation (6.5)) is shown. Its overall mean is 2.3 mm (about 61% of the uncompensated movement) and its mean [SD](#) is 1.5 mm.

In the fourth column, the residual [STA](#) after applying the skin model by Zhang et al. with optimised values (Equation (6.2) with Equation (6.7)) is shown. Its overall mean is 1.7 mm (about 45% of the uncompensated movement) and its mean [SD](#) is 1.1 mm.

In the fifth column, the [LOOCV](#)-value of the above is given with a mean of 1.9 mm (50% of the uncompensated movement) and a mean [SD](#) of 1.1 mm.

All values are given for the marker positions projected onto the sagittal planes of the nearest bones.

6.3 Discussion

The measurements of skin movement with respect to the bone showed that it is always larger near joints than away from joints. Therefore, the model by Zhang et al. [2003] targets the most important part of the skin.

The model explains already with the default values close to 40% of the skin movement. Once its parameters are optimised, it is able to explain about 50% of it. (This value is cross-validated, so there is no risk of an overfit.) Thus, the

model is shown to be useful in compensating a large part of the skin movement. This percentage improvement is better than the one reported by the Dexmart project (18.2–27.8%, see Section 2.4). However, their absolute discrepancy between measured and modelled marker positions was lower (0.91–1.02 mm with rigid model and 0.66–0.80 mm with moving-marker model). Furthermore, the marker placement was different.

The residual skin movement of about 50% may be due to actual skin movement which was not represented in the model, but a part of it may also be due to noise in the measurement of the bone pose and the marker position.

The measurements were made with only one subject. Since the overall anatomy of the hand seems similar for most humans, it is expected that the qualitative results of this experiment are valid. However, in order to obtain quantitatively reliable results, more subjects would be needed.

Another limitation of the experiment was the limited accuracy of the bone orientation estimation around its longitudinal axis. Because of this, the marker positions had to be projected onto the sagittal plane, so that a full validation of the 3D movement of the markers was not possible.



7

Conclusion

This thesis presented a set of methods and investigations for improving the creation of hand movement models:

A method for determining joint types of joints of the human hand was developed. The method provides to its user a measure how well each joint type out of a given list is able to represent a set of measured segment poses. The user sets a threshold on this measure and the simplest joint that satisfies the threshold will be selected. A designer of a humanoid robotic hand can use this method for deciding which joint types the hand should have. The method was demonstrated on a set of representative hand postures recorded using magnetic resonance imaging ([MRI](#)). The measure of the goodness of fit of the joint was cross-validated, thereby avoiding an overfit of the joint parameters to the measured poses. The sources of measurement errors were identified and the contributions of each of the sources were estimated.

By defining the joint types of all the joints of that hand, and additionally measuring and segmenting the hand surface, a virtual hand model was created. Applications for the resulting hand model were shown: grasp simulations of different objects with three human hand models with different thumbs and a robotic hand model, as well as simulations for an exoskeleton. In simulations of specific grasps of six objects, no differences were found between the thumb models of the human hand. The robotic hand model was able to perform five

of the six grasps as specified, and one of the grasps only with a different grasp type. A grasp score that estimates the ability to resist external perturbations was in most cases higher for the human hand models than for the robotic hand model, probably due to the higher number of [DoF](#) resulting in a higher number of contact points. An investigation about the subjectivity of the results with one object, two hand models and five operators showed a moderate operator-dependent variability of the grasp score compared to the hand-model-dependent variability of the grasp score.

A comparison of measurement methods could not detect any improved precision when using [MRI](#) instead of optical motion capture ([MoCap](#)). The mean residual error for single joints is in both cases around 1 mm (translational) and 5° (rotational).

The skin movement model by Zhang et al. [2003] was validated. It can further improve [MoCap](#) measurements by explaining a substantial amount of the skin movement relative to the bones.

7.1 Limitations

A limitation of most of the studies in this thesis is that they were conducted with only one subject, which was in part due to the limited availability of the [MRI](#) machine. Therefore the results cannot be treated as information about the human hand in general, but rather as proof of concept of the presented methods. However, it can be argued that most of the human hands are able to perform most of the tasks necessary for daily living very well. Hence, understanding and copying the functionality of one of them can already provide helpful insights for the design of robotic hands. Still, in order to discern which properties are a result of natural variation and which ones are crucial for the functioning of the human hands, data from a larger set of human hands will be needed.

In the method for selecting the joint types, the list of joint types is necessarily limited. In this thesis, only rotary joint types with up to three rotation axes were considered. This seems to be a good approximation for most joints. However, the [CMC](#) joint of the thumb seems to perform more complex movements that possibly include rotations coupled with translations. Also, the movement of the little finger [IMC](#) joint seems to be more complex than a simple rotation, with the head of the [MC5](#) bone first moving in palmar direction and then in palmar-radial direction.

Generativeness may be an important property for humanoid hands, as it allows the user to predict the kind of movements that the hand can do. In this

thesis, no method was found for quantifying generativeness. While it is closely linked to the number of **DoF**, it is not exactly the same. The range of motion of the joints was determined independently for each **DoF**. However, there are interdependencies between joints, some of them rather obvious, and probably also between the **DoF** of a multi-**DoF** joint. For example, the difference between the flexion angles of the **MCP2**, **MCP3**, **MCP4** joints is limited. These interdependencies are not modelled, thereby allowing some unnatural postures.

A general objection to kinematic modelling of the human hand is that *the* human hand does not exist. Of course, each individual hand differs from the next. But, as Grebenstein [2010] points out, there are “seven billion perfect hands”, that is, each of these different hands is able to perform the movements needed in daily living. This means that if a robotic hand is able to perform the same movements as any individual hand, it will be able to handle common objects. On the other hand, it might copy individual peculiarities of that hand, which may be difficult to implement but not important for its function. Therefore, it would be interesting to find the intersection of properties that all human hands have in common, as well as the directions of freedom in which they differ from each other. Such a more general hand model could be created based on the measurements of hand postures of a large number of subjects.

The determination of the joint types and the calculation of the modelling error are limited by the accuracy and precision of the measurements. If the modelling error of a joint reaches below the measurement error by using a joint type with more **DoF**, it is likely that the additional **DoF** compensate the modelling error instead of describing any real motion.

The method for selecting the joint types includes a subjective element, namely the setting of the accuracy threshold. This will likely be influenced by assumptions and prior knowledge about the joint types. For example, in this thesis, the threshold of the intermediately complex model was set in a way that the resulting joint types coincided with the joint types mentioned in the literature. A further subjective element is the selection of the postures that are used for identifying the joint parameters. In this thesis attention was paid to cover the whole range of motion of each **DoF**, that is, including at least one posture where the **DoF** is close to its minimum position and one where it is close to its maximum position.

The grasp simulations relied on failed grasps to reveal the importance of kinematic properties for the functionality of the hand. The grasps tested so far were limited to a set of six object grasps times four hand models. In-hand manipulation was not yet considered. The results were influenced by some subjectivity,

because human operator interaction was required. Since the grasp score evaluates the contact wrench on the object and therefore on the contact forces, it cannot be treated from a purely kinematic point of view. The simulation assumed unit forces at each contact location. The actual forces that the muscles and actuators can apply were not considered. The grasp score should therefore be taken *cum grano salis*. The simulation treated the finger segments as rigid bodies. Possibly important contributions of the soft tissue deformation to grasp stability by moments and form closure could therefore not be evaluated. A constant friction coefficient was assumed, ignoring the dependency of the friction coefficient on the materials of hand and object.

7.2 Outlook

In future work, it might make sense to explore other joint types, for example, translational joints, joints with coupled rotation and translation, parallel mechanisms like 4- or 5-bar linkages or the two-curvature model by Van Nierop et al. [2008]. Interdependencies between DoF and joints could be considered, in order to create hand models that avoid unnatural postures. In order to make the selection of joint types less subjective, statistical methods like Akaike Information Criterion or Bayesian Information Criterion could be applied for all fingers, as it was already done for the thumb by Corato et al. [2009].

It would also be interesting to analyse the hand movements of a very large group of subjects and to find out which kinematic properties these hands have in common and in which properties they differ from each other. The properties in which they differ from each other could be regarded as “free” properties, because all of the subjects have fully functional hands. In order to build an anthropomorphic hand that copies human movement abilities, the free properties could be chosen so that they are most easily implemented. As an example, if the angle between two rotation axes varies in humans between 85 and 95 degrees, the robotic hand could be designed with orthogonal axes, if this gives an advantage for the manufacture or control of the robotic hand.

Bibliography

ABlogtoWatch.com. Jaquet Droz: The writer automaton from 1774 in action. aBlogtoWatch.com, 2012. URL <http://www.youtube.com/watch?v=ux2KW20nqHU>. Accessed 2014-03-25.

Peter K. Allen, Matei T. Ciocarlie, Corey Goldfeder, and Hao Dang. Low-dimensional data-driven grasping. In Ravi Balasubramanian and Yoky Matsuoka, editors, “*Understanding the Human Hand for Advancing Robotic Manipulation*” Workshop at Robotics: Science and Systems 2009, 2009. URL <http://coreygoldfeder.com/papers/RSS09.pdf>.

Tamim Asfour, Kristian Regenstein, Pedram Azad, J Schroder, Alexander Bierbaum, Niko Vahrenkamp, and Rüdiger Dillmann. ARMAR-III: An integrated humanoid platform for sensory-motor control. In *Humanoid Robots, 2006 6th IEEE-RAS International Conference on*, pages 169–175, 2006. doi: [10.1109/ICHR.2006.321380](https://doi.org/10.1109/ICHR.2006.321380).

George Bekey and Jose Fermoso. Interview: USC’s George Bekey on Past and Future Robot Hands. Gadget Lab | Wired.com, September 2008. URL <http://www.wired.com/gadgetlab/2008/09/robotic-hands-h/>. Accessed 2014-03-25.

Boris Bertram. Geschichte der Armprothetik. In *9. interdisziplinärer SGA/IUGR-Workshop 1.-2.7.2011 in Kloster Schöntal*, pages 29–45, 2011. URL <http://sga-syndrom.de/Proceedings/2011-Proceedingband.pdf#page=29>. Accessed 2014-03-27.

Lyndon B Bridgwater, CA Ihrke, Myron A Diftler, Muhammad E Abdallah, Nicolaus A Radford, JM Rogers, S Yayathi, R Scott Askew, and D Marty Linn. The robonaut 2 hand-designed to do work with tools. In *Robotics and Automation (ICRA), 2012 IEEE International Conference on*, pages 3425–3430, 2012. doi: [10.1109/ICRA.2012.6224772](https://doi.org/10.1109/ICRA.2012.6224772).

- Bryan Buchholz, Thomas J. Armstrong, and Steven A. Goldstein. Anthropometric data for describing the kinematics of the human hands. *Ergonomics*, 35(3):261–273, 1992. doi: [10.1080/00140139208967812](https://doi.org/10.1080/00140139208967812).
- J. Butterfaß, M. Grebenstein, H. Liu, and G. Hirzinger. DLR-Hand II: Next generation of a dextrous robot hand. In *Proceedings of the 2001 IEEE Int. Conference on Robotics and Automation*, Seoul, Korea, 2001. doi: [10.1109/ROBOT.2001.932538](https://doi.org/10.1109/ROBOT.2001.932538).
- Joerg Butterfass, Gerd Hirzinger, S Knoch, and Hong Liu. DLR’s multisensory articulated hand. I. Hard-and software architecture. In *Robotics and Automation. Proceedings. 1998 IEEE International Conference on*, volume 3, pages 2081–2086, 1998. doi: [10.1109/ROBOT.1998.680625](https://doi.org/10.1109/ROBOT.1998.680625).
- Aurelio Cappozzo. Gait analysis methodology. *Human Movement Science*, 3(1):27–50, 1984. doi: [10.1016/0167-9457\(84\)90004-6](https://doi.org/10.1016/0167-9457(84)90004-6).
- P. Cerveri, N. Lopomo, A. Pedotti, and G. Ferrigno. Derivation of centers of rotation for wrist and fingers in a hand kinematic model: Methods and reliability results. *Annals of Biomedical Engineering*, 33:402–412, 2005. doi: [10.1007/s10439-005-1743-9](https://doi.org/10.1007/s10439-005-1743-9).
- P. Cerveri, E. De Momi, N. Lopomo, G. Baud-Bovy, R. M. L. Barros, and G. Ferrigno. Finger kinematic modeling and real-time motion estimation. *Annals of Biomedical Engineering*, 35:1989–2002, 2007. doi: [10.1007/s10439-007-9364-0](https://doi.org/10.1007/s10439-007-9364-0).
- P. Cerveri, E. De Momi, M. Marchente, N. Lopomo, G. Baud-Bovy, R. M. L. Barros, and G. Ferrigno. In vivo validation of a realistic kinematic model for the trapezio-metacarpal joint using an optoelectronic system. *Annals of Biomedical Engineering*, 36(7):1268–1280, 2008.
- Maxime Chalon, Markus Grebenstein, Thomas Wimboeck, and Gerd Hirzinger. The thumb: Guidelines for a robotic design. In *International Conference on Intelligent Robots and Systems (IROS 2010)*, 2010. doi: [10.1109/IROS.2010.5650454](https://doi.org/10.1109/IROS.2010.5650454).
- Lillian Y. Chang and Nancy S. Pollard. Constrained least-squares optimization for robust estimation of center of rotation. *Journal of Biomechanics*, 40(6):1392–1400, 2007a. doi: [10.1016/j.jbiomech.2006.05.010](https://doi.org/10.1016/j.jbiomech.2006.05.010).

- Lillian Y. Chang and Nancy S. Pollard. Robust estimation of dominant axis of rotation. *Journal of Biomechanics*, 40(12):2707–2715, 2007b. ISSN 0021-9290. doi: [10.1016/j.jbiomech.2007.01.010](https://doi.org/10.1016/j.jbiomech.2007.01.010).
- D. Comaniciu and P. Meer. Mean shift: a robust approach toward feature space analysis. *IEEE Transactions Pattern Analysis and Machine Intelligence*, 24: 603–619, 2002. doi: [10.1109/34.1000236](https://doi.org/10.1109/34.1000236).
- Francesco Corato, Pietro Falco, Martin Lösch, Emilio Maggio, Rainer Jäkel, and Luigi Villani. Original approaches to interpretation learning, and modelling, from the observation of human manipulation. In *Workshop “Understanding the Human Hand for Advancing Robotic Manipulation” at the RSS conference*, 2009. More in-depth information is provided in the public deliverable D1.1 of the Dexmart project (<http://www.dexmart.eu/index.php?id=13735>).
- John J. Craig. *Introduction to robotics: mechanics and control*. Pearson Education, 3rd edition, 2005. ISBN 0201-54361-3.
- Mark R Cutkosky. On grasp choice, grasp models, and the design of hands for manufacturing tasks. *Robotics and Automation, IEEE Transactions on*, 5(3): 269–279, 1989. doi: [10.1109/70.34763](https://doi.org/10.1109/70.34763).
- Mary F. Dempsey, Barrie Condon, and Donald M. Hadley. MRI safety review. *Seminars in Ultrasound, CT, and MRI*, 23:392 – 401, 2002.
- J. Denavit and R. S. Hartenberg. A kinematic notation for lower-pair mechanisms based on matrices. *Transactions of the ASME. Journal of Applied Mechanics*, 22:215–221, 1955.
- Ashish D Deshpande, Zhe Xu, Michael J Vande Weghe, Benjamin H Brown, Jonathan Ko, Lillian Y Chang, David D Wilkinson, Sean M Bidic, and Yoky Matsuoka. Mechanisms of the anatomically correct testbed hand. *Mechatronics, IEEE/ASME Transactions on*, 18(1):238–250, 2013. doi: [10.1109/TMECH.2011.2166801](https://doi.org/10.1109/TMECH.2011.2166801).
- Rosen Diankov. *Automated Construction of Robotic Manipulation Programs*. PhD thesis, The Robotics Institute, Carnegie Mellon University, 2010. URL http://www.programmingvision.com/rosen_diankov_thesis.pdf.
- Rosen Diankov and James Kuffner. Openrave: A planning architecture for autonomous robotics. Technical Report CMU-RI-TR-08-34, Robotics Institute,

- Pittsburgh, PA, July 2008. URL http://www.ri.cmu.edu/publication_view.html?pub_id=6117&menu_code=0307.
- M.A. Diftler, J.S. Mehling, M.E. Abdallah, N.A. Radford, L.B. Bridgwater, A.M. Sanders, R.S. Askew, D.M. Linn, J.D. Yamokoski, F.A. Permenter, B.K. Hargrave, R. Platt, R.T. Savy, and R.O. Ambrose. Robonaut 2 – the first humanoid robot in space. In *2011 IEEE International Conference on Robotics and Automation*, 2011. doi: 10.1109/ICRA.2011.5979830.
- R. Dumas and L. Cheze. Soft tissue artifact compensation by linear 3D interpolation and approximation methods. *Journal of Biomechanics*, 42(13): 2214–2217, 2009. doi: 10.1016/j.jbiomech.2009.06.006.
- Thomas Feix, Heinz-Bodo Schmiedmayer, Javier Romero, and Danica Kragić. A comprehensive grasp taxonomy. In *Robotics, Science and Systems conference: workshop on Understanding the human hand for advancing robotic manipulation*, 2009. URL <http://grasp.xief.net/documents/abstract.pdf>.
- K. Fukunaga and L. D. Hostetler. The estimation of a gradient of a density function, with applications in pattern recognition. *IEEE Transactions on Information Theory*, 21:32–40, 1975. doi: 10.1109/TIT.1975.1055330.
- Bo Gao. *A new soft tissue artifact compensation technique in human motion analysis and clinical applications*. PhD thesis, University of Florida, 2009. URL http://etd.fcla.edu/UF/UF0041214/gao_b.pdf. Accessed 2014-01-24.
- Joel Gibbard. Open hand project, 2013. URL <http://www.openhandproject.org/>. Accessed 2014-03-27.
- Ricardo González Camarero. Dynamic simulation and control of exoskeletal devices for an astronaut’s hand and leg. Master’s thesis, Tecnun - Universidad de Navarra, 2014. URL <http://elib.dlr.de/89554/>.
- Andreas Goß. Development of a human finger model with the CAE-software Simpack. Master’s thesis, University of Applied Sciences Regensburg, 2012. URL <http://elib.dlr.de/79969/>.
- GRASP. Welcome to opengrasp, 2011. URL <http://opengrasp.sourceforge.net/>. Accessed 2015-02-24.
- Markus Grebenstein. *Approaching human performance: The functionality-driven Awiwi robot hand*, volume 98 of *Springer Tracts in Advanced Robotics*. Springer, 2012. ISBN 3319035924.

Markus Grebenstein, Maxime Chalon, Gerd Hirzinger, and Roland Siegwart. A method for hand kinematics designers - 7 billion perfect hands. In *Proceedings of 1st International Conference on Applied Bionics and Biomechanics*, 2010. URL <http://www.thehandembodied.eu/pdf/markusGrebenstein7billionICABB10.pdf>. Accessed 2011-05-16.

Markus Grebenstein, Alin Albu-Schäffer, Thomas Bahls, Maxime Chalon, Oliver Eiberger, Werner Friedl, Robin Gruber, Ulrich Hagn, Robert Haslinger, Hannes Höppner, Stefan Jörg, Matthias Nickl, Alexander Nothelfer, Florian Petit, Joseph Reill, Nikolaus Seitz, Thomas Wimböck, Sebastian Wolf, Tilo Wüsthoff, and Gerd Hirzinger. The DLR Hand Arm System. In *2011 IEEE International Conference on Robotics and Automation*, 2011. doi: [10.1109/ICRA.2011.5980371](https://doi.org/10.1109/ICRA.2011.5980371).

Alan Greene. Polydactylysm, 2008. URL <http://www.drgreene.com/qa-articles/polydactylysm/>. Accessed 2014-02-11.

Agneta Gustus, Georg Stillfried, Judith Visser, Henrik Jörntell, and Patrick van der Smagt. Human hand modelling: kinematics, dynamics, applications. *Biological Cybernetics*, 106:741–755, 2012. doi: [10.1007/s00422-012-0532-4](https://doi.org/10.1007/s00422-012-0532-4).

Richard S. Hartenberg and Jaques Denavit. *Kinematic Synthesis of Linkages*. McGraw-Hill Book Company, 1964. URL <http://kmodd1.library.cornell.edu/bib.php?m=23>.

U. Hillenbrand. Non-parametric 3D shape warping. In *Proceedings International Conference on Pattern Recognition (ICPR)*, 2010. doi: [10.1109/ICPR.2010.651](https://doi.org/10.1109/ICPR.2010.651).

Ulrich Hillenbrand. Consistent parameter clustering: definition and analysis. *Pattern Recognition Letters*, 28:1112–1122, 2007. doi: [10.1016/j.patrec.2007.01.006](https://doi.org/10.1016/j.patrec.2007.01.006).

Ulrich Hillenbrand and Alexander Fuchs. An experimental study of four variants of pose clustering from dense range data. *Computer Vision and Image Understanding*, 115(10):1427 – 1448, 2011. doi: [10.1016/j.cviu.2011.06.007](https://doi.org/10.1016/j.cviu.2011.06.007).

Anne Hollister, William L. Buford, Loyd M. Myers, David J. Giurintano, and Andrew Novick. The axes of rotation of the thumb carpometacarpal joint. *Journal of Orthopaedic Research*, 10:454–460, 1992. doi: [10.1002/jor.1100100319](https://doi.org/10.1002/jor.1100100319).

- Anne Hollister, David J. Giurintano, William L. Buford, Loyd M. Myers, and Andrew Novick. The axes of rotation of the thumb interphalangeal and metacarpophalangeal joints. *Clinical Orthopaedics and Related Research*, 320:188–193, 1995. URL http://journals.lww.com/corr/Abstract/1995/11000/The_Axes_of_Rotation_of_the_Thumb_Interphalangeal.31.aspx. Accessed 2008-11-19.
- Berthold K. P. Horn. Closed-form solution of absolute orientation using unit quaternions. *Journal of the Optical Society of America A*, 4(4):629–642, 1987.
- Thea Iberall. Human prehension and dexterous robot hands. *The International Journal of Robotics Research*, 16(3):285–299, 1997. doi: [10.1177/027836499701600302](https://doi.org/10.1177/027836499701600302).
- S.C. Jacobsen, E.K. Iverse, D.F. Knutti, R.T. Johnson, and K.B. Bigger. Design of the Utah/M.I.T. Dextrous Hand. *Robotics and Automation. Proceedings. 1986 IEEE International Conference on*, 3:1520–1532, 1986. doi: [10.1109/ROBOT.1986.1087395](https://doi.org/10.1109/ROBOT.1986.1087395).
- Lynette A Jones and Susan J Lederman. *Human hand function*. Oxford University Press, 2006. ISBN 978-0-19-517315-4.
- Satomi Kamojima, Natsuki Miyata, and Jun Ota. Identification of position and orientation of hand bones from MR images by bone model registration. In *Proceedings of 2004 IEEE/RSJ International Conference on Intelligent Robots and Systems*, 2004. doi: [10.1109/IROS.2004.1389695](https://doi.org/10.1109/IROS.2004.1389695).
- A. Kapandji. Cotation clinique de l'opposition et de la contre-opposition du pouce [clinical test of opposition and counter-opposition of the thumb]. *Annales de Chirurgie de la Main*, 5(1):67–73, 1986. doi: [10.1016/S0753-9053\(86\)80053-9](https://doi.org/10.1016/S0753-9053(86)80053-9).
- I. A. Kapandji. *Funktionelle Anatomie der Gelenke*. Enke, 2 edition, 1992. ISBN 3-432-94232-X. Translated by J. Koebke from Physiologie articulaire / Physiology of the joints.
- Harushira Kawasaki, Tsuneo Komatsu, and Kazunao Uchiyama. Dexterous anthropomorphic robot hand with distributed tactile sensor: Gifu Hand II. *IEEE/ASME Transactions on Mechatronics*, 7(3):296–303, 2002. doi: [10.1109/TMECH.2002.802720](https://doi.org/10.1109/TMECH.2002.802720).
- W. Khalil and E. Dombre. *Modeling, Identification and Control of Robots*. Taylor & Francis, 2002. ISBN 1-56032-983-1.

- Anna Kochan. Shadow delivers first hand. *Industrial Robot: An International Journal*, 32(1):15–16, 2005. doi: [10.1108/01439910510573237](https://doi.org/10.1108/01439910510573237).
- Jürgen Koebke. *A biomechanical and morphological analysis of human hand joints*. Springer-Verlag, 1983.
- Timothy J Koh, Mark D Grabiner, and Robert J De Swart. In vivo tracking of the human patella. *Journal of biomechanics*, 25(6):637–643, 1992. doi: [10.1016/0021-9290\(92\)90105-A](https://doi.org/10.1016/0021-9290(92)90105-A).
- K Kuczynski. The thumb and the saddle. *Journal of Hand Surgery (European Volume) (“The Hand”)*, 7(2):120–122, 1975.
- A. Leardini, L. Chiari, U. Della Croce, and A. Cappozzo. Human movement analysis using stereophotogrammetry. Part 3. soft tissue artifact assessment and compensation. *Gait and Posture*, 21(2):212–225, February 2005. doi: [10.1016/j.gaitpost.2004.05.002](https://doi.org/10.1016/j.gaitpost.2004.05.002).
- Beatriz León, Stefan Ulbrich, Rosen Diankov, Gustavo Puche, Markus Przybylski, Antonio Morales, Tamim Asfour, Sami Moisio, Jeannette Bohg, James Kuffner, and Rüdiger Dillmann. Opengrasp: A toolkit for robot grasping simulation. In Noriaki Ando, Stephen Balakirsky, Thomas Hemker, Monica Reggiani, and Oskar von Stryk, editors, *Simulation, Modeling, and Programming for Autonomous Robots*, volume 6472 of *Lecture Notes in Computer Science*, pages 109–120. Springer Berlin Heidelberg, 2010. ISBN 978-3-642-17318-9. doi: [10.1007/978-3-642-17319-6_13](https://doi.org/10.1007/978-3-642-17319-6_13).
- Owen John Lewis. Joint remodelling and the evolution of the human hand. *Journal of anatomy*, 123(Pt 1):157, 1977. URL <http://www.ncbi.nlm.nih.gov/pmc/articles/PMC1234261/>.
- Hong Liu, Peter Meusel, Bertram Willberg, Gerd Hirzinger, M.H. Jin, Y.W. Liu, R. Wei, Z.W. Xie, and H.G. Cai. The modular multisensory DLR-HIT-hand: Hardware and software architecture. In *Proceeding ISR-2006, Joint Conference on Robotics / ROBOTIK 2006*, 2006. URL <http://elib.dlr.de/51245/>. Accessed 2014-03-27.
- Hong Liu, K Wu, Peter Meusel, Nikolaus Seitz, Gerd Hirzinger, MH Jin, YW Liu, SW Fan, T Lan, and ZP Chen. Multisensory five-finger dexterous hand: The DLR/HIT Hand II. In *Intelligent Robots and Systems, 2008. IROS 2008. IEEE/RSJ International Conference on*, pages 3692–3697, 2008. doi: [10.1109/IROS.2008.4650624](https://doi.org/10.1109/IROS.2008.4650624).

- L. Lucchetti, A. Cappozzo, A. Cappello, and U. Della Croce. Skin movement artefact assessment and compensation in the estimation of knee joint kinematics. *Journal of Biomechanics*, 31(11):977–84, 1998. doi: [10.1016/S0021-9290\(98\)00083-9](https://doi.org/10.1016/S0021-9290(98)00083-9).
- A. Lundberg, O. K. Svensson, G. Nemeth, and G. Selvik. The axis of rotation of the ankle joint. *Journal of Bone & Joint Surgery, British Volume*, 71(1): 94–99, 1989. URL <http://www.bjj.boneandjoint.org.uk/content/71-B/1/94.abstract>.
- Arne Lundberg. On the use of bone and skin markers in kinematics research. *Human Movement Science*, 15(3):411–422, 1996. doi: [10.1016/0167-9457\(96\)00008-5](https://doi.org/10.1016/0167-9457(96)00008-5).
- John T. Manter. Movements of the subtalar and transverse tarsal joints. *The Anatomical Record*, 80(4):397–410, 1941. doi: [10.1002/ar.1090800402](https://doi.org/10.1002/ar.1090800402).
- F. Marin, J. Allain, Diop, N. Maurel, M. Simondi, and F. Lavaste. On the estimation of knee joint kinematics. *Human Movement Science*, 18:613–626, 1999. doi: [10.1016/S0167-9457\(99\)00024-X](https://doi.org/10.1016/S0167-9457(99)00024-X).
- Kurt Meyberg and Peter Vachenauer. *Höhere Mathematik 1*. 4. Auflage. Springer, Berlin, 1999.
- Andrew T. Miller. *GraspIt!: A Versatile Simulator for Robotic Grasping*. PhD thesis, Columbia University, 2001. URL www.cs.columbia.edu/~amiller/thesis.pdf.
- Mindtrans.narod.ru. The best robotic hands, 2010–2013. URL <http://mindtrans.narod.ru/hands/hands.htm>. Accessed 2014-02-06.
- Natsuki Miyata, Makiko Kouchi, Masaaki Mochimaru, and Tsuneya Kurihaya. Finger joint kinematics from MR images. In *IEEE/RSJ International Conference on Intelligent Robots and Systems*, 2005. doi: [10.1109/IROS.2005.1545611](https://doi.org/10.1109/IROS.2005.1545611).
- Hisao Moritomo, Akira Goto, Yoshinobu Sato, Kazuomi Sugamoto, Tsuyoshi Murase, and Hideki Yoshikawa. The triquetrum-hamate joint: An anatomic and in vivo three-dimensional kinematic study. *The Journal of Hand Surgery*, 28A(5):797–805, 2003.
- J. A. Nelder and R. Mead. A simplex method for function minimization. *The Computer Journal*, 7(4):308–313, 1965. doi: [10.1093/comjnl/7.4.308](https://doi.org/10.1093/comjnl/7.4.308).

- M. J. Pearcy and M. W. Whittle. Movements of the lumbar spine measured by three-dimensional x-ray analysis. *Journal of Biomedical Engineering*, 4(2): 107–112, 1982. doi: [10.1016/0141-5425\(82\)90070-X](https://doi.org/10.1016/0141-5425(82)90070-X).
- Alana Peters, Brook Galna, Morgan Sangeux, Meg Morris, and Richard Baker. Quantification of soft tissue artifact in lower limb human motion analysis: a systematic review. *Gait & posture*, 31(1):1–8, 2010. doi: [10.1016/j.gaitpost.2009.09.004](https://doi.org/10.1016/j.gaitpost.2009.09.004).
- Robert N. Rohling and John M. Hollerbach. Calibrating the human hand for haptic interfaces. *Presence: Teleoperators and Virtual Environments*, 2(4): 281–296, 1993. ISSN 1054-7460.
- Robert N. Rohling and John M. Hollerbach. Modeling and parameter estimation of the human index finger. In *Robotics and Automation, 1994. Proceedings., 1994 IEEE International Conference on*, pages 223–230. IEEE, 1994.
- Alexandru Rusu. Segmentation of bone structures in magnetic resonance images (mri) for human hand skeletal kinematics modelling. Master’s thesis, Erasmus Mundus in Vision and Robotics (VIBOT), 2012. URL <http://elib.dlr.de/74593/>.
- Jae Hun Ryu, Natsuki Miyata, Makiko Kouchi, Masaaki Mochimaru, and Kwan H. Lee. Analysis of skin movements with respect to bone motions using MR images. *International Journal of CAD/CAM*, 3:61–66, 2003.
- Jae Hun Ryu, Natsuki Miyata, Makiko Kouchi, Masaaki Mochimaru, and Kwan H. Lee. Analysis of skin movement with respect to flexional bone motion using mr images of a hand. *Journal of Biomechanics*, 39:844–852, 2006. doi: [10.1016/j.jbiomech.2005.02.001](https://doi.org/10.1016/j.jbiomech.2005.02.001).
- Arash Salarian. Repeated Measures ANOVA - File Exchange - MATLAB Central, 2008. URL <http://www.mathworks.com/matlabcentral/fileexchange/22088-repeated-measures-anova>. Accessed 2015-03-24.
- Joaquín L. Sancho-Bru, Antonio Morales, Antonio Pérez-González, Beatriz E. León, José L Iserte, Margarita Vergara, Marta C. Mora, and Pablo J. Rodríguez-Cervantes. *Towards a realistic and self-contained biomechanical model of the hand*. INTECH Open Access Publisher, 2011. doi: [10.5772/19977](https://doi.org/10.5772/19977).
- Stefan Schulz, Christian Pylatiuk, Artem Kargov, Reinhold Oberle, and Georg Bretthauer. Progress in the development of anthropomorphic flu-

- idic hands for a humanoid robot. In *Humanoid Robots, 2004 4th IEEE/RAS International Conference on*, volume 2, pages 566–575, 2004. doi: [10.1109/ICHR.2004.1442671](https://doi.org/10.1109/ICHR.2004.1442671).
- H. J. Sommer 3rd and N. R. Miller. A technique for kinematic modeling of anatomical joints. *Journal of Biomechanical Engineering*, 102(4):311, 1980. doi: [10.1115/1.3138228](https://doi.org/10.1115/1.3138228).
- STAMAS. Homepage, 2013. URL <http://www.stamas.eu/>. Accessed 2015-02-23.
- G. Stillfried, U. Hillenbrand, M. Settles, and P. van der Smagt. MRI-based skeletal hand movement model. In R. Balaraman and V. Santos, editors, *The Human Hand as an Inspiration for Robot Hand Development*, volume 95 of *Springer Tracts on Advanced Robotics*, pages 49–76. Springer, 2014. doi: [10.1007/978-3-319-03017-3_3](https://doi.org/10.1007/978-3-319-03017-3_3). URL <http://elib.dlr.de/85039/>.
- Georg Stillfried. Kinematische Simulation einer menschlichen Hand. Diplomarbeit, TU München, Lehrstuhl für Angewandte Mechanik, 2009.
- Georg Stillfried and Patrick van der Smagt. Movement model of a human hand based on magnetic resonance imaging (MRI). In *1st International Conference on Applied Bionics and Biomechanics*, 2010. URL <http://elib.dlr.de/65935/>.
- A. Synek, M. Settles, and G. Stillfried. Multi-body simulation of a human thumb joint by sliding surfaces. In *Biomedical Robotics and Biomechatronics (BioRob), 2012 4th IEEE RAS /EMBS International Conference on*, pages 379 –384, june 2012. doi: [10.1109/BioRob.2012.6290755](https://doi.org/10.1109/BioRob.2012.6290755).
- Alexander Synek. Simulation of a human finger joint with sliding surfaces. Master’s thesis, FH Technikum Wien, 2011.
- TIME. In celebration of the robonaut, 2012. URL <http://content.time.com/time/health/article/0,8599,2108652,00.html>. Accessed 2014-03-27.
- R. Tomovic and G. Boni. An adaptive artificial hand. *Automatic Control, IRE Transactions on*, 7(3):3–10, 1962. doi: [10.1109/TAC.1962.1105456](https://doi.org/10.1109/TAC.1962.1105456).
- Onno A. van Nierop, Aadjan van der Helm, Kees J. Overbeeke, and Tom J.P. Djajadiningrat. A natural human hand model. *Visual Comput*, 24:31–44, 2008. doi: [10.1007/s00371-007-0176-x](https://doi.org/10.1007/s00371-007-0176-x).

- Michael Vande Weghe, Matthew Rogers, Michael Weissert, and Yoki Matsouka. The ACT hand: Design of the skeletal structure. In *Proceedings of the 2004 IEEE International Conference on Robotics & Automation*, pages 3375–3379, New Orleans, LA, 2004.
- Kenneth Waldron and James Schmiedeler. Kinematics. In Bruno Siciliano and Oussama Khatib, editors, *Handbook of Robotics*. Springer, 2008. ISBN 978-3-540-23957-4.
- Dieter Christian Wirtz, Norbert Schiffers, Thomas Pandorf, Klaus Radermacher, Dieter Weichert, and Raimund Forst. Critical evaluation of known bone material properties to realize anisotropic FE-simulation of the proximal femur. *Journal of Biomechanics*, 33(10):1325–1330, 2000. doi: [10.1016/S0021-9290\(00\)00069-5](https://doi.org/10.1016/S0021-9290(00)00069-5).
- HJ Woltring, A de Lange, JMG Kauer, and HWJ Huiskes. *Biomechanics: Basic and Applied Research*, chapter Instantaneous helical axis estimation via natural, cross-validated splines. Martinus Nijhoff / Springer, 1987. ISBN 978-0898389616. URL <http://library.tue.nl/csp/dare/LinkToRepository.csp?recordnumber=587036>.
- Zhe Xu, Emanuel Todorov, Brian Dallon, and Yoky Matsuoka. Design and analysis of an artificial finger joint for anthropomorphic robotic hands. In *Robotics and Automation (ICRA), 2011 IEEE International Conference on*, pages 5096–5102, 2011. doi: [10.1109/ICRA.2011.5979860](https://doi.org/10.1109/ICRA.2011.5979860).
- Y. Youm, T. E. Gillespie, A. E. Flatt, and B. L. Sprague. Kinematic investigation of normal MCP joint. *Journal of Biomechanics*, 11:109–118, 1978. doi: [10.1016/0021-9290\(78\)90003-9](https://doi.org/10.1016/0021-9290(78)90003-9).
- Xudong Zhang, Lee Sang-Wook, and Peter Braido. Determining finger segmental centers of rotation in flexion-extension based on surface marker measurement. *Journal of Biomechanics*, 36:1097–1102, 2003. doi: [10.1016/S0021-9290\(03\)00112-X](https://doi.org/10.1016/S0021-9290(03)00112-X).